HYBRID SILICON-VANADIUM DIOXIDE MODULATORS AND TRANSFORMATION OPTICS COUPLERS FOR OPTICAL INTERCONNECTS

By

Petr Markov

Dissertation
Submitted to the Faculty of the
Graduate School of Vanderbilt University
in partial fulfillment of the requirements
for the degree of

DOCTOR OF PHILOSOPHY
in
Electrical Engineering

May, 2015
Nashville, TN

Approved:
Professor Sharon M. Weiss
Professor Richard F. Haglund, Jr.
Professor Jason Valentine
Professor Kirill Bolotin
Professor Yaqiong Xu

To friends, family, and colleagues

who supported me all the way.

ACKNOWLEDGMENTS

Fresh from undergrad and aspired to do great things, I was lucky to be accepted to Vanderbilt University with no prior research or physics experience. This luck I owe to Sharon Weiss, who believed in me despite me lacking some important background. I attribute most of my success in graduate school to her encouragement to learn new things and develop my ideas into fruitful research. It was really motivating to come in into her office with an idea and not have it shut down but rather critically discussed and leave with a plan for experiments to get this idea working. Also I am grateful to her for teaching me that research is 99% failure and patience is of utmost importance. I would like to thank Sharon for guiding me through tough times and not pressuring me during periods of seeming lack of progress, and also for not kicking me out of the group when I fell asleep in her class once.

This thesis would not be possible without the help and support of ORNL CNMS staff (Scott Retterer, Dayrl Briggs, Dale Hensley, Kevin Lester, Bernadeta Srijanto, and Jessica Gardner) and VINSE staff (Tony Hmelo, Jed Ziegler, Ben Schmidt, and Bo Choi). Fabrication has been a huge part of my graduate work and I am grateful for the guidance and expertise these wonderful people have provided for me over the years, making working in a cleanroom a pleasure. Excellent research experience at CNMS was one of the huge factors in my enjoyment of frequent trips to Oak Ridge, the other factor was awesome pizza at Big Ed's. I would like thank Yang Jiao for letting me stay and hang out with him during my tips to Oak Ridge. Prior to that I have been known to camp near Oak Ridge and would like to thank Del and Marty Scrubbs for running the best campground ever and helping me out with food and shelter when I was waiting for my financial reimbursement.

I would like to thank my mentors within the group, Chris Kang and Judson Ryckman, for teaching me the nuances of fabrication and testing of photonic devices. I would like to thank other members of Weiss group as well, especially Gilbert Rodriguez, Jeremy Mares, Yang Jiao, and Shweta Bhanderu, for frequent fruitful discussions, science and otherwise. The environment within the group has always been friendly, non-competitive and supportive with numerous collaborations within the group and fun lunch outings helping to keep me sane. Out of the group collaborations have proved most fruitful for me, so I would like to thank my collaborators from the Haglund group, Bob Marvel and Krishen Appavoo, and the Bolotin group, Hiram Conley. These guys provided outstanding knowledge in their respective areas of expertise and worked with me at an amazing pace.

I would like to thank friends and family without whom I would not have motivation to complete this long process. Some of the best ideas I have had were originated while drinking beer and watching soccer with Krishen and Dima Markov. Besides scientific contributions, blowing off steam has been very important to stay on track and not burn out. I thank Kirill Zavalin for being always there in trouble, joy, and adventures. I also would like to thank my fiancee Casey for keeping me on track and focused on research and for making my apartment feel more like home, cozy and comfortable. And finally, I would like to thank my parents, brother, and grandparents for being 100% supportive through my Ph.D. experience.

TABLE OF CONTENTS

Page

Chapter

Appendix

LIST OF TABLES

LIST OF FIGURES

LIST OF ABBREVIATIONS

DC	**D**irect **C**urrent
CMOS	**C**omplementary **M**etal **O**xide **S**emiconductor
PIC	**P**hotonic **I**ntegrated **C**ircuit
WDM	**W**avelength **D**ivision **M**ultiplexing
TO	**T**ransformation **O**ptics
MZI	**M**ach **Z**ehnder **I**nterferometer
SPP	**S**urface **P**ropagating **P**lasmon
PLD	**P**ulsed **L**aser **D**eposition
SEM	**S**canning **E**lectron **M**icroscopy
EBL	**E**lectron **B**eam **L**ithography
EBE	**E**lectron **B**eam **E**vaporation
FDTD	**F**inite **D**ifference **T**ime **D**omain
FEM	**F**inite **E**lement **M**ethod
Q	**Q**uality **F**actor
FET	**F**ield **E**ffect **T**ransistor
PEC	**P**roximity **E**rror **C**orrection
SOI	**S**ilicon **O**n **I**nsulator
TE	**T**ransverse **E**lectric (polarization)
TM	**T**ransverse **M**agnetic (polarization)
PMMA	**P**oly **M**ethyl **M**eth**A**crylate
CNMS	**C**enter for **N**anophase **M**aterials **S**ciences
ORNL	**O**ak **R**idge **N**ational **L**aboratory
VINSE	**V**anderbilt **I**nstitute of **N**anoscale **S**cience and **E**ngineering

CHAPTER 1

INTRODUCTION

1.1 Motivation for Optical Interconnects

The first major breakthrough in optical communication technology occurred in 1970 with the development of glass fibers with low propagation loss (20 dB/km) [16]. This advance followed shortly after, and was enabled by, the development of the semiconductor laser in 1962 [17]. These breakthroughs led to the development of long-haul optical communications that now form the backbone of the internet. Historically, optical communication research has been focused on long distance applications (i.e., a few to hundreds of kilometers). Now, however, the research emphasis has shifted towards developing short range optical communication components. There are two major scales in short range interconnects: rack-to-rack interconnects (less than a meter long) (Fig. 1.1(a)) and on-chip interconnects (several to hundreds of microns long) (Fig. 1.1(b)). Rack-to-rack interconnects, a middle ground between long range and on-chip, can be incredibly useful for servers as they can greatly reduce the power consumption in large server systems [18]. On-chip interconnects are the shortest range optical connections envisioned, connecting processor cores to memory and potentially yielding the greatest gains in processing power [19].

The on-chip optical interconnects are especially important because of the ever-growing demand for more powerful computers that has led to the emergence of multicore processors. Due to the nature of parallel processing, additional cores significantly improve performance. However, a major roadblock preventing the number of cores from growing without bounds is the rate at which they can share information. Current state-of-the-art technology uses on-chip copper electrical interconnects to carry information between cores and memory. However, copper interconnects suffer performance deterioration with increased data rates due to cross talk and increased power requirements [19, 20]. When an electrical signal travels along a copper transmission wire it experiences loss due to resistance of the metal wire. The lost power is converted to heat and needs to be dissipated away from the chip. This issue of heat dissipation is the primary performance bottleneck limiting how many electrical interconnects can be used on chip. Electrical interconnects are also susceptible to electro-magnetic noise as the information is carried by electrons. These drawbacks of electrical interconnects make their improvement unsustainable in the near future. As the transistor technology is improving in accordance with Moore's law [21], the copper interconnects have reached their potential and for continued improvement an alternative approach is desired [20]. A number of solutions have been proposed, including quantum information transfer [22], superconducting wires [23], and molecular computing [24], but these solutions have not demonstrated superior performance to conventional interconnects yet. Based on currently demonstrated performance, the most promising approach to date is using light to carry information in place of electrons.

When information on-chip is carried by photons, the major drawbacks of electrical information transfer are eliminated. Photons generally do not interact with one another because of a lack of coherence, and photons that propagate in a low loss dielectric do not generate excess heat. Moreover, their resistance to electro-magnetic noise makes optical interconnects an especially attractive option for use in harsh environments, such as space, military bases, airports, and factories. Another advantage of optical interconnects is that multiple channels can be transmitted through the same waveguide, as different wavelengths of light do not interfere with each other. This approach, called wavelength division multiplexing, allows to reduce the footprint of optical interconnects compared to electrical [25].

On-chip optical interconnects are expected to be implemented in future generations of silicon integrated circuits, and therefore must be complementary metal-oxide-semiconductor (CMOS) technology compatible [20]. Typically, an optics layer is added on top of the fabricated integrated circuit and the photonic components are connected to the electronics through vertical vias [26]. When developing optical interconnect components, one needs to always keep in mind the CMOS integration requirements.

Currently, silicon photonics is the best option for continued improvements of microelectronics technology, which focuses on providing CMOS-compatible solutions for optical on-chip interconnects. The most important building blocks in silicon photonics are on-chip light sources, optical modulators, waveguides, and detectors [20]. The communication flow is envisioned as follows: (1) the electrical signal comes in from the electronics layer and enters the electro-optic modulator units, which are fed light by on-chip or off-chip light sources; (2) the optical modulated signals propagate along waveguides and are detected by the photodetectors on the receiving end, which convert the optical signals to electrical signals that can be used by the receiving electronic layer. This approach (Fig. 1.1(a)) is envisioned by several companies for rack-to-rack optical interconnects currently being developed. The difference between on-chip and rack-to-rack interconnects is that in case of rack-to-rack communication the signal leaves the chip and is coupled to a fiber to be transmitted to another chip (Fig. 1.1(a)). Generally, rack-to-rack interconnect components can be a lot larger in size and do not have to be necessarily implemented on silicon. Currently photonic integrated circuits (PICs) for rack-to-rack interconnects are commercialized, implemented in GaAs or InP [27]. The components in these integrated circuits are quite large, however, and not CMOS compatible, and therefore not suitable for on-chip optical interconnects and also not CMOS compatible. In silicon, even though all basic components for optical interconnects have already been developed and demonstrated, their performance is more suitable for rack-to-rack interconnects and needs to be significantly improved for true on-chip applications [5, 19, 28]. The biggest issue with these components is their size, measuring in hundreds of microns. In order to make them suitable for on-chip interconnects, their length needs to be reduced by several orders of magnitude. The size of silicon devices is dictated by electro-optical properties of silicon and bypassing performance blocks due to these properties is the main challenge in silicon photonics.

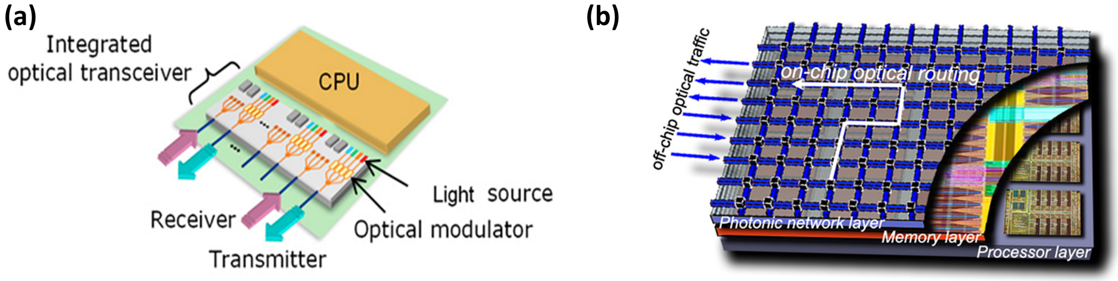

Figure 1.1: (a) Fujitsu vision of rack-to-rack optical interconnects, (b) Intel vision of on-chip optical interconnects

1.1.1 Challenges in Silicon Optical Interconnects

The optical properties of silicon support easy and efficient guiding of light in silicon with low loss [29]. Using silicon dioxide as a complimentary material allows for waveguides operating using total internal reflection to be constructed. Silicon is nearly transparent for infrared light of the current communication band (1550nm). This low absorption in the infrared makes silicon perfect for passive optical devices. For active optical devices however, other properties of silicon are not as beneficial. An indirect band semiconductor, silicon does not favor radiative recombination of carriers and therefore traditional lasing cannot be realized in silicon [28]. In order to deliver light on chip different approaches are therefore needed.

Another property of silicon that inhibits its use for active devices is its weak electro-optic non-linearity and strong thermo-optic effect. Silicon has a centro-symmetric diamond crystal structure suppressing the second order electro-optic effect (Pockel's effect), which is normally the strongest non-linear effect [30]. The third order non-linear effect (Kerr effect) is much weaker in general and in silicon it is almost absent, i.e. for electric field intensity of 10^5 V/cm the change in refractive index Δn is only $\sim 10^{-8}$ [30]. These non-linear effects are typically used in modulators and are essential for getting photons to interact with each other inside a material. Adding addition difficulty to the design process is silicon's thermo-optic effect which is much stronger than its electro-optic nonlinearities and much slower [31].

$$\Delta n(\Delta T) = 10^{-4}\Delta T \tag{1.1}$$

where Δn is the change in refractive index and ΔT is the change in temperature. In addition to these effects, there are other semiconductor effects based on the concentration of free carriers like carrier plasma dispersion and absorption [30].

$$\Delta n = -[8.8 * 10^{-22} \Delta N + 8.5 * 10^{-18} (\Delta P)^{0.8}] \tag{1.2}$$

$$\Delta \alpha = 8.5 * 10^{-18} \Delta N + 6.0 * 10^{-18} \Delta P \tag{1.3}$$

where $\Delta\alpha$ is the change in absorption, ΔN is the change in electron density and ΔP is the change in hole density. The carrier effects in silicon often times happen on the scales comparable to recombination rates which are relatively slow (ns) [30]. All these effects cause significant challenges for active device implementation in silicon. These issues and mitigation approaches are introduced in following sections.

1.2 Light Sources for Silicon Photonics

It is standard for optical communications to use lasers as a light source instead of LEDs. The use of laser light decreases loss due to dispersion and maximizes the use of available bandwidth for wavelength division multiplexing (WDM) [25]. As mentioned previously, it is not possible to achieve standard lasing in silicon due to an indirect band gap. Several alternative methods were developed to achieve integrated lasers on silicon, such as Raman lasing [28] and a hybrid approach [32]. The later approach was pioneered first and included bonding a complimentary material to the silicon wafer, and the former takes advantage of stimulated Raman scattering.

The hybrid approach provides the best efficiency, but the integration is quite challenging. Raman silicon lasers can only be pumped optically which adds a layer of complexity for them to be used in an integrated environment [28]. Although integrated lasers have the greatest long-term potential for integrated optics on-chip, currently off-chip lasers are more efficient. Fiber coupled infrared tunable high-power lasers are readily available to deliver light on-chip making fiber-to-chip coupling an important issue in silicon photonics. As well as using coupling to provide a light source for silicon photonics, the coupling solutions are important for rack-to-rack interconnects where the signal has to leave and enter a chip.

1.2.1 Requirements for Coupling from an External Source

An ideal fiber-to-chip coupler is lossless and broadband. Other considerations are specific for the intended application and available fabrication tools. For instance for the application of providing a light source for electro-optic modulators, it can be assumed that only a single wavelength is used and therefore the bandwidth requirement is not as critical. While for applications of signal in/out coupling, the broadband and low loss requirements are very important for energy conservation and flexibility.

Lossless couplers need to be reflection-less and are necessarily mode and impedance matched. Mode matching means that the optical mode of the input fiber is the same as the input mode of the coupler. Impedance is important to avoid reflections and must be matched to the input mode of the fiber. Optical impedance is defined as $Z = \sqrt{\frac{\mu}{\varepsilon}}$. If the material is assumed to be non-magnetic, which is usually the case with dielectrics, impedance matching becomes permittivity matching. When the coupler is mode and impedance matched to the fiber, the light is allowed to enter the coupler without reflections. After the light is coupled in, it generally needs to be converted to the mode of a silicon single mode waveguide.

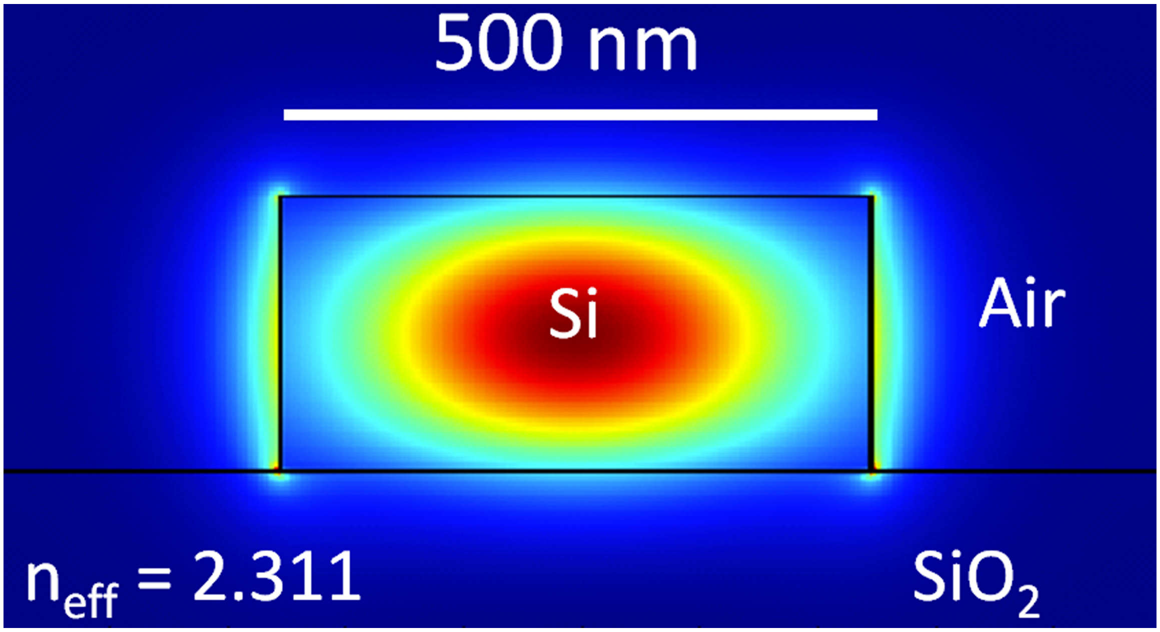

Figure 1.2: Electric field intensity distribution of a single mode silicon ridge waveguide at 1550 nm wavelength for TE polarization

The waveguide mode (Fig. 1.2) is much smaller than the fiber mode, therefore the light needs to be squeezed. Mode and impedance matching issues can be solved by a variety of approaches, described in detail in chapter 2.

1.2.2 Mode Size Conversion by Transforming the Optical Space

Besides conventional approaches to mode and impedance matching, there is an option to transform the optical space itself. Maxwell's equations that govern the flow of light are coordinate system invariant, meaning they have the same form no matter what coordinate system is chosen, but the permittivity (ε) and permeability (μ) of the space are scaled. This property allows to bend and squeeze the flow of light in almost any way imaginable by manipulating the ε and μ tensors [1]. Transformation optics (TO) provides a design approach to this light manipulation. A simple visualization of capabilities of TO is shown in

Fig. 1.3(a). Assuming a beam of light follows a straight line path in the original coordinate system, it will follow the path through the same coordinates if the coordinate system is distorted as shown in Fig. 1.3(a). This property allows for total control of the dispersion profile of certain regions in space assuming one can arbitrarily change both ε and μ.

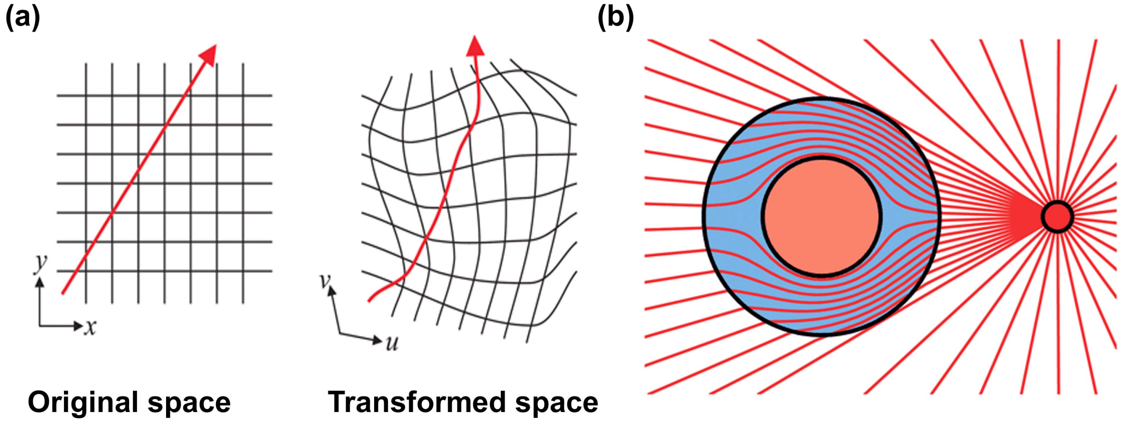

Figure 1.3: (a) An example of how light propagates through a distorted optical space, (b) Schematic representation of how invisibility cloaking works: the light from the sun bends around the circular concealed object. Adopted from ref. [1]

This powerful design capabilities of TO has led to the development of several complex optical devices, including invisibility cloaks (Fig. 1.4(d,e)) [3, 33–36], multifunctional optical devices (Fig. 1.4(a,b,c)) [2], and photonic black holes [37, 38]. The classic example of a TO designed device is an optical cloak. The idea of invisibility cloaks has been heavily publicized in entertainment media and usually dwells on the idea of being transparent to all light. Changing the material properties of a complex object, such as human body, to make invisible is impossible with the current state of technology, but TO allows for a different approach. This approach, pictured in Fig. 1.3(b), relies on placing a shell around the object, one desires to conceal. This shell is designed to bend the light around the object, effectively rendering it invisible or transparent [1]. The recent advancement in metameterials, as well as the theory of transformation optics has allowed this kind of cloaks to be implemented (Fig. 1.4(d,e)) [1, 39].

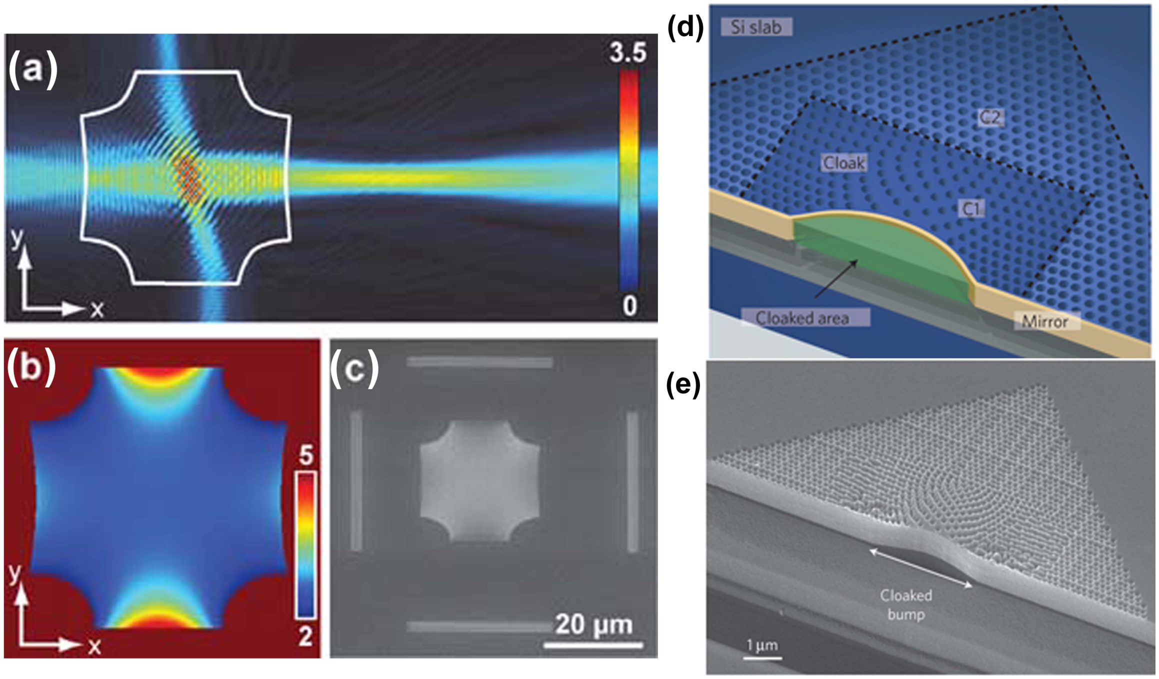

Figure 1.4: ”Janus” metadevice consisting of a focusing element (lens) in horizontal (x-direction) and a beam-shifter in vertical (y-direction). (a) Two-dimensional simulation of the spatial electric field magnitude (|Ez|) for a large beam propagating in the x-direction and a small beam in the y-direction. The white line marks the area of the transformed index region. (b) Spatial profile for the permittivity obtained by transformation of the space. (c) Scanning electron microscope image of the fabricated device together with the grating for coupling light to the transversal magnetic waveguide mode. Adopted from [2]. (d) Schematic diagram of a fabricated carpet cloak showing the different regions, where C1 is the gradient index cloak and C2 is a uniform index background. The cloak is fabricated in a SOI wafer where the Si slab serves as a 2D waveguide. The cloaked region (marked with green) resides below the reflecting bump (carpet) and can conceal any arbitrary object. The cloak will transform the shape of the bump back into a virtually flat object. (e) Scanning electron microscope image of a fabricated carpet cloak. The width and depth of the cloaked bump are 3.8 mum and 400 nm, respectively. Adopted from [3].

The method of transformation optics is perfect for converting a fiber mode to a waveguide mode without losses. The transformed space tapers from the size of an optical fiber tip at the input of the coupler to the size of a single mode silicon waveguide, while the original space stays the size of the fiber tip. The light ”sees” the original space and propagates freely through the coupler, while following the transformed space trajectory becoming focused. Detailed approach is described in chapter 2.

1.3 Modulators for Silicon Photonics

The optical modulator is an essential component of optical interconnects for integrated photonic circuits [20]. A typical electro-optic modulator converts the change in refractive index of the active material due to input voltage to an optical signal change. The most popular modulator geometries are Mach-Zehnder interferometers (MZI) (Fig. 1.5(a)) [40] and ring resonators (Fig. 1.5(b)) [5]. MZIs split the input light into two arms with one arm incorporating the active material, and when the two signal are recombined they interfere based on the phase change introduced in the active arm. Ring resonators consist of a bus waveguide and a ring-shaped waveguide. The input light from the bus waveguide couples to the ring shaped waveguide and interferes with itself. When a resonant condition is met, the light stays in the ring and does not pass through the bus waveguide. Changing the active material deposited on top of the ring waveguide changes the resonant condition and allows the light to pass.

Due to silicon’s weak electro-optic effects, silicon electro-opitc modulators historically have been relying on carrier depletion/accumulation or diffusion effects in p-i-n junctions [5, 41–44]. Forward-biased p-i-n junctions operate using carrier injection based on carrier diffusion and are fundamentally limited by carrier lifetimes in silicon. Certain approaches like carrier sweeping have helped these kind of devices to achieve GHz switching speeds

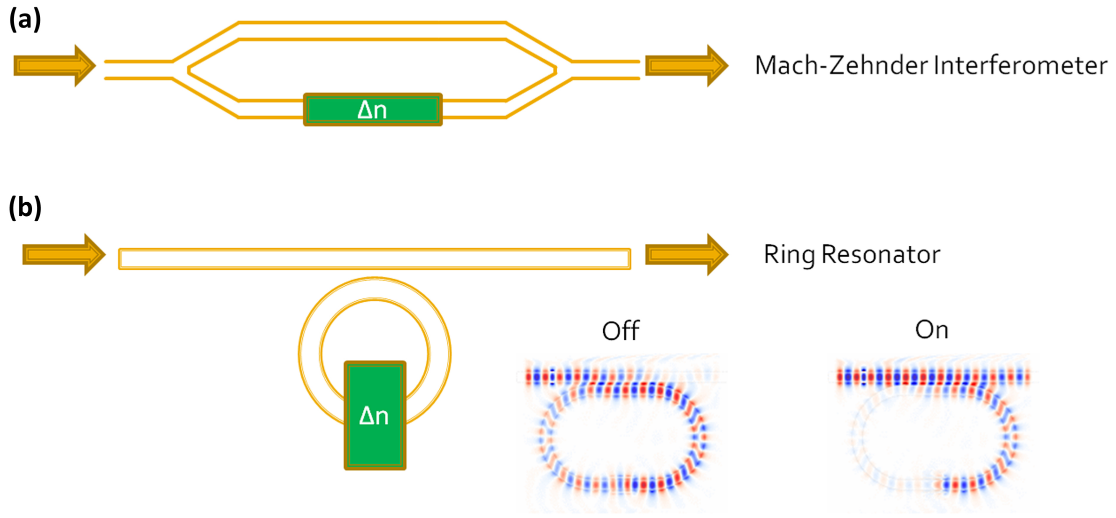

Figure 1.5: A schematic of (a) a Mach-Zehnder interferometer (MZI) and (b) a ring resonator with an image of electric field in the ON and OFF states

[5]. The carrier depletion devices operate using reverse bias p-n junctions, where the width of the depletion region is varied in order to influence the optical properties of the modulator. This type of modulators is a lot faster and has achieved modulation speeds of ∼50 GHz [45].

Although stronger than electro-optic effects, carrier dispersion effects are still relatively weak in silicon [30]. So utilizing them requires a clever approach: the light has to interact with the active medium (p-i-n junction) for a long time, which is achieved by either modulators being rather large (Fig. 1.6(a)) or resonant (Fig. 1.6(b)). The resonant modulators rely on confining the light to the cavity with an active medium for a period of time proportional to the quality factor (Q-factor) of the resonance. As the carrier dispersion effect is rather weak, the time light is confined in the cavity is very long and so are the Q-factors. High Q-factor cavities are easily affected by slight changes in temperature because of the strong thermo-optic effect in silicon. Thus even though silicon modulators are capable of modulation speeds up to 50 GHz [8], they are too large or temperature-sensitive for integrated photonic circuits.

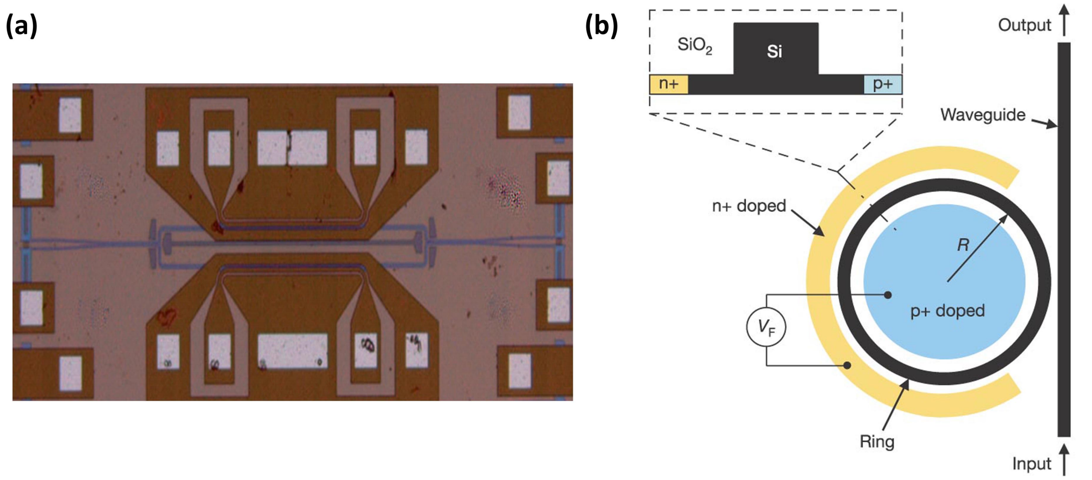

Figure 1.6: (a) A microscope photograph of a silicon Mach-Zehnder interferometer electro-optic modulator from ref. [4] (b) Schematic of micro-scale ring resonator electro-optic modulator from ref. [5]

Electro-optic modulators that are more compact and less temperature-sensitive than silicon devices can be made from binary or ternary III-V materials (e.g., GaAs, InGaAs) [46] and lithium niobate [47]. However, compatibility with silicon is essential for most on-chip applications; hence hybrid structures have been proposed that overcome the intrinsic limitations of silicon optical modulators and maintain CMOS compatibility, while adding another material with synergistic properties. For example, organic non-linear polymers with large second-order nonlinearities [48, 49], graphene [50], and vanadium dioxide (VO_2) [9, 14, 15, 51, 52] have been combined with silicon modulators to achieve improved performance. Out of these materials, VO_2 is the only one readily compatible with CMOS fabrication and therefore was chosen for investigation in this work. Basic properties of VO_2 are presented in the next section (Sec. 1.3.1).

While both rack-to-rack and on-chip interconnects can benefit from the hybrid modulator approach, on-chip modulator size needs to be reduced further. Size minimization can be achieved by using plasmonics which allows sub-diffraction limit light confinement and has been shown to shrink the size of non-hybrid devices [53]. Despite the advantages of plasmonics in shrinking size of the devices, there are trade-offs to be made, such as additional loss encountered by the metals. This issues are introduced in section 1.3.2.

1.3.1 Vanadium Dioxide: a Smart Optical Material

One family of proposed complimentary material systems consists of strongly correlated materials, with band structures that are strongly dependent on electron-electron interactions and give rise to the phenomenon of reversible solid-solid phase transformations. Among the correlated insulators, many transition metal oxides exhibit first-order, thermally driven semiconductor-to-metal transitions (SMT) of a particular interest for modulator applications. Vanadium dioxide (VO_2) is especially interesting for photonic and electronic applications because its transition occurs around room temperature (68°C) and is accompanied by a large change in electrical and optical properties. In addition to temperature, the SMT can be triggered by strain [54], electrical excitation [55–57], optical excitation [54], and hot electron injection [58]. The SMT occurs on the time scale of femtoseconds for optical excitation.

The nature of the SMT in VO_2 has long been disputed. The discussion is still ongoing with certain work pointing towards Mott-like behavior where the electron structure change initiates the movement of the atoms in the crystal lattice, and other work pointing to phonon-lattice interactions being responsible. The semiconducting room temperature phase of VO_2 has a monoclinic (M1) structure (Fig. 1.7(a)), while the metallic high-temperature phase has a rutile crystal structure (Fig. 1.7(c)) [6]. It has been recently shown that there is a monoclinic metallic phase (M2) of VO_2 that forms under certain excitation conditions (Fig. 1.7(e)) [59–61]. While M1 and R phases have very different electrical and optical properties (Fig. 1.7(b,d)), the relatively large difference in crystal structure implies relatively slow phase transition. The latest research allowed to differentiate between M1, M2, and R phases and showed that upon optical excitation the electronic structure changes immediately and the band gap closes, followed by slower structural transition on the time scale of picoseconds [59]. The time scales of the reverse transition from R to M1 phase is also a subject of ongoing research, but scientists agree that the reverse transition takes longer than the M1-R transition [62, 63].

This research is very relevant for optical modulators as it is highly desirable to have ultrafast switching times for both M1-R and R-M1 transitions. If it is possible to drive VO_2 to the M2 phase that has metallic behavior and does not require the long relaxation time, THz modulation speeds are achievable.

Fig. 1.8 shows a typical temperature hysteresis loop for VO_2 in both reflectivity [9] and resistance [10]. At room temperature, VO_2 is a semiconductor with a large bandgap and refractive index of 3.25 near 1.55 μm; above 67°C, it becomes a metal with a refractive index of approximately 1.9 near 1.55 μm [54]. The reflectivity changes due to thin film interference and increased absorption in the metallic state. Resistivity changes several orders of magnitude when the SMT is triggered by temperature. While when SMT is triggered by an optical signal, it occurs on time scales of femtoseconds but electrical triggering has been shown to be slower. The fastest reported switching values with a DC voltage are on

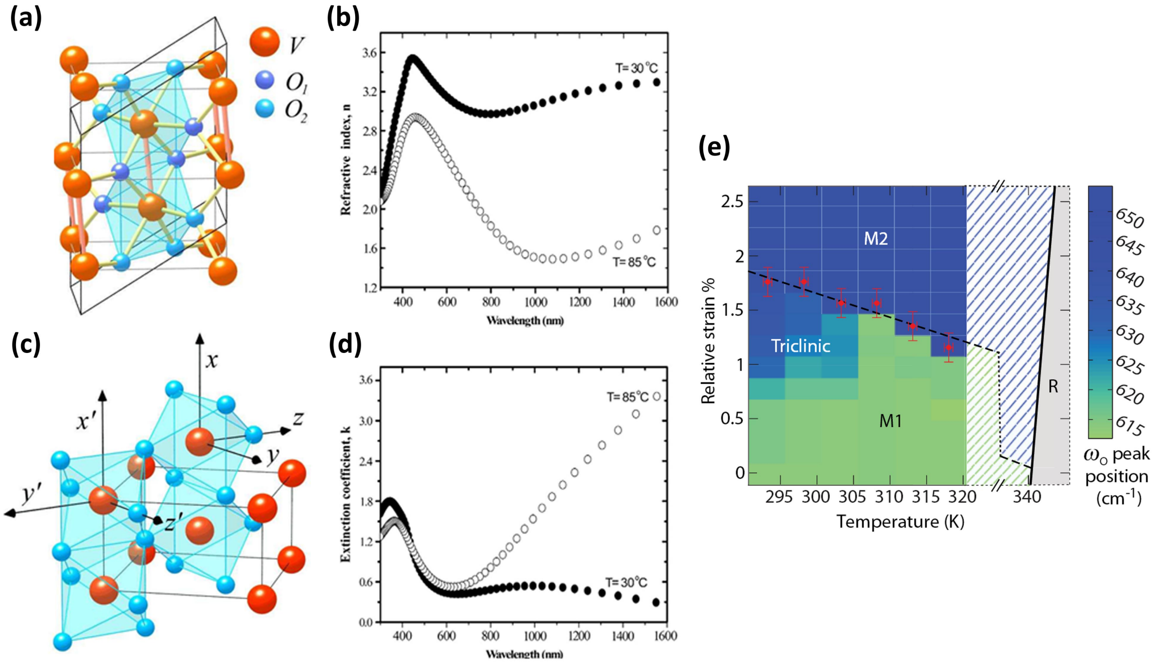

Figure 1.7: (a) Schematic crystal structure representation (adopted from ref. [6]) and (b) refractive index as a function of wavelength (adopted from ref. [7]) of monoclinic semiconducting phase of VO_2; (c) Schematic crystal structure representation (adopted from ref. [6]) and (d) refractive index as a function of wavelength (adopted from ref. [7]) of rutile metallic phase of VO_2; (e) phase transition diagram for VO_2 (adopted from ref. [8])

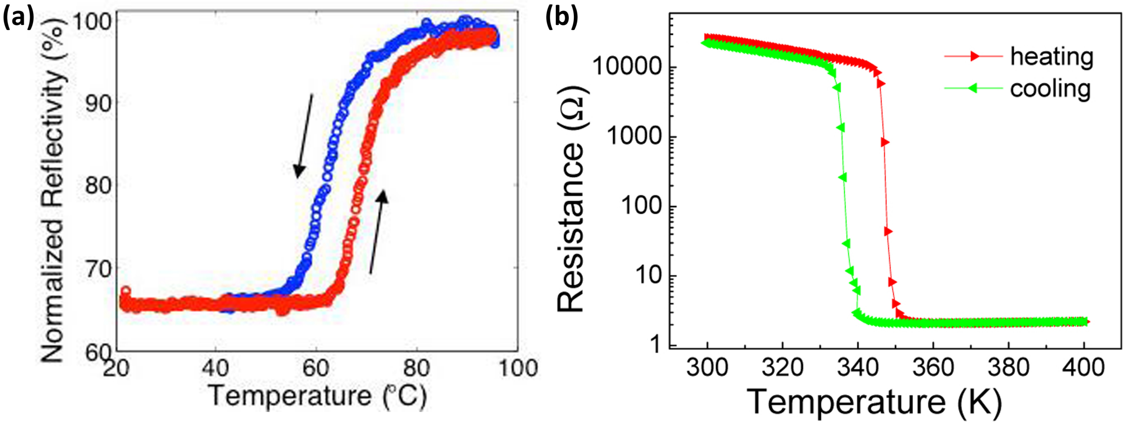

Figure 1.8: VO_2 (a) normalized reflectivity and (b) resistance as a function of temperature showing hysteresis behavior. Images adopted from [9] and [10] respectively.

the order of nanoseconds [56]. Switching values as fast as 9 ps have been demonstrated using terahertz field excitation in conjunction with metamaterials [62]. Electrical switching is discussed in detail in Chapter 3

1.3.2 Plasmonics: a Way to Achieve Smaller Footprints

Plasmonics provides a way to confine light to sub-wavelength dimensions and has been used to effectively shrink the size of optical devices, including electro-optic modulators [53, 64–66]. Plasmonics studies the interaction of light with metallic particles and surfaces. Generally, there are two types of plasmonic phenomena: propagating plasmons and localized plasmons.

Surface propagating plasmons (SPP) are collective photon-electron surface waves that at certain conditions can propagate along metal-dielectric surfaces. Besides sub-wavelength confinement to the surface, SPPs have very large group effective index. In electro-optic modulators large group index means that the light can more strongly interact with the active medium. The dispersion relation for propagating surface plasmons is given by:

$$k = \frac{\omega}{c}\sqrt{\frac{\varepsilon_1 \varepsilon_2}{\varepsilon_1 + \varepsilon_2}} \tag{1.4}$$

where ε_1 and ε_2 are permittivities of metal and dielectric, ω is the angular frequency of light, and k is the wave vector. If the metal permittivity is modeled with a free-electron model without attenuation the wave vector goes to infinity approaching the metal plasma frequency. Practically, attenuation is always present and therefore the wave vector is just maximized around the plasma frequency.

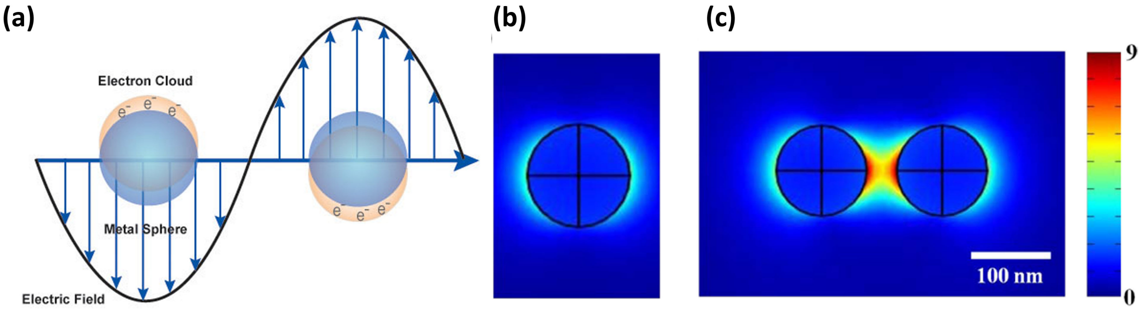

Figure 1.9: (a) Illustration of the interaction of electric field of incident light wave with the electron cloud. Electric field distribution of a (b) single plasmonic particle and (c) plasmonic dimer when light of resonant wavelength is incident. (b) and (c) are adopted from [11]

While propagating surface plasmons propagate on metal-dielectric surfaces, localized plasmons (Fig. 1.9(a)) are bound to sharp edges of metal structures and have even higher field intensities [67]. Localized surface plasmons are created at the surfaces of metallic particles due to electron cloud oscillations caused by the incident electro-magnetic wave (Fig. 1.9(b)). The schematic representation of this phenomenon is shown in Fig. 1.9(a). The localized plasmon results in extremely high electric fields near the surface of the metal which can significantly improve light-matter interaction for electro-optic modulation. This effect has been used in solar cells [68], light waveguiding [69], and localized heating [70].

If particles exhibiting localized plasmonic resonance are placed in close proximity to each other, they form a coupled dimer resonance (Fig. 1.9(c)) [67]. The electric field is further enhanced between particles, creating ”hot spots”. The enhancement is not linear and is the highest for smallest gaps between particles. Although localized plasmons are typically bound to particles, in multi-particle chains the energy can be transferred from particle to particle [69]. Essentially this phenomenon is a coupled resonance but it can be used for waveguiding. Compared to plasmonic films, guiding plasmons through particles is potentially more effective for modulator applications as the light is largely concentrated in the dielectric material between particles, which can be active.

However plasmonic modulators suffer from very high insertion losses and also are quite complicated to fabricate. It is generally accepted as a fact that it is not viable to transfer information using plasmons on-chip [71]. Photonics is a much better way to transfer information, but plasmonics can help shrink the size of active devices. This means that photonic and plasmonic components need to be combined on chip. Photonic-plasmonic mode conversion has already been addressed in a number of articles [72, 73], therefore we incorporate these couplers in our plasmonic modulator design. Alternatively, hybrid plasmonic waveguides can be constructed to reduce the propagation loss [73]. In this case the hybrid material is a dielectric with a lower refractive index than the base dielectric and is placed between base dielectric and metal. The hybrid plasmonic mode is pulled further away from the metal and mostly concentrated in the lower-index dielectric. This way the absorption from the metal is mitigated. Our plasmonic modulator design utilized both a hybrid plasmonic mode and a hybrid active material (VO_2). The design is described in Chapter 4.

1.4 Overview of the Dissertation

The objective of this dissertation is to contribute to the body of knowledge on optical interconnects and to make major improvements in the design and performance of two main building blocks of optical interconnects. Chapter 2 describes in detail how a compact and efficient fiber-to-chip coupler can be designed using the transformation optics design approach. Transformation optics allows for perfect in-plane mode conversion and excellent impedance and mode matching. Experimental measurements are provided proving the validity of this design. The challenge of creating compact and efficient electro-optic modulators is addressed in Chapter 3. The behavior of vanadium dioxide is investigated in a hybrid silicon environment, namely the ability of vanadium dioxide to undergo the semiconductor-to-metal phase transition under electrical stimulus. Modeling and experiment are presented tracking the spatial and temporal propagation of the phase transition through a microscopic VO_2 patch. Chapter 4 introduces an approach to shrink the footprint of electro-optic modulators by presenting a novel design of a hybrid Si-VO_2-Au plasmonic electro-optic modulator. The hybrid plasmonic modulator is simulated and compared to the state-of-art modulator designs. Chapter 5 summarizes the finding from this body of work and proposes directions for future research.

CHAPTER 2

IMPROVING FIBER-TO-CHIP COUPLING USING TRANSFORMATION OPTICS

2.1 Overview: Fiber-to-Chip Coupling

For many years, one of the biggest challenges in silicon photonics has been generating light on-chip due to the indirect band gap in silicon [19]. While on-chip light sources have been developed in recent years [28, 32], they remain relatively inefficient and challenging to fabricate. While research aiming to ease the fabrication and improve the efficiency of on-chip sources continues, off-chip light sources currently remain the preferred excitation method for photonic platforms. The off-chip sources, however, do not have the intrinsic advantage of on-chip sources, which are mode-matched to the on-chip photonic waveguides. Typically, stand-alone laser sources are either coupled to an optical fiber or free space. In either case, there is a substantial mode mismatch between the off-chip light sources and on-chip waveguides, preventing efficient coupling. For example, the smallest spot size achievable from commercially available off-chip lasers (using lensed fiber-coupled lasers) is typically $\approx 3\,\mu$m while silicon-compatible single-mode waveguides typically have dimensions of $\approx 500\,\text{x}\,250\,$nm [74]. In addition to the spot-size mismatch, the other important considerations for efficient off-chip to on-chip coupling are momentum and impedance matching to suppress reflections.

Despite recent advances in on-chip laser sources, off-chip lasers remain more efficient. Because they are more efficient and versatile fiber-to-chip coupling is still needed for optical interconnect applications. In addition to providing a source of light for on-chip applications, fiber-to-chip couplers are essential for routing signals on and off chip for board-to-board interconnects. A number of solutions for coupling light on-chip have been developed and can be classified into out-of-plane and in-plane couplers, schematically pictured in Fig. 2.1 [13]. Out-of-plane couplers allow light propagating normal to the chip to couple into the on-chip waveguide. This configuration is particularly advantageous for high-throughput diagnostics of multiple on-chip components where light can directly be brought to the regions of interest on the chip. However momentum matching as well as spot size and impedance matching must be considered to achieve effective out-of-plane coupling.

In the case of in-plane couplers, light is coupled from the edge of the chip, automatically taking care of momentum matching. However, spot-size and impedance matching still must be addressed and light can only be coupled on-chip from the edge of the chip.

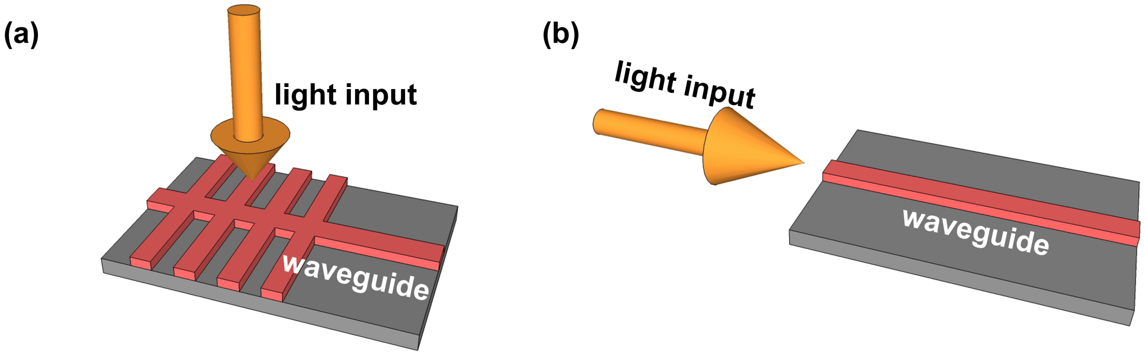

Figure 2.1: The schematic representation of (a) out-of-plane and (b) in-plane coupling.

The most common out-of-plane couplers are based on diffraction gratings, in which the light source often fiber-coupled is placed above the chip and light is incident near normal incidence to the plane of the chip [75–78]. The grating enables momentum matching for the out-of-place to in-plane light propagation direction. However, this conversion relies on diffraction which is described by following equation for normal angle of incidence of input light:

$$d sin \Theta_m = m\lambda \tag{2.1}$$

where m is an integer, λ is wavelength, d is grating pitch, and Θ_m is the angle of the diffracted light. It can be deduced from this equation that there are multiple diffracted beams, therefore in order to maximize the coupling careful design of grating pitch, height, and duty cycle is required.

Unless sophisticated designs are used [77, 78], there is a fundamental limit to grating coupler efficiency due to the fact that light is scattered from the grating in both the forward and backward directions. While the forward scattered light can be coupled to a waveguide mode, the backward scattered light is lost. In addition, grating couplers are typically designed for a single wavelength and angle of incidence, thus limiting their bandwidth of operation. These disadvantages are a major limiting factor for the use of out-of-plane couplers in integrated optics applications.

In-plane coupling is a more promising approach for integrated photonic circuits. The most prominent designs for in-plane coupling are based on the inverse taper geometry although a traditional taper can also work effectively for applications where length is not a constraint. Two examples of the inverse taper geometry are shown in Fig. 2.2 [12, 79–81]. In the simpler configuration, light is coupled from a fiber into a very narrow end of a tapering waveguide where the mode is initially delocalized before being smoothly converted in both mode field size and effective index along the taper to the high-index on-chip silicon waveguide. This simple and efficient coupler suffers from one major drawback: the facet of the chip has to be in a very close proximity to the coupler taper (1-3 μm), requiring precise polishing (Fig. 2.2(a)). In order to eliminate the need for polishing, another lithography step can be performed to deposit a spot-size converter, which is essentially a larger, lower refractive index waveguide typically made of polymer deposited on top of the taper. The light first couples to a large low-index spot-size converter, which increases the mode match to the fiber and helps with vertical mode conversion. Then the light from the spot-converter is slowly transfered to the inverse taper. While certain taper and spot-size converter combinations achieve insertion losses as low as 0.5 dB, they require multi-step lithography and extend over a long distance ($>$200 μm), occupying a large area on the chip (Fig. 2.2(b)) [13, 79]. Recently, improved tolerance to fiber misalignment was achieved by introducing a Luneburg lens to focus light into an inverse nanotaper; however, this method did not result in increased coupling efficiency and requires the use of a complicated greyscale lithography process [82].

In this work, we use a new approach to improve in-plane coupling and demonstrate an efficient, ultra-compact, and easy-to-fabricate coupler. This approach is based on transformation optics that allows to improve mode conversion efficiency and maintain mode and impedance matching. The basic design considerations are presented in next section (Sec. 2.2) before design of the new coupler is described (Sec. 2.3).

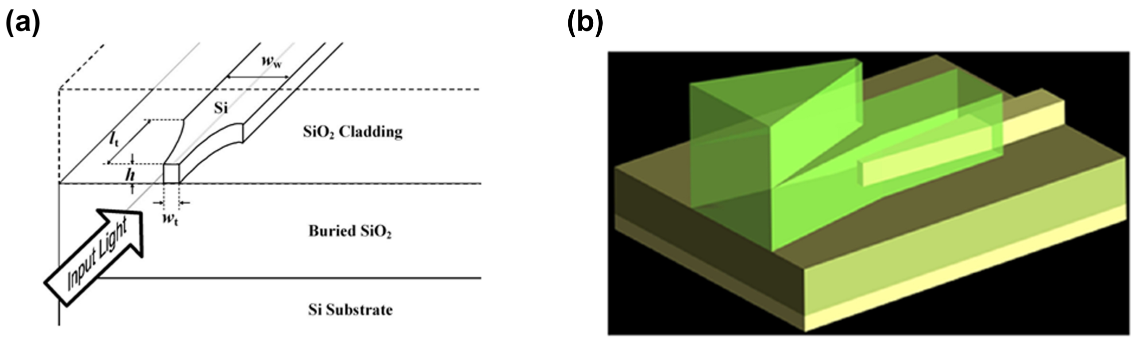

Figure 2.2: Examples of in-plane couplers: (a) nanotaper geometry from ref [12] and (b) planar fiber-to-chip coupler based on two-stage adiabatic evolution from ref. [13]

2.2 Overview: Transformation Optics

2.2.1 Mapping Techniques for Transformation Optics

In order to arbitrarily control the flow of light, one needs to have arbitrary control of both ε and μ tensors, which includes negative and infinite values. Unfortunately, the current state-of-the-art technology does not have capabilities to produce fully arbitrary optical properties. The design strategy therefore strives to avoid extreme values of refractive index and coordinate transformation becomes heavily reliant on the mapping technique. For instance, given the same boundary conditions, space itself can be modified in an infinite number of ways. Out of a variety of mapping techniques, conformal mapping is of the most interest as it minimizes the optical anisotropy yielding an isotropic material, which is much easier to realize [3].

Performing a coordinate transformation on Maxwell's equations, one can obtain the formula for the ε and μ based on the distortion tensor of transformed space. Mathematically the new ε and μ are described as following:

$$\varepsilon' = \frac{A\varepsilon_0 A^T}{detA} \tag{2.2}$$

$$\mu' = \frac{A\mu_0 A^T}{detA} \tag{2.3}$$

where $A_{ij} = \frac{\delta X_i'}{\delta X_j}$ is the Jacobian tensor. X' is the new coordinate superimposed on X, the old coordinate system and A defines the deformation field, determined by the mapping. For example if X is a two dimensional Cartesian space with a point represented by (x,y), or X_1 = x and X_2 = y, and X' is represented by (u,v), or X'_1 = u and X'_2 = v, then the deformation tensor:

$$A = \begin{pmatrix} \frac{\delta u}{\delta x} & \frac{\delta u}{\delta y} \\ \frac{\delta v}{\delta x} & \frac{\delta v}{\delta y} \end{pmatrix}$$

While these equations are general and work for all transformations, quasi-conformal mapping described by Chang et al. allows to minimize the off axis components and reduce A to a diagonal matrix [83]. Laplace equation is used to solve for the deformation:

$$\bigtriangledown_{X'} X = 0 \tag{2.4}$$

Equation 2.4 represents an inverse spatial transformation where the transformed space is mapped to the original. From a practical standpoint that means that the shape of the transformed space can be arbitrary and has to be mapped onto a rectangular uniform original space, making computation easier.

In order to implement a 2D transformation, where the original space coordinates are x and y and transformed space coordinates are u and v, using finite element method solver (COMSOL™), one needs to follow these steps: (1) define the transformed space; (2) create two Laplace equation solvers (for u and v); (3) create the Jacobian (A) from the data attained from the solutions of the Laplace equations. The detailed instructions for each step are included in the coupler design section 2.3.

2.3 Coupler: Design and Simulation

2.3.1 Transformation Design

The design of a transformation optics coupler includes three steps: (1) obtain the space distortion tensor from the transformation, (2) convert the space distortion to a permittivity profile, and then (3) represent the permittivity profile using Maxwell-Garnett effective index theory.

Step (1). Transformation optics can, in theory, provide a three-dimensional (3D) transformation that perfectly converts a Gaussian-like fiber mode into a mode of a rectangular waveguide through mode size and modal index matching. However, this 3D coordinate transformation requires permittivity and permeability tensors that vary in all three dimensions and would make the physical implementation extremely challenging with modern fabrication technology. A more realistic approach is the design of a coupler that only transforms light in the in-plane direction and accordingly utilizes a two-dimensional (2D) transformation. The design approach of converting a 3 μm transverse-electric (TE) fiber mode into a 500 x 250 nm waveguide mode is shown in Fig. 2.3(a). The transformation compresses physical space in the in-plane direction, squeezing the fiber mode profile into a ridge waveguide mode. The ridge waveguide mode is obtained from a standard single-mode waveguide on the silicon-on-insulator (SOI) platform. Similar 2D spot-size converters have been proposed but have not been implemented yet due to fabrication challenges associated with transformations resulting in complex anisotropic permittivity and permeability tensors [84–86].

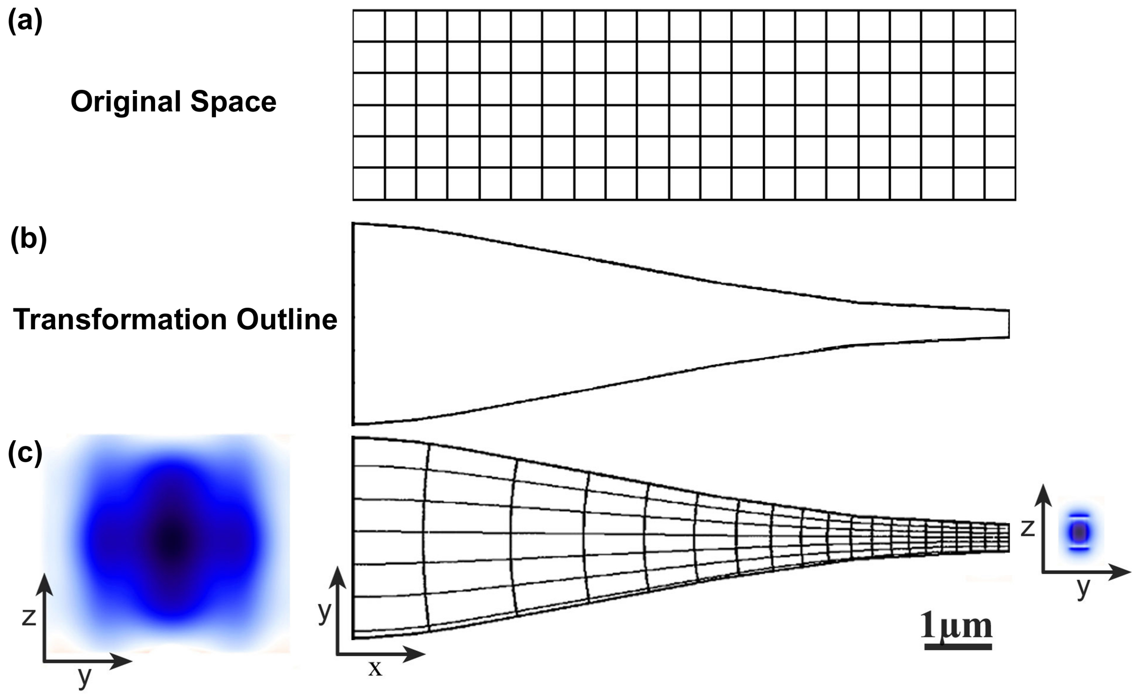

Figure 2.3: Original space pictured is the virtual space the light effectively sees, while the physical space tapers following the transformation outline. The bottom pictures fiber mode field profile is on the left and ridge waveguide mode profile on the right; darker color indicates higher intensity. Transformed coordinate system isolines, obtained by quasi-conformal mapping, are shown in the middle.

In order to reduce anisotropy in the transformation to yield isotropic material properties, a quasi-conformal mapping technique proposed by Chang et al. was used [83]. The technique utilizes the solution to the Laplace equation with sliding boundary conditions (the coordinate lines are orthogonal to the boundary rather than fixed at a certain value) which results in minimization of the anisotropy in the transformed medium for TE polarization, as discussed in section 2.2.1. The real space was chosen to taper from 3 μm to 450 nm over a distance of 10 μm, as shown in Fig. 2.3(a,b). This space was defined as a geometrical object in COMSOL Multiphysics™software and two Laplace solvers were added to the physics. The virtual space was chosen to be a 3 μm by 10 μm rectangle and was not defined in any way in COMSOL™, instead the dimensions of the virtual space were used to define the boundary conditions for Laplace solvers. The first Laplace solve was dedicated for calculating distortion in x, which was minimal because the real space coordinate did not need to compress along the direction of the coupler. In this case the vertical facets of the coupler had fixed boundary conditions (0 μm and 10 μm) and the horizontal lines had a sliding boundary condition (a.k.a Neumann condition). This boundary condition allows slipping and ensures that the coordinate system is perpendicular to the boundary: $\delta x/\delta n' = 0$. Likewise the second Laplace solver is setup mapping top and bottom boundaries to 1.5 μm and -1.5 μm respectively. For the second solver the vertical facets of the coupler are allowed to slip.

Step (2). Distorted coordinate system (Fig. 2.3(c)) was obtained from the results of the Laplace solvers. From the deformation tensor the ε and μ profiles are obtained using equations 2.2 and 2.3. These resulting profiles are strongly dependent on the shape selected for the coupler. As a general design guideline, the real space must avoid discontinuities in the first derivative of the boundary outline, as they cause singularities in the deformation tensor profile. Considering the range and the gradient of permittivity accessible for different coupling lengths, a 10 μm coupler length was selected as it offered the best balance between high coupling efficiency and low losses due to scattering. A smooth coupler

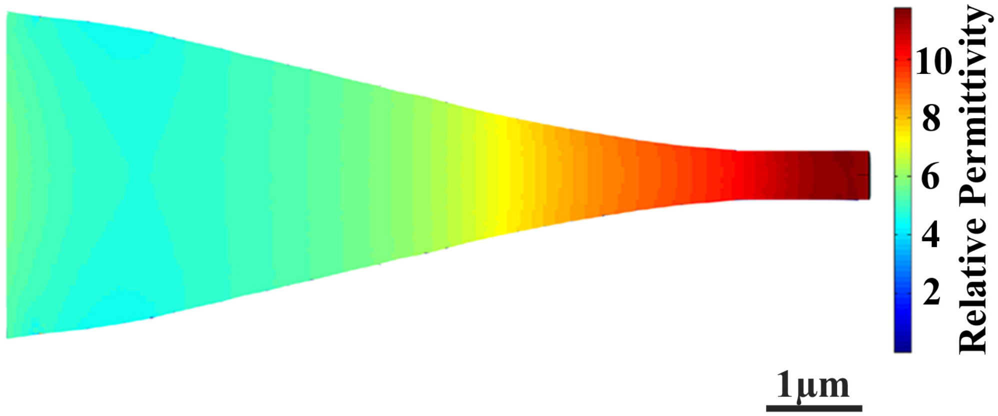

Figure 2.4: The permittivity profile profile obtained by a quasi-conformal mapping technique

shape consisting of 2nd and 3rd order Bezier curves was empirically determined to provide the most conservative ε and μ profiles. After determining the optimal shape of the coupler, one must account for the inability to modify the μ without introducing a magnetic material. Both ε and μ profiles were combined in a single refractive index profile and then matched to the input and output ports of the coupler. In order to match the output port, the highest refractive index was set to the refractive index of silicon (3.45). Ideally the refractive index of the input port should be set to 1 to match that of air, but it is impractical. Therefore the input side was matched to silicon dioxide with a refractive index of 1.45. In order to facilitate these matchings, the refractive index profile of the virtual space (ε_0) can no longer be uniform and is set to an exponential which ensures no reflections. The resulting ε profile is shown in Fig. 2.4.

2.3.2 Effective Permittivity Engineering

Step (3). There are several possible approaches to realizing a varying permittivity profile on SOI platform. The most popular approach utilizes an array of holes or pillars much smaller than the wavelength of light. This condition results in light ”seeing” an effective medium of some permittivity rather than a discrete array of objects. This effective permittivity can be modulated by varying the filling fraction of the unit cells. For instance one could either vary the size of the holes or pillars, or the spacing between them.

In this work, a hexagonal lattice of fixed diameter sub-wavelength air holes with varying filling fraction was employed [3]. The hole array is placed in the device layer of an SOI wafer and the spatially varying filling fraction was computed in order to most closely match the effective waveguide mode index to the permittivity profile dictated by the transformation. We chose to implement uniform-size holes with variable spacing owing to the more forgiving fabrication tolerances that this approach offers compared to fixed-spacing and arbitrary hole size [36]. Other methods of obtaining variable permittivity that use random hole placement either based on a probability function or a grayscale image have a lower resolution and therefore require a much smaller hole size in order to be effective [35, 87].

The Maxwell-Garnett effective medium approximation is good approximation for isolated cylinders embedded in another medium and was used to determine the desired filling fraction profile.

$$\varepsilon_{eff} = \frac{f\varepsilon_i a + \varepsilon_e(1-f)}{fa + (1-f)} \tag{2.5}$$

where ε_i is the permittivity of inclusion (air in our case), ε_i is the permittivity of the medium (silicon), f is the filling fraction, and a is the field ratio between two materials for TE-polarization defined by $a = \frac{2\varepsilon_e}{\varepsilon_e+\varepsilon_i}$. An algorithm (shown in Appendix A) was developed and implemented in MATLAB to determine the proper hole placement in the distorted lattice. The performance of the algorithm was evaluated by extracting the effective permittivity of the distorted lattice with the resolution equal to the hole diameter. The hexagonal lattice arrangement allows for maximum theoretical packing density (74 %) and therefore can achieve a greater range of permittivity values. For our design, the hole diameter was chosen to be 100 nm to ensure consistent hole-to-hole uniformity using standard electron-beam lithography processing. Reducing the hole diameter would lead to a more accurate permittivity profile, resulting in improved coupler performance. The final hole layout is shown in Fig. 2.5(a) overlaid with the permittivity profile.

The algorithm utilizes an iterative method to shift the hole positions according to the permittivity profile. (1) First, the permittivity profile is converted into a filling fraction profile. Then the filling fraction and desired hole size is used to determine the desired area around each individual hole. (2) A uniform hexagonal array of holes is generated with the hole spacing needed to represent the lowest permittivity in the profile and therefore the smallest spacing between holes. (3) The array is stretched hole-by-hole according to the area-around-the-hole profile using a built-in MATLAB function to determine the area around each hole. (4) The algorithm repeats itself until the areas around all holes are matched to the profile. The resulting permittivity profiles for 100 nm and 50 nm diameter holes are shown in Fig. 2.5(b,c) respectively.

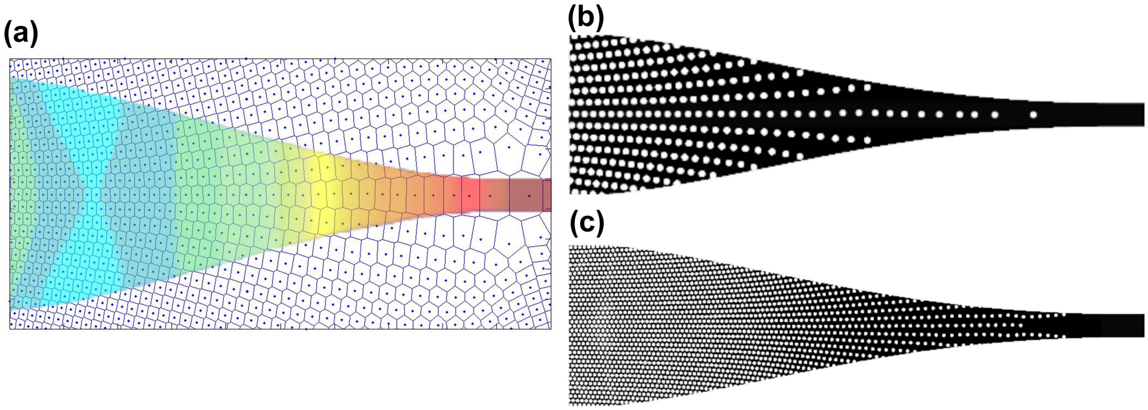

Figure 2.5: (a) The result of the custom MATLAB algorith visualized: the points represent hole placements, while the lines indicate the boundaries of areas around the holes; the permittivity profile is overlaid as a background. The permittivity profiles extracted from MEEP with (b) 100nm holes and (c) 50nm holes.

2.3.3 Simulated Performance

Initially the coupler performance was simulated with finite element method (FEM) using a qualitative approach. The mode was excited by a plane wave at the input port of the coupler and the excited fields were observed. The image of electric fields, presented in Fig. 2.6(a), represents one of the possible field distributions within the coupler at a random time. Because FEM is lacking the time component, quantifying the transmission performance from this approach is impractical, but it is an appropriate tool for gauging the transformation performance. In contrast with the designed TO coupler, the TO coupler outline without any holes has a significant portion of the electric field escaping the coupler.

In order to quantitatively verify proper operation of the TO coupler, in-plane mode conversion was studied by restricting the size of the out-of-plane input mode profile to match the height of the waveguide and coupler. To evaluate coupling efficiency, 3D finite-difference time-domain (FDTD) simulations were carried out for the coupler with the

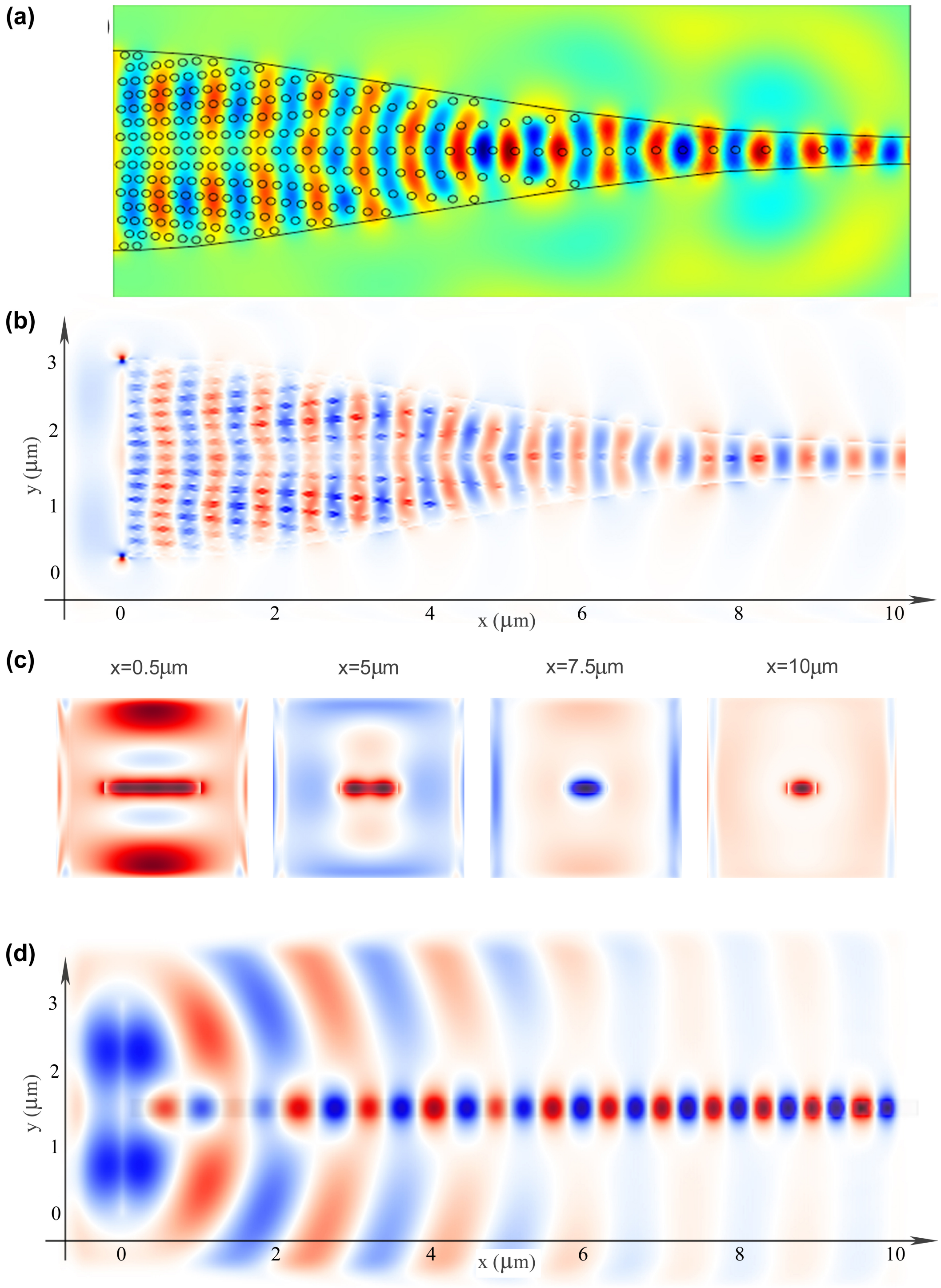

Figure 2.6: (a) Electric field (Ey) profile obtained from COMSOL FEM simulation, (b) Electric field (Ey) snapshot of the transformation-optical coupler with 100 nm holes demonstrating efficient in-plane mode conversion (top view), (c) Mode profiles at various points along the transformation-optical coupler with continuously-varying permittivity in 3D mode conversion, (d) Field (Ey) snapshot of the transformation-optical coupler with continuously-varying permittivity in 3D mode conversion (side view).

designed spatially varying hole profile using freely available software, MEEP [88]. A 3000 nm x 250 nm input rectangular Gaussian pulse was launched into the wide end of the coupler and the transmission was determined by accumulating flux through two planes, one at each end of the coupler. A Fourier transform was then performed on the resulting fluxes; transmitted power was determined by the ratio of the transformed output plane flux to the transformed input plane flux [88]. The mode conversion efficiency was nearly 100% for some wavelengths within the evaluated bandwidth (1500-1700 nm) (field snapshot shown in Fig. 2.6(b), transmission plot shown in Fig. 2.7). The origin of the oscillations in the transmission spectrum is discussed in the following section. In comparison, the peak efficiency of the TO coupler outline without holes was less than 85 % (Fig. 2.7), confirming that the transformation optics approach to in plane mode conversion works as designed. The TO coupler outline design provides mode size conversion but does not achieve modal index matching because its input port is solid silicon which has a much higher refractive index than the optical fiber. Several mode profiles at different positions along the TO coupler are shown in Fig. 2.6(c). Bending of the field can be observed at x=5 μm, illustrating how the light is compressed as it propagates inside the transformed coordinate system (Fig. 2.3).

Furthermore, to analyze the efficiency of the TO coupler for fiber-to-waveguide mode conversion (3D mode conversion), the input mode was approximated by a rectangular 3000 nm x 3000 nm plane wave centered in the middle of the coupler. Instead of the Gaussian-like field profile of a real fiber, the plane wave has a uniform field profile contributing to additional loss (illustrated in Fig. 2.6(d)) in the simulation. Despite this additional loss, the simulation results (Fig. 2.8) provide a good comparison between different coupler designs. For the butt-coupled waveguide (red curve) without any included transition region

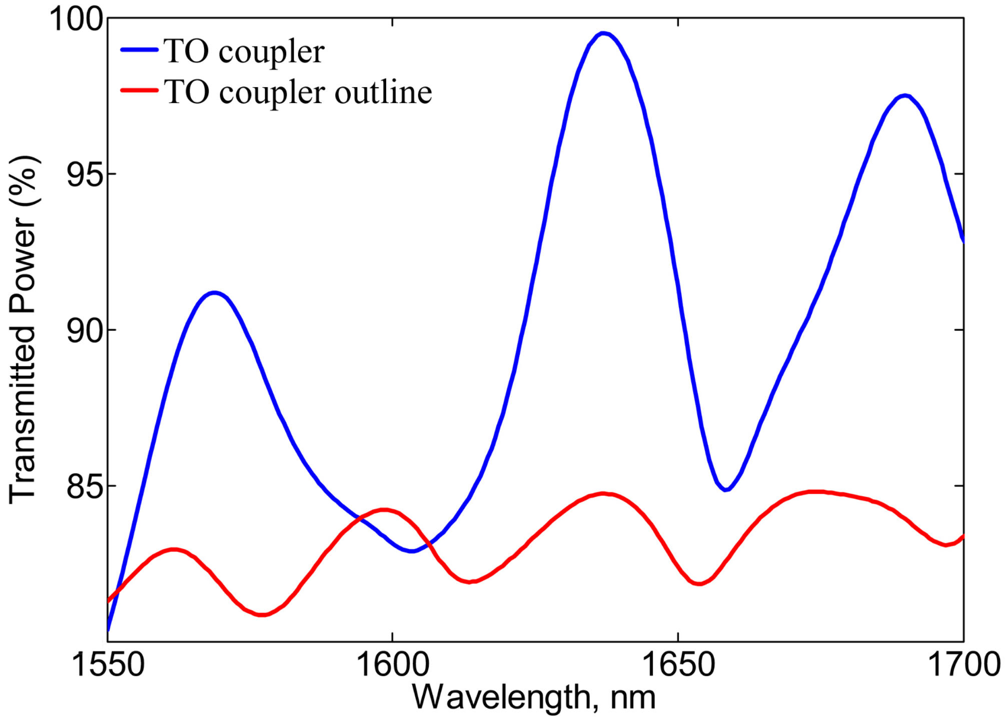

Figure 2.7: Simulated transmission plot for in-plane mode conversion for TO coupler and TO coupler outline without holes.

between the fiber and waveguide, an average transmission of 1 % was simulated, while for TO coupler with 100nm (Fig. 2.5(b)) holes a maximum transmission of 17 % was simulated (blue curve). In comparison, the TO coupler outline without any holes showed an average simulated transmission of 10 %. Due to the out-of-plane losses and inaccuracies in approximating the fiber mode in simulation, the maximum achievable transmission for our in-plane mode conversion TO coupler was found to be approximately 21 % by simulating a continuously varying index profile (”Perfect index” obtained directly from the transform) for the TO coupler. The previously mentioned oscillations present in the transmission curve of the 100 nm hole design are caused by discretization of the refractive index and resulting cavity effects and are greatly reduced by decreasing the hole size to 50 nm (Fig. 2.5(c)) (green curve) or restricting the transformed region (teal curve). These two approaches are discussed in detail in the experimental performance section, as this behavior was confirmed in experiment.

2.4 Coupler: Experiment

2.4.1 Fabrication

The coupler design was fabricated on an SOI wafer with a 220 nm p-type, 1422 Ω-cm resistivity, Si(100) device layer and 1 μm buried oxide layer (SOITEC). Electron-beam lithography (JEOL JBX-9300100kV) was performed using poly(methyl methacrylate) (PMMA) resist. After pattern exposure and development in methyl isobutyl ketone (MIBK) and isopropyl alcohol in a ratio of 1:3 (v/v), anisotropic reactive ion etching was performed (Oxford PlasmaLab 100) using C4F8/SF6/Ar process gases to etch the exposed portion

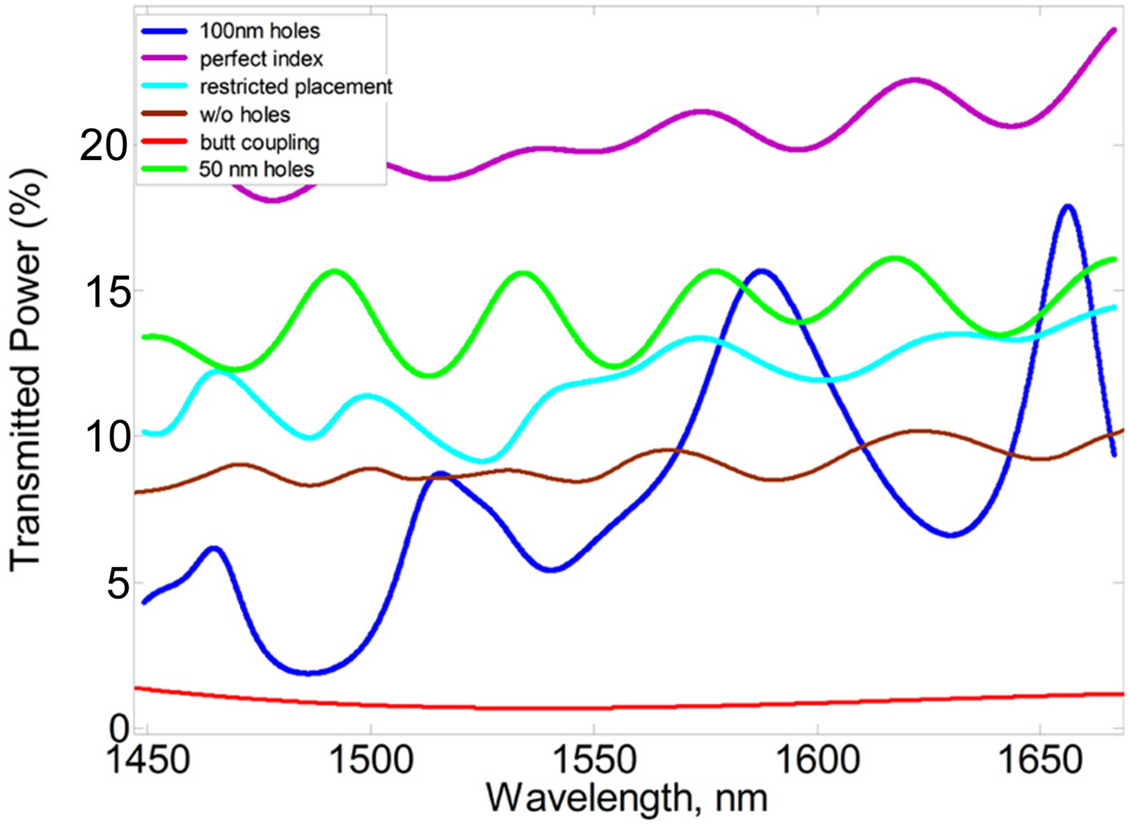

Figure 2.8: Simulated transmission plot for fiber-to-chip coupling for TO coupler with 50 nm (green) and 100 nm (blue) size holes and perfect permittivity (purple), TO coupler outline without holes (brown) and butt-couping (red) as a benchmark.

of the 220 nm Si layer. The 100 nm diameter holes with variable spacing were fabricated with relatively low size deviation due to proximity effects. In addition to the TO coupler (Fig. 2.9(a)), several other geometries were fabricated for performance comparison: waveguides without a coupler, TO coupler outline without holes, and a TO coupler with holes only in the wider (x = 0-5 μm) region (Restricted placement). After etching, the chips were masked with a thick PMMA protective layer (to protect from polishing debris sticking to the devices) and then cleaved and polished down to the couplers on one side and cleaved through the waveguides on the other. The PMMA protective layer was removed with ultrasonication in acetone before measurements were performed.

Larger hole sizes were easier to fabricate consistently and uniformly than smaller ones. Diameter uniformity of the holes was critical for producing an accurate permittivity profile, which is essential for an effective device. Extensive dose tests were performed in order to fine tune the fabrication of 100 nm holes. Initially ZEP 520 photo-resist was used due to its lower dose requirement and therefore shorter electron beam write times. However, this very property of ZEP resist was ultimately it's limiting factor. When the critical dose is low, the secondary electron proximity effect has a significant contribution to the effective exposure dose. This proximity effect is hard to predict and contributes to the hole size distribution, which we strive to minimize. PMMA A4 950k resist however has approximately three times higher critical dose and is more resistive to secondary electron proximity effects. PMMA thickness, spun at 2000 rpm, measures around 300 nm, making the smallest achievable hole size using JEOL JBX-9300 around 30 nm. The smallest hole size was determined experimentally and is affected by following factors: accelerating voltage, electron focusing, resist forward electron scattering, critical dose, and development parameters. This is the smallest achievable size, without taking uniformity and hole circularity into account. Considering those factors, even hole sizes on the order of 50 nm were not practical in our design. For experimental measurements, 100 nm hole diameter was selected as it further relaxes fabrication tolerances and allows the focus to be on design rather than fabrication.

One of the major advantages of this TO coupler is that the 3 μm wide end of the coupler could be extended to eliminate the need for polishing, although additional transmission losses would be incurred through that section. In order to accurately determine the performance metrics of the couplers in this experiment, a polishing step was performed to allow off-chip light to be directly coupled into the TO coupler. First, the chips were cleaved as close to fabricated couplers as possible. in the best cases, the cleaving plane was within 100 μm of the coupler. Then, a fine grain polishing wheel was used to remove the excess silicon. The polishing process was performed manually. The chip was held perpendicular to the polishing wheel for about ten second increment. Between each increment the edge was inspected in a microscope with a 100X objective.

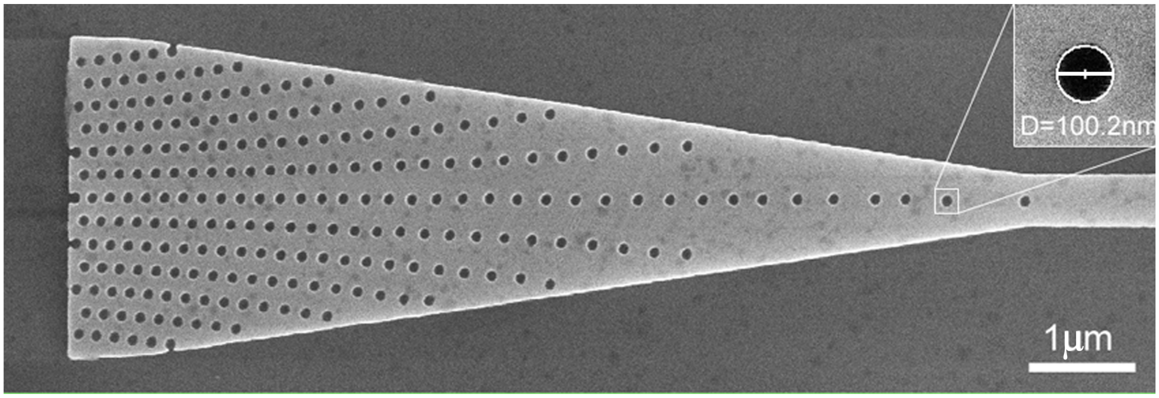

Figure 2.9: Scanning-electron microscope image of TO coupler.

2.4.2 Experimental setup

Experimental data was obtained using a lensed polarization-preserving fiber to couple light into and out of the waveguides. The setup is pictured in Fig. 2.10. Measurements were performed using a broadband TE-polarized LED source (Agilent™83437A, 1500-1700 nm) and an optical spectrum analyzer (Agilent™86140B). For higher resolution measurements, a tunable TE-polarized laser source (Velocity™6328, 1520-1570 nm) and a broadband photodiode (Newport™1835-C) were utilized. The light source (Agilent™83437A or Velocity™6328) is coupled to an optical fiber and passed though a TE polarizer. The tapered tip of the fiber is then brought in close proximity to the TO coupler input using a 3-axis piezoelectric stage. The position of the input fiber tip is then optimized using an infrared camera by maximizing the light coming out of the output waveguide of the coupler. Next, an output fiber coupled to a photodetector (Newport™1835-C) is brought in proximity to the waveguide output and its position is optimized by maximizing the measured transmission. With the measurement setup properly aligned, the performance of the couplers was evaluated by measuring the transmission spectrum of each coupler. Depending on the resolution and bandwidth requirements for the measurement, either the tunable laser was scanned across multiple wavelengths with the coupler transmission measured by the photodetector at each wavelength or the broadband LED source was used with the spectrum analyzer to capture the transmitted spectra. The use of input and output fibers allowed for a seamless transition between measurement setups without the need for complete realignment. In order to minimize the human error in measurement that is associated with the manual setup optimization, the data was averaged for three different couplers for both the TO coupler and all the control couplers. All of the couplers were located on the same chip and went through the same processing and preparation steps.

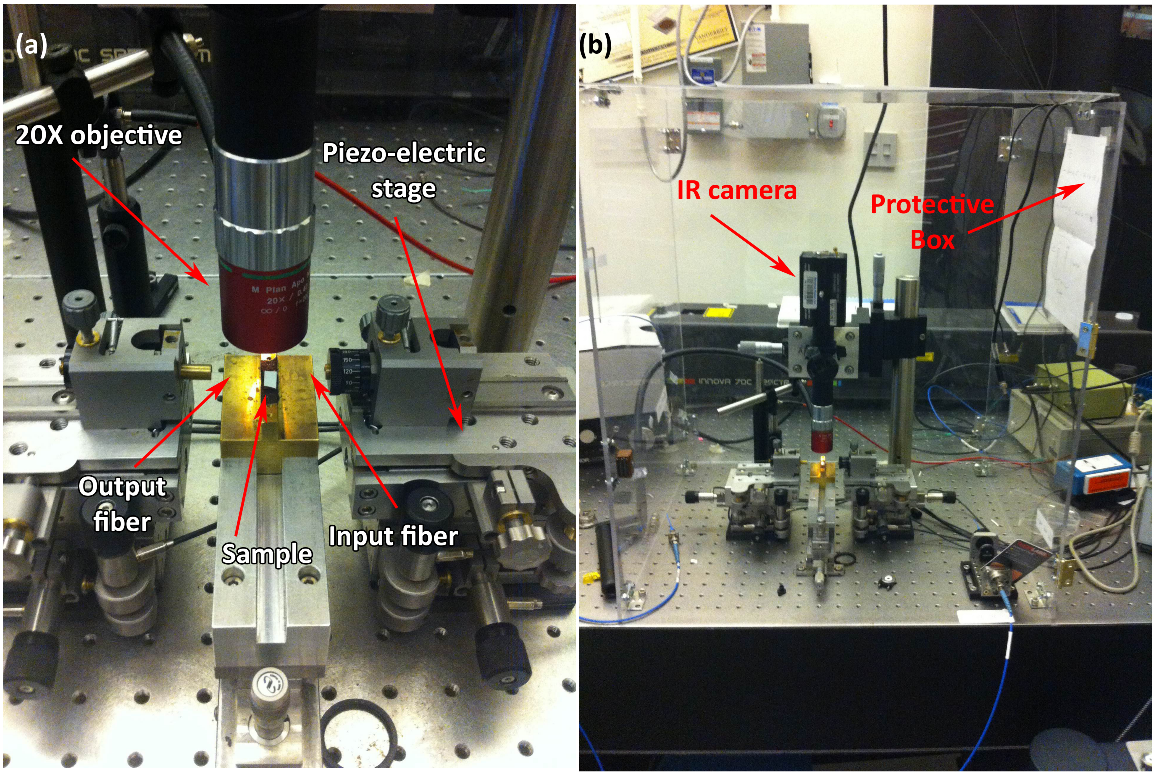

Figure 2.10: Measurement setup (a) zoomed in on the sample and (b) zoomed out. (a) Zoomed in image shows device under test (”sample”), input/output fibers mounted on piezo-electric stages, and a 20X microscope objective optimized for near-infrared transmission used for observation above the sample. (b) Zoomed out image shows the IR camera and the protective Plexiglas box around the setup to prevent interference from air currents in the room.

2.4.3 Coupler Performance

The simulation results (Fig. 2.11(a)) provide a good comparison between different coupler designs and match reasonably well with the experimental measurements (Fig. 2.11(b)). The slight differences between simulations and experiments are likely caused by fabrication errors, namely non-uniformity in the hole size and distortion in the hole shape. For the butt-coupled waveguide without any included transition region between the fiber and waveguide, an average transmission of 1 % was simulated and very low power was measured at the output of the waveguide. The fabricated TO coupler showed a peak 5-fold improvement over butt coupling in experiment for the design with 100 nm holes. A maximum transmission of 17 % was simulated. In comparison, the TO coupler outline without holes showed an average simulated transmission of 10 % and a 3-fold improvement over butt-coupling in measurement. Due to the out-of-plane losses and inaccuracies in approximating the fiber mode in simulation, the maximum achievable transmission for our in-plane mode conversion TO coupler was found to be approximately 21 % by simulating a continuously varying index profile (”Perfect index”) for the TO coupler.

Besides the lack of an out-of-plane transformation, the TO coupler efficiency is also affected by inaccuracies in replicating the designed permittivity profile. As shown in Fig. 2.11, the TO coupler efficiency varies with wavelength and does not match the efficiency of the continuously-varying index obtained directly from the transformation (perfect index). This inconsistency is due to the discretization in the refractive index profile caused by use of 100 nm diameter air holes. The discretization becomes more drastic in the narrow end of the coupler where the spacing between air holes is large enough to cause interference effects. Namely, the two holes at the end of the coupler, separated by about 1 μm, form a Fabry-Perot type structure, which exhibits similar oscillations to the ones seen in the TO coupler transmission. Furthermore, due to the strong field confinement in the narrow end of the coupler, small deviations in the lateral positioning of the holes in this section lead to large differences in the effective index of the mode, making it challenging to match the perfect index profile. These effects can be seen in both simulation and experiment, proving

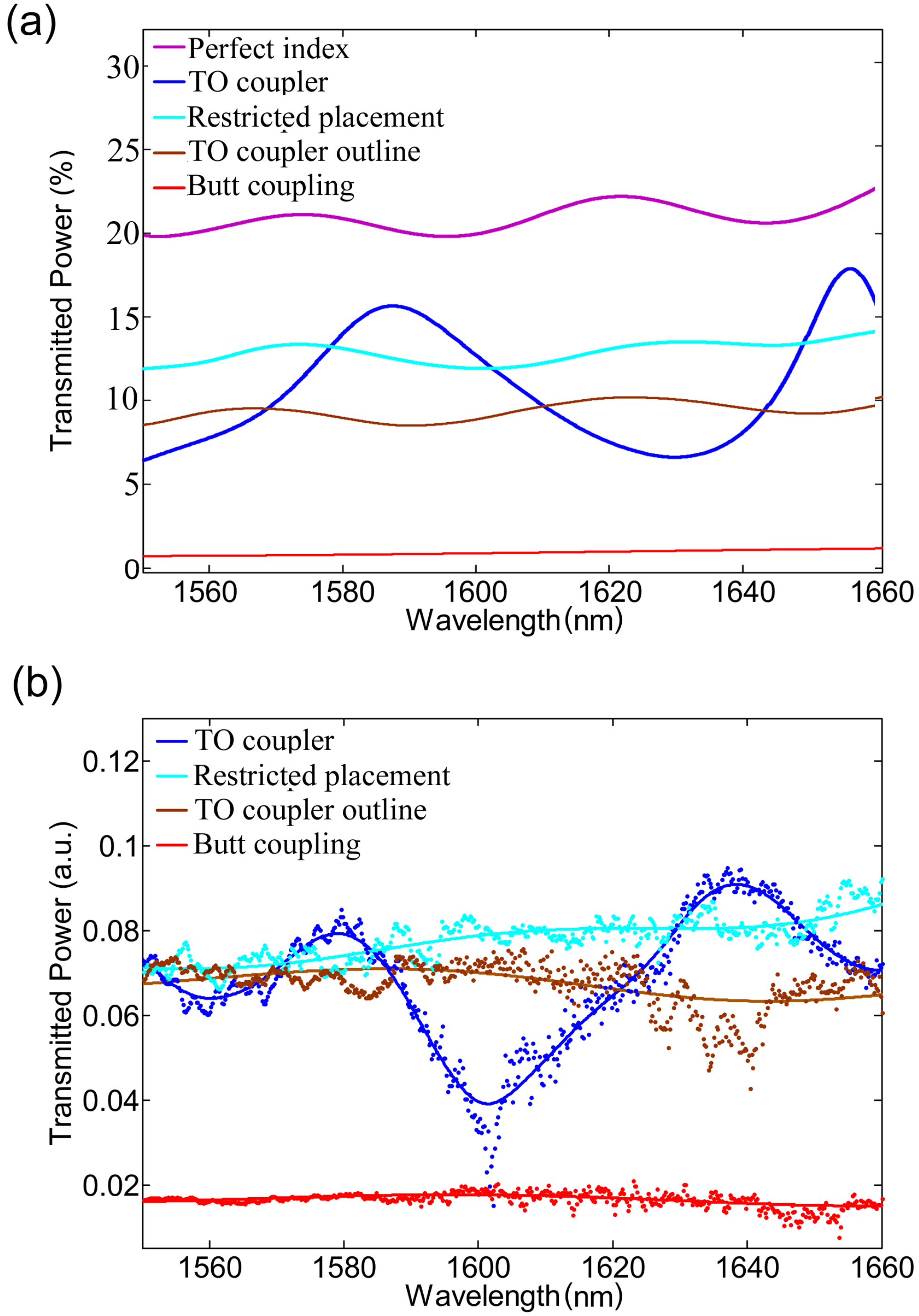

Figure 2.11: Plot of the (a) simulated power transmission and (b) experimental transmission through the couplers: TO coupler, TO coupler with holes present only in wider half of coupler (Restricted placement), and TO coupler outline without holes. For comparison, a coupler with a perfect refractive index gradient transformation was simulated and a butt-coupled waveguide without a coupler was simulated and experimentally investigated.

that they cannot be attributed to fabrication imperfections and therefore can be addressed in effective permittivity design step.

In order to demonstrate that the transmission curve for the TO coupler can be flattened to increase the wavelength tolerance of the coupler performance, two approaches could be taken: (1) eliminating the transformation in the narrow end of the coupler at the expense of peak coupling efficiency, and (2) reducing the size of the holes. The second approach will minimize the transformation errors due to the permittivity discretization but, because of the fabrication difficulties, it was investigated only in simulation (Fig. 2.8). The first approach was simulated and fabricated by removing all holes in the narrow half of the coupler (x=5-10 μm, "Restricted placement"), thus truncating the transformation. As shown in Fig. 2.11(b), this approach indeed demonstrated flattening of the transmission spectrum. The experimental transmission curve shows an increase with wavelength, which does not appear in simulation. One possible reason for this small discrepancy between experiment and simulation is the slight inhomogeneity in the hole profile, which causes stronger scattering from holes at shorter wavelengths.

2.5 Summary and Outlook

Transformation optics is a powerful design tool, which helped in this case improved the foot print and efficiency of fiber-to-chip couplers by a significant factor. The demonstrated experimental 5-fold improvement in coupling efficiency for the TO coupler compared to butt coupling (i.e. no coupler) justifies the additional fabrication complexity in many cases. Besides the performance improvement, the compact footprint and relative ease of alignment are highly beneficial to the TO coupler integration into future photonic circuits. The CMOS single layer design of the TO coupler can be easily fabricated on a large scale on the same layer as most photonic circuit devices (i.e., waveguides, modulators) [89].

Although photonic integrated systems would benefit from utilizing the proposed TO coupler design, in an academic research environment, the fabrication tolerances for hole size and position make it somewhat impractical to implement for testing other devices. Often, in the basic research environment, sub-optimal coupling can be overcome by simply increasing the input power to compensate for coupling losses unless nonlinear effects are introduced. One of the byproduct research results from this project is that the control structure of the TO coupler outline also was found to performs much better than butt coupling. The TO outline fabrication is significantly more straight forward and simpler than the TO coupler as it does not require holes of accurate diameter and placement. Moreover, the transmission curve of the TO coupler outline is much flatter than that of the TO coupler, improving the bandwidth. Therefore the TO coupler outline is an excellent candidate for the use the in research environment and in fact is now used for a number of projects in our lab, including the hybrid Si-VO_2 electro-optic modulator described in the following chapter (Chapter 3).

CHAPTER 3

OPTICALLY INVESTIGATED ELECTRICALLY TRIGGERED PHASE TRANSITION IN VANADIUM DIOXIDE

3.1 VO_2 for Modulation Applications

Electro-optic modulators are essential components in the grand scheme of optical interconnect realization. The purpose of an electro-optic modulator is to convert electrical signals coming from the electronics layer to an optical signal suitable for signal transmission. Analogous to radio frequency electro-magnetic waves, light can encode the information in a variety of ways. The two basic modes are by phase modulation and amplitude modulation. While amplitude modulation is realized by introducing a variable absorption medium into the system, phase modulation utilizes a material which alters the phase of light. In the simplest example, the phase can be detected by interfering the signal with a reference light of the same frequency and known phase. The two modulation approaches, depicted in Fig. 3.1, typically require different types of active materials. Phase modulation is usually accomplished by a change in optical path length given by a change in the real part of the refractive index of the modulator material, while amplitude modulation is usually accomplished by changing the imaginary part of the refractive index of the modulator material. Vanadium dioxide (VO_2) is suitable for both types of electro-optic modulators as it experiences significant changes in both the real and imaginary parts of the refractive index across the phase transition [7].

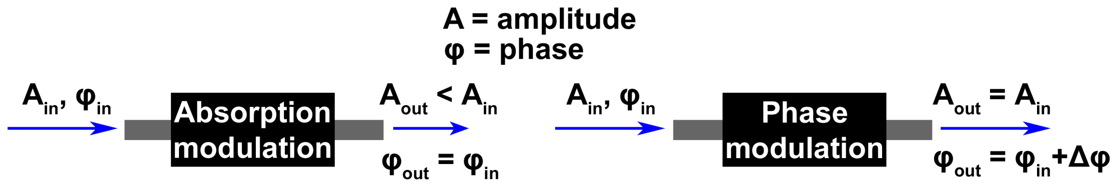

Figure 3.1: Conceptual representation of (a) absorption modulator and (b) phase modulator.

3.1.1 VO_2 Optical Modulators

VO_2 has been previously utilized in both amplitude and phase modulators. The first silicon optical modulator incorporating VO_2, described by Briggs et. al. in ref. [14], consisted of a patch of VO_2 deposited on top of a single mode SOI waveguide (Fig. 3.1(a)). The optical modulation was achieved by heating the entire sample above 68°C and therefore triggering the phase transition in VO_2. With VO_2 transitioned to its metallic state, absorption in the device was increased by about 3 dB, which is a respectable value for electro-optical modulators desired for optical interconnects. In this demonstration utilizing VO_2 as an active material enabled a three orders of magnitude reduction in the footprint of the modulator compared to silicon-only devices. However, the modulator switching time was very slow due to the thermal actuation.

The next generation of silicon modulators employing VO_2 was developed by Ryckman et. al. at Vanderbilt [9, 51]. These phase modulators used the large change in the real part of the refractive index following the VO_2 phase transition. VO_2 was deposited on a portion of a ring resonator structure, as shown in Fig. 3.2(b). When the phase of VO_2 is changed by local laser heating [9] or nanosecond laser pulses [51], the resonant condition in the ring changes inducing a large change in the transmission of the bus waveguide at a given wavelength, as illustrated in Fig. 3.2(d). This configuration allows for the insertion loss to be decreased dramatically and the modulation depth increased to 7 dB. In this work, the modulator switching time was commensurate with the full-width-at-half-maximum of the exciting laser pulse ($\sim$25 ns).

The two aforementioned experiments laid the ground work for future investigation of Si-VO_2 hybrid electro-optic modulators, but the devices in these experiments were not electro-optic modulators. In both experiments, it was not an electrical signal triggering an optical change, but rather a change in temperature either by thermal or optical heating. The next step in VO_2 modulator research was to integrate an electrical signal for triggering the phase transition in VO_2. In order to activate the phase transition based on an applied bias, Joushaghani et. al. used an integrated heater made of silver that also served as a plasmonic waveguide [15]. The device achieved high modulation depth (7 dB), but relatively slow modulation speed: 40 kHz. Since the voltage and resulting current are completely localized within the silver layer, electrical switching of VO_2, as considered by the VO_2 community, was not accomplished. Electrical switching of VO_2 is described in detail in the next section.

3.1.2 VO_2 Electrical Switching

Experiments investigating the underlying mechanism of the electrically induced semiconductor-metal transition (SMT) in VO_2 date back to 2000 when Stefanovich et. al. [57] reported that electric field or electron injection could induce the SMT in VO_2. They argued that their modeling showed that the leakage current was insufficient to raise the temperature of the device above the critical temperature T_c [90]. In the ensuing years, several groups have studied the electrically induced SMT in VO_2 and argued that the primary switching mech-

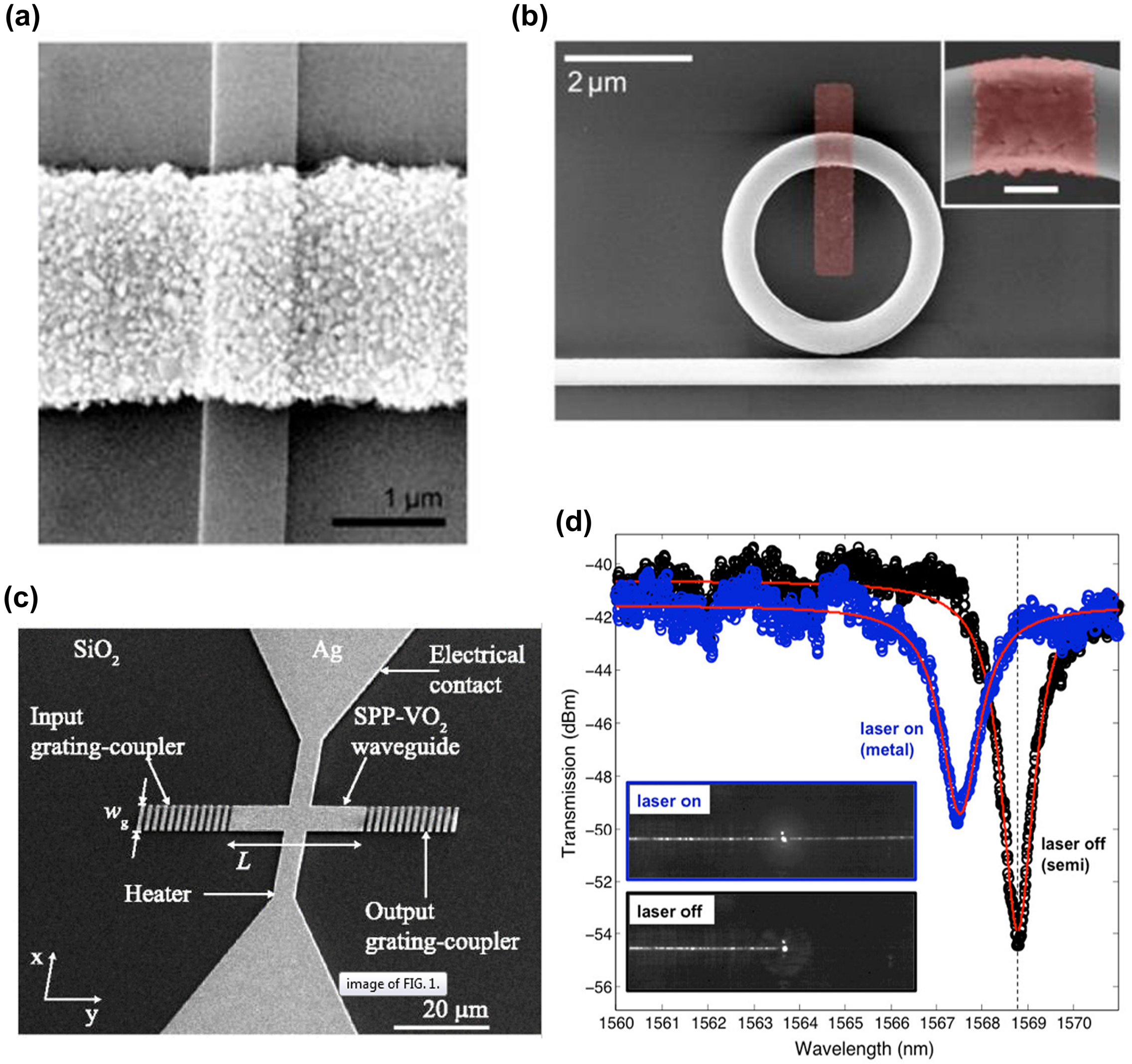

Figure 3.2: The SEM images of (a) a lithographically defined 2 μm-wide polycrystalline VO$_2$ tab across a Si waveguide from ref. [14], (b) a Si ring resonator modulator with VO$_2$ patch in false color (red) from ref. [9], and (c) a hybrid SPP-VO$_2$ switch with an integrated heater from ref. [15]. (d) Optical resonance spectrum for on and off states for hybrid Si-VO$_2$ ring resonator from ref. [9].

anism is electric field rather than Joule heating [56, 91]. The main argument for electric field triggering has been the relatively short time scale below 10 ns on which switching occurs [56, 91, 92]. However, if the SMT is indeed triggered by electric field alone, it should be possible to demonstrate switching in a field-effect geometry (Fig. 3.3(a)) with a high-k gate dielectric eliminating the leakage current. The field-effect geometry, also called a Mott-FET analogous to metaloxidesemiconductor field-effect transistor (MOSFET), has been explored [93, 94] but not fully demonstrated due to difficulties attendant to creating sufficiently strong electric fields ($\sim 10^7$ V/m) and the very short screening length in VO_2 (less than 1 nm) [93]. In order to overcome this roadblock, ionic liquids have been proposed as an alternative to the conventional gate dielectric. However, ionic liquid modulation is not suitable for high-speed operating devices and have been found to induce a reversible compositional change in the VO_2 films due to the formation of oxygen vacancies at the liquid-solid interface [95, 96]. In light of this failure to demonstrate pure electric field switching [97], an alternative explanation of carrier injection due to the Poole-Frenkel effect, as discussed in section 3.3.2, has been proposed and confirmed via modeling and experiment [93, 98] in a two-terminal device geometry (Fig. 3.4(b)). Although this field-assisted mechanism involves Joule heating, the thermal process is extremely fast ($\sim$10 ps), as has been shown by terahertz field excitation experiments [62], and therefore it is suitable for implementation in high speed electronic and photonic devices.

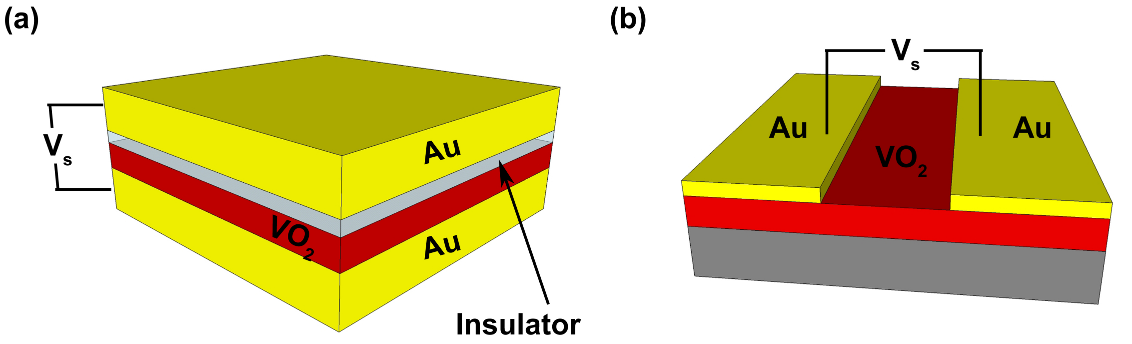

Figure 3.3: Schematic of an example (a) Field-effect switching structure and (b) two-terminal Joule heating structure.

3.2 Electro-Optic Hybrid Si-VO_2 Modulator

3.2.1 Modulator Schematic

In order to utilize the electrical SMT of VO_2 in photonic and electronic devices, further insight into the dynamics of the phase transition is needed. There has already been a significant effort to characterize the spatial evolution of the SMT at the nano-scale [99, 100] and micro-scale [101, 102] via AFM and Raman spectroscopy. These studies showed that the SMT does not occur simultaneously everywhere, but rather grain-by-grain and the semiconductor and metal phase can coexist in the same film. Here we present a novel way to characterize the VO_2 phase transition with nanosecond temporal resolution and tens of nanometers spatial resolution, which will aid in developing future electronic and photonic devices harnessing the SMT in VO_2. We employ a two-terminal configuration that allows for the application of a large electric field, but does not suppress leakage current. In order to distinguish the contributions of the electric field from Joule heating, we fabricate the in-plane VO_2 electrical switch on top of a single mode silicon waveguide. The optical measurements allow us to separate the measured optical signal from the electrical signal that triggers the phase transition, and then track the spatial and temporal evolution of the phase transition using both the experimental data and appropriate simulations.

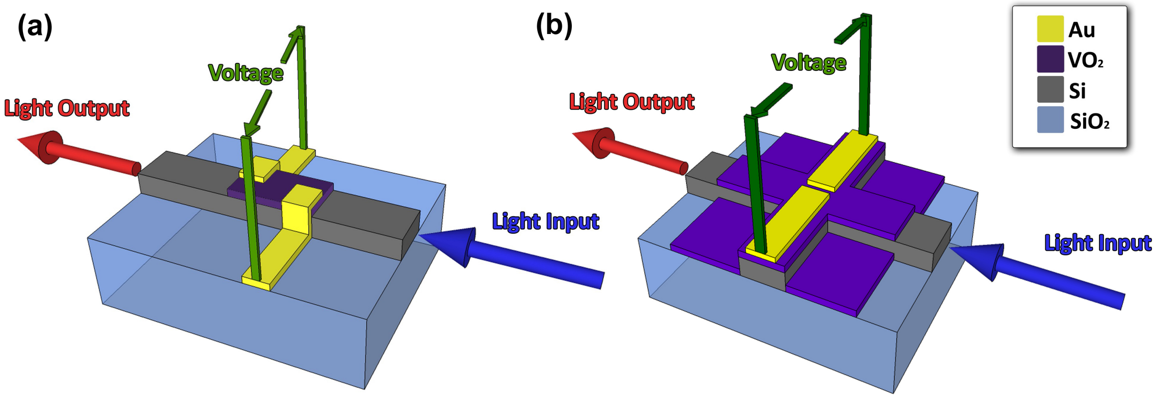

Figure 3.4: Schematic of the hybrid Si-VO_2 electro-optic modulator: (a) first generation and (b) second generation.

A schematic of the first generation of the Si-VO_2 linear absorption electro-optic modulator is shown in Fig. 3.4(a). A small patch of VO_2 was deposited on top of a single mode silicon waveguide, similar to ref. [14], and then gold contacts with a small gap on the order of 100-200 nm between them were deposited on top of the waveguide and VO_2 patch. This configuration is what was initially envisioned as a hybrid VO_2 electro-optic modulator. When a voltage is applied to the gold contacts, the VO_2 between the contacts is switched to the metallic state and a decrease in the optical signal in the waveguide is observed due to the increased absorption of light in the VO_2. This configuration requires the contacts to be continuous up the side walls of the waveguide, which turned out to be challenging to achieve and contributed to device failure as described in the following section. Therefore, in order to overcome this fabrication challenge, a second-generation device geometry was developed, shown in Fig. 3.4(b). In this geometry, the method and mechanics of switching are the same as in the first generation. The main difference is the inclusion of silicon supports for the gold contacts. While the silicon supports eliminate the challenge of gold deposition on a sidewall, they do create additional losses in the propagating mode. For the purposes of investigating the phase transition of VO_2, this second generation device geometry is suitable. For improved electro-optic modulator performance, additional design modifications could be made.

3.2.2 Fabrication: Lithography

Devices were patterned using electron beam lithography (EBL). EBL provides extremely high resolution (2 nm) and relatively high writing speeds (compared to focused ion beam (FIB) milling). In order to fabricate these devices, two EBL systems were used: a JEOL JBX-9300100kV at the Center for Nanophase Materials Sciences (CNMS) at Oak Ridge National Laboratory (ORNL) and a Raith eLine at the Vanderbilt Institute of Nanoscale Science and Engineering (VINSE). A three layer lithography was utilized, with second and third layers aligned to the first.

The first layer of lithography defined the silicon waveguide on a standard silicon-on-insulator (SOI) substrate (220 nm p-type,1422 Ω-cm resistivity, Si(100) device layer and 1 μm buried oxide layer (SOITEC)). The large scale writing was performed without alignment using the JEOL EBL system at CNMS/ORNL. The whole pattern was designed in L-edit software at Vanderbilt, and then the first layer was converted to a .v30 format that was accepted by the JEOL EBL. ZEP520A photoresist was spun at 6000 rpm for 45 sec and then baked at 180°C for 2 min to produce a resist layer around 300 nm thick. A dose of 300 μC/cm^2 was used to expose the resist at 30 kV voltage, 2 nA current, and 4 nm shot pitch. After exposure, the sample was developed in Xylenes for 30 sec and etched for 2 min using anisotropic reactive ion etching (Oxford PlasmaLab 100) with C_4F_8/SF_6/Ar process gases.

In addition to waveguides, the first EBL layer included global and local alignment marks for second and third layer alignment. The second and third layers were written using the Raith system at VINSE. Global alignment marks were placed outside the chip limits and were used to establish the chip local coordinate system. The EBL system recognizes the global mark positions from the design file. The job of the operator is to find those alignment markers on the sample. Once these global marks are found, the EBL software identifies the position of the beam in relation to the design file. Theoretically at that time, the sample is aligned and the second layer can be written, but there is an issue of stage movement. The stage is activated by a nano-manipulator and a laser controlled feedback loop. The movement of the stage is reasonably accurate, but stitching errors happen on occasion. This is where the concept of a write field comes in, which is one of the most important characteristics of a given EBL system. Stitching errors can occur at the edges of the write field. The dimensions of the write field are defined by the maximum deflection of the electron beam in the system. The Raith system at VINSE has an optimal write field size of 100 μm. If the write field is increased beyond that value, loss of resolution occurs. The JEOL system at CNMS has a standard write field size of 1mm, which allows it to write larger patterns more efficiently.

In order to do precise alignment for the modulator structures, an alignment process within each write field is required. Four local alignment marks for each write field are therefore present for every device. These alignment marks eliminate the error from stage movement, as they are used to modify the pattern of the electron beam deflection once the stage is immobilized in a process called write field alignment. Manual write field alignment entails the user picking the center of the alignment marks displayed on the computer screen, while automatic alignment uses a threshold algorithm to determine the center of the alignment marks. This lithography and automatic alignment process was used to define mask openings for both VO_2 and gold depositions for the second and third layer lithography of the Si-VO_2 electro-optic modulator fabrication.

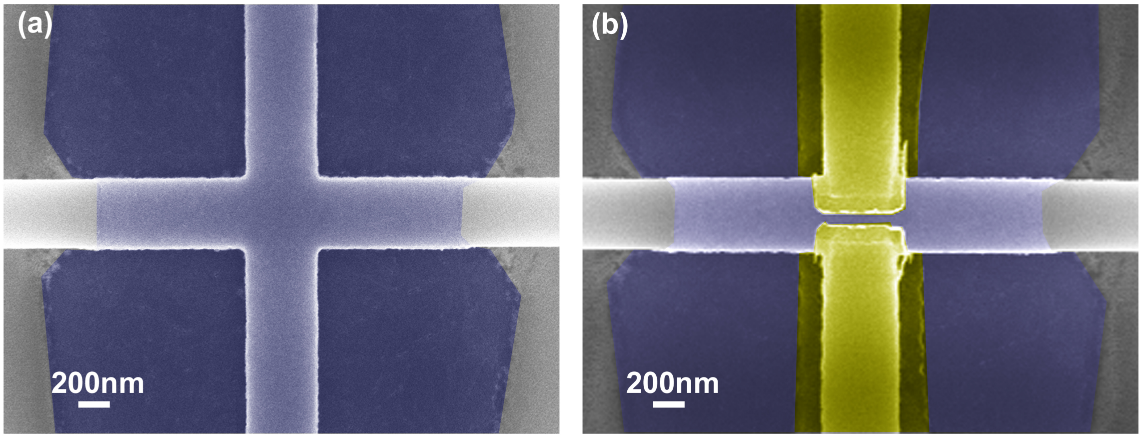

Figure 3.5: SEM images of the results of last 2 layers of lithography for the Si-VO_2 electro-optic modulator (a) after VO_2 patch deposition and (b) after gold contact deposition. False color: purple VO_2 and yellow gold.

3.2.3 Fabrication: Deposition

In order to complete second and third layers of lithography, fabrication facilities at VINSE were used with following process parameters. First, PMMA A4 950k photoresist was spun at 2000 rpm for 45 sec and baked at 180°C for 1.5 min to produce a 300 nm resist layer. It was then exposed at 800 μC/cm^2, 20 kV, 30 μm aperture, and 10nm step size and developed in a MIBK/IPA (1:3 v/v) mixture for 45 sec. VO_2 deposition was then performed using one of the following methods: pulsed laser deposition (PLD), electron beam evaporation (EBE), or sputtering. The three deposition methods were performed by Haglund group members at Vanderbilt. The results obtained from these methods varied significantly based on the condition of the deposition tools. At first the best film uniformity and stoichiometry were achieved with the PLD method, then after several months by EBE, and then eventually sputtering yielded the best results. Regardless of the deposition method, however, a post-development, pre-deposition dry oxygen-plasma clean was critical to producing quality VO_2.

In order for the pre-deposition clean to be effective, the chamber needs to be pre-seasoned, which is done by running the oxygen plasma clean for at least 10 min on the empty chamber. The reflected inductively coupled plasma (ICP) power should be less than 2 W. After pre-seasoning, the sample should be placed in the chamber and cleaned for 3 sec. Immediately after the clean, the deposition should be performed. Amorphous VO_x (non-switching) is first deposited on the sample, followed by lift-off in acetone for 1 hour. The amorphous VO_x is then annealed at 450°C and 250 mTorr of oxygen for 10 min to produce stoichiometric switching VO_2 for all deposition methods.

The electrical performance of a given VO_2 film can often be predicted from SEM imaging of the film structure and uniformity. Fig. 3.6 depicts one case of good switching VO_2 (a) and three different cases of rough-looking non-switching VO_2 (b-d). The difference is quite obvious: the good films appear largely featureless with barely visible crystals and bad films appear very rough. This roughness can be caused by a number of factors. The most important factor is the cleanliness of the surface on which the VO_2 is deposited. Another

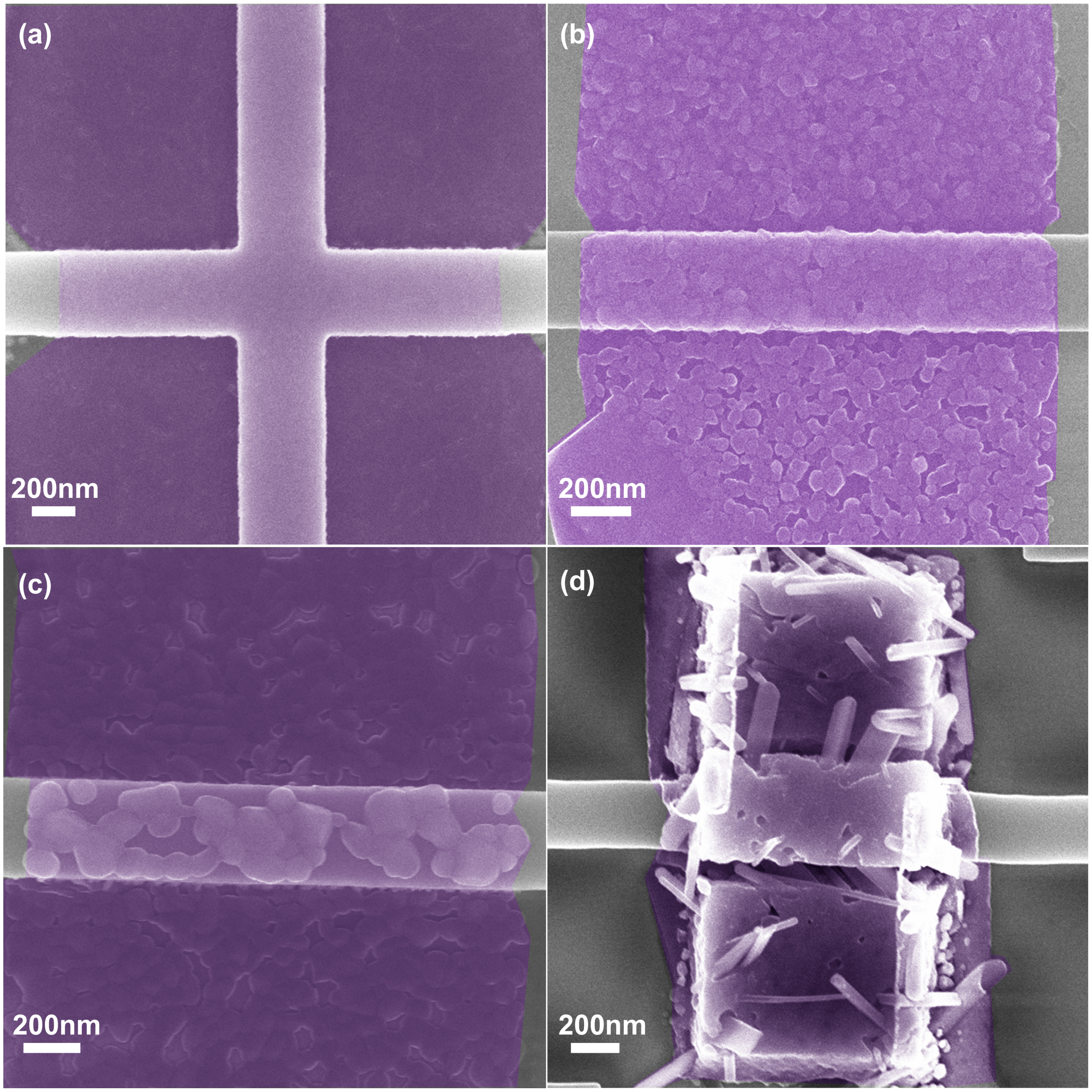

Figure 3.6: SEM images of VO_2 films with different morphology. ”Good switching” VO_2 tends to be smoother (a), while rougher films with various protrusions tend not to exhibit the expected switching behavior (b-d). VO_2 is highlighted in false color (purple) on various silicon structures (gray).

factor is over-annealing, the films become rougher when they are annealed for longer times. Another possible reason for surface roughness is under-exposure or under-development, which leads to resist being left on the surface.

Similarly to the VO_2 mask lithography, the mask for gold contacts is produced using a 300 μC/cm^2 dose, 20 kV accelerating voltage, 30 μm aperture, and 20 nm step size on the Raith EBL. The pre-deposition clean is similarly performed before the metal contacts are deposited. The contact films consists of two layers: a 15 nm adhesion/ohmic layer of titanium and a 65 nm gold layer. Alternatively, chromium was used as an adhesion layer, performing similarly to titanium.

3.3 Electrical Measurements of Electrical Switching of VO_2

3.3.1 Steady-State Electrical Switching

First the electrical properties of the devices are characterized by varying the applied voltage to obtain an I-V curve for each device. In order to make electrical contact to the device, two manipulator probes are placed in direct contact with the gold contact pads. The probes are connected to a Keithley 2400 source-meter, which both supplies a voltage and measures the resulting current though the device. The device SEM image is presented in Fig. 3.7(a) and I-V curves for different contact separation for the first generation geometry are presented in Fig. 3.7(b). At a certain threshold voltage, a high-conductivity current path is formed through the VO_2 patch [103, 104] and a significant jump in current is observed as shown in Fig. 3.7(b). The threshold voltage increases for increased contact separation, as expected, in order to maintain the necessary electric field intensity for switching VO_2

(~3.5-4.2 x 10^6V/m).

Despite consistent electrical switching results for some devices from the first generation design, most devices were not usable either initially or after a few switching cycles. If the current is not appropriately limited in the metallic state, the devices have a tendency to burn out. They are also prone to electro-static discharge damage, which is why a grounding strap should be used at all times when handling these devices. The failure mode usually includes a melting of either thin parts of the gold contacts that go up the waveguide wall or melting of the VO_2 film itself. Example SEM images of burned out devices are shown in Fig. 3.8.

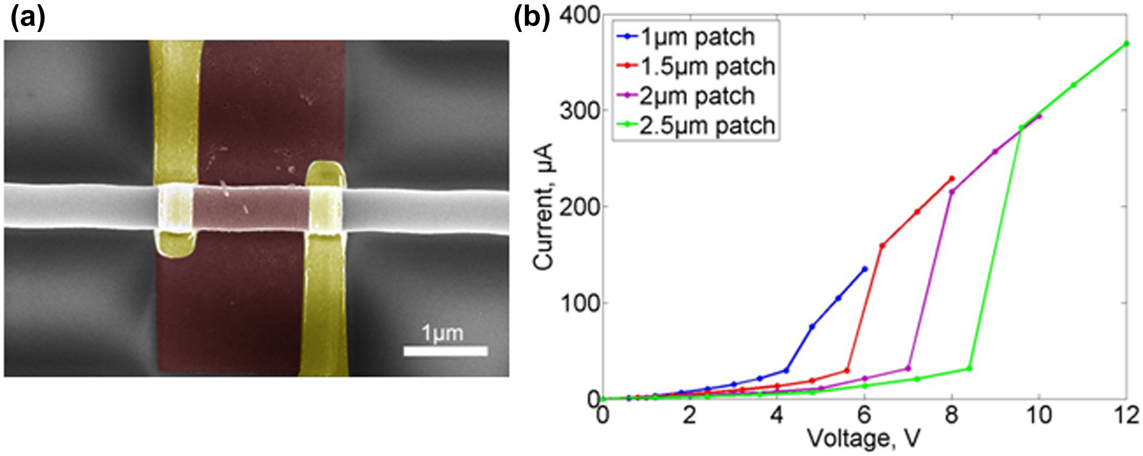

Figure 3.7: (a) SEM image of a first generation hybrid Si-VO_2 electro-optic modulator. (b) I-V curves for different patch size and contact spacings in first generation devices with contact spacing equal to patch length minus 600 nm.

3.3.2 Poole-Frenkel Model

In order to make the devices more robust and resistant to burning out, the second generation geometry was developed incorporating contact supports into the design (Fig. 3.4(b)). The IV behavior of second generation devices was very similar to the first generation and is shown in Fig. 3.9(a). The gap between contacts in this case was very small (100 nm) to

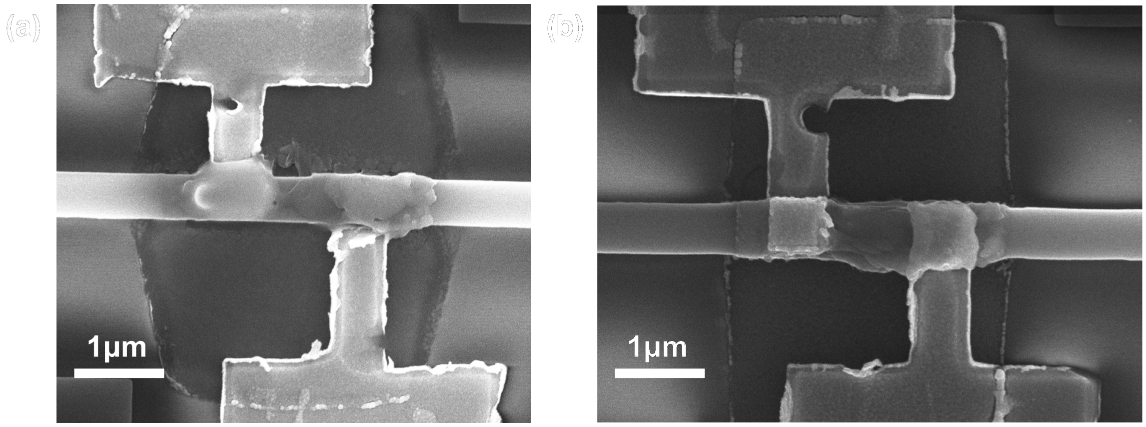

Figure 3.8: SEM images showing electrical damage typical in first generation devices.

induce the phase change at lower voltages. Prior to the current jump characteristic of the phase transition, a non-linear relationship between leakage current and applied field can be observed, as shown in Fig. 3.9(a). This behavior is typical for semiconductors prior to electrical breakdown and there are several mechanisms responsible for this behavior.

In most insulating materials the two breakdown modes are Zener [105] and ionic breakdown. Zener breakdown is non-destructive and involves quantum tunneling of carriers through a material's bandgap. Ionic breakdown is destructive and involves migration of ionized atoms in the lattice. In phase change materials like VO_2, two additional mechanisms are present: thermal breakdown where Joule heating triggers the phase transition and Mott-like breakdown where either injected carriers or formed electron-hole pairs exceed the critical carrier concentration and trigger the phase transition [106]. Poole-Frenkel emission has already been shown to be responsible for enhanced Joule heating at the initiation of the phase transition in VO_2 when triggered by THz electric fields [62], as well as in V_2O_3 [107]. The Poole-Frenkel effect lowers the thermal energy threshold for the valence electrons to be excited to the conduction band in the presence of a large electric field and can be identified by a following relationship:

$$I \propto E e^{\frac{-q(\phi_B - \sqrt{qE/\pi\varepsilon}}{k_B T}} \tag{3.1}$$

where ε is permittivity, T is temperature, ϕ_B is the hopping-potential barrier, k$_B$ is Boltzmanns constant, and q is the elementary electronic charge. The exponential growth characteristic of this effect is evident in the I-V measurements of our devices (Fig. 3.9(a)) prior to the dramatic current increase indicating the formation of a metallic current path between gold contacts. The Poole-Frenkel model agrees well with the experimental I-V data for exact device parameters: ε = 10.56, T = 293 K, ϕ_B is 0.2 eV.

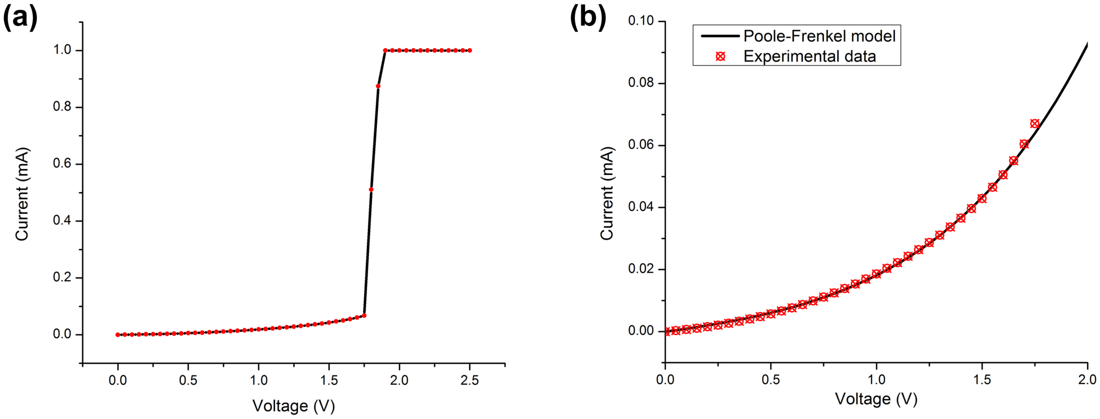

Figure 3.9: (a) I-V behavior of the second generation hybrid Si-VO$_2$ electro-optic modulator. (b) I-V relationship of the device before the phase transition: the smooth curve is the I-V curve calculated from a model that includes Poole-Frenkel emission.

3.3.3 Transient Electrical Switching

In order to measure the switching times of our device, a function generator producing square voltage pulses as short as 10 ns with varying amplitudes is employed to supply pulses to a simple circuit consisting of the device in series with a current limiting resistor (Fig. 3.10(a)). The voltage across this resistor is measured and the resistance of the Si-VO_2 device is calculated based on the amplitude of the input pulse using voltage division. As shown in Fig. 3.10(b), it is expected that the voltage across the resistor normalized to the total voltage increases when the device is switched to the metallic state. Although simple in concept, this measurement scheme is tricky to implement. The circuit itself can operate with any value of current limiting resistor as the capacitance of the VO_2 device is negligible. The cables and connections in the setup have to be rated for higher than 1 GHz frequencies if 1 ns resolution is desired. In our setup the hard limiting factor was the rise time of the function generator, which was 2 ns. A special sample holder (Fig. 3.12) with SMA connectors and silver signal strips was obtained from the Radiation Effects group at Vanderbilt and was rated for 4-5 GHz. The holder was tested using a network analyzer to demonstrate the correct bandwidth. Then the sample was placed on the holder using carbon tape and wirebonded using a Westbond wedge wirebonder.

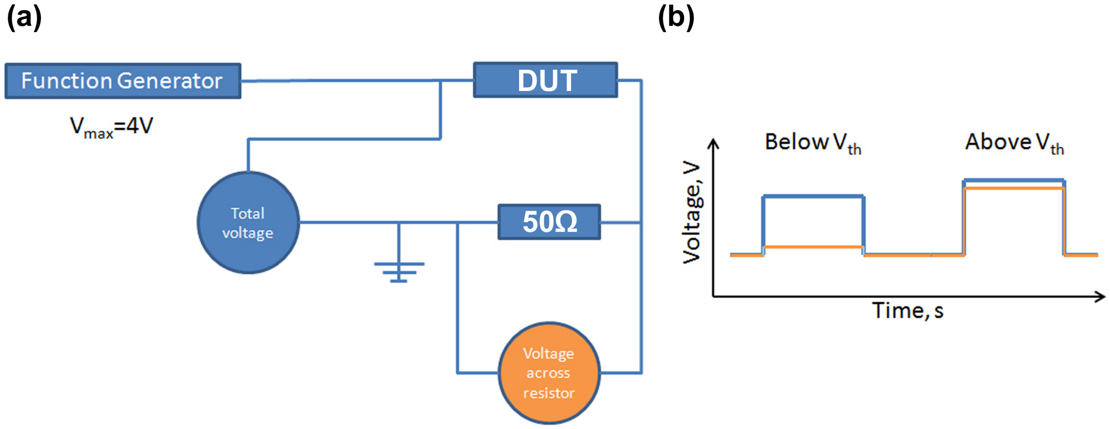

Figure 3.10: (a) Schematic of the electrical transient response testing setup of the device under test (DUT) and (b) expected behavior of the devices below and above the critical voltage.

In this type of electrical measurement, considerable attention should be given to the measurement instrument. A typical oscilloscope has an internal capacitance of 20pF and an internal resistance of 1 MΩ, limiting its bandwidth to 50kHz if the stored charge during the measurement has to be discharged through the oscilloscope. In case where the current limiting resistor in our circuit is smaller than 1 MΩ, the bandwidth is roughly equal to 1/RC, where C = 20 pF. Therefore, if 1 GHz bandwidth is desired, the maximum resistance of the current limiting resistor is 50 Ω, which means that the current through our device cannot be very effectively limited.

Since the current limiting resistor is fixed at a small value, measuring the devices electrically has a high chance of burning them out, therefore device geometry for this measurement was simplified. The optical component was eliminated and a VO_2 film was deposited on a flat undoped silicon substrate with gold contacts deposited on top of VO_2. This geometry improved the heat dissipation and prevented the devices from burning out immediately. Fig 3.11 shows 10 ns pulse measurements, below and above threshold voltage. The resistance decreases by approximately an order of magnitude (from 5 kΩ to 500 Ω) when a voltage above threshold is applied, indicating that a current path has been formed through the VO_2 patch. This graph also indicates that the phase transition occurs faster than the resolution of our measurement limited by the rise time of the function generator, which is less than 2 ns. This switching time is the fastest among those reported for VO_2 [56, 91, 108, 109] in the case of DC field application. These measurements indicate that a high-conductivity path has formed between the gold contacts.

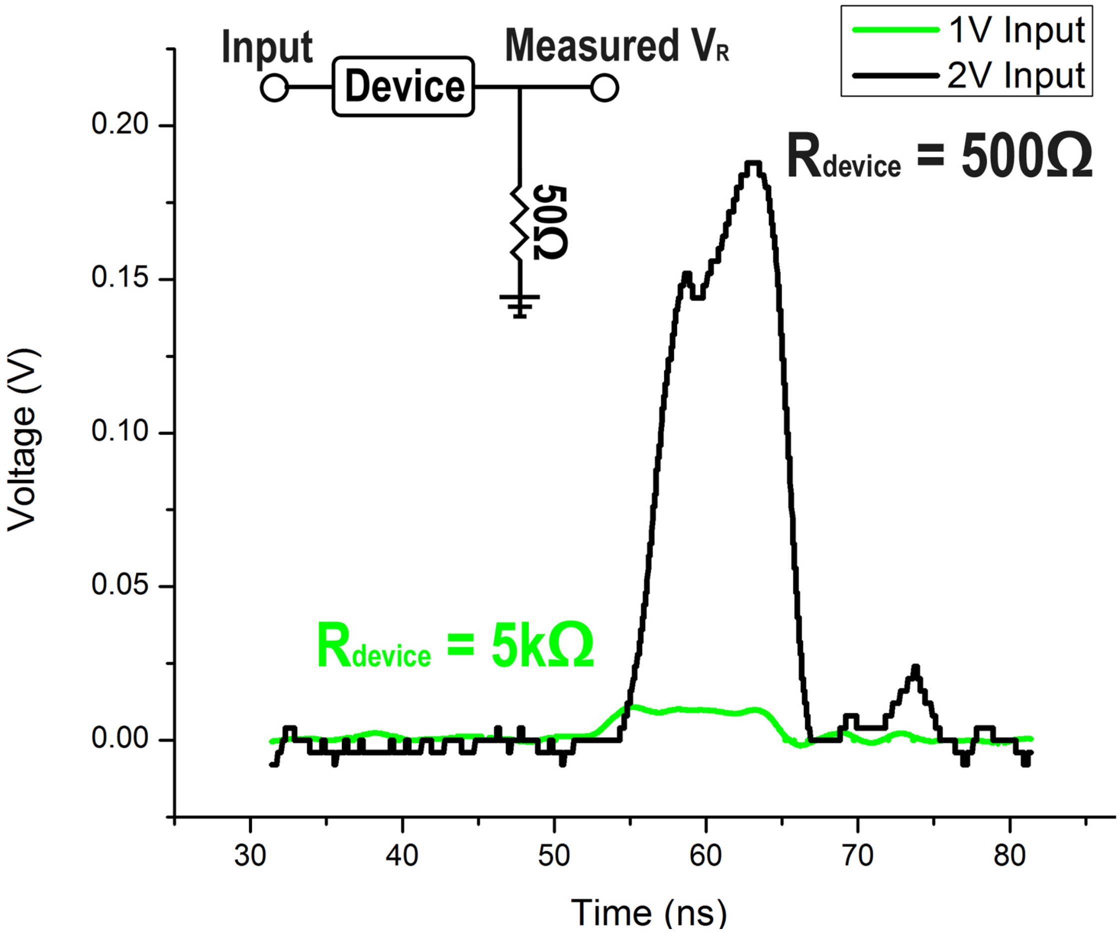

Figure 3.11: Response to a 10 ns voltage pulse below (green) and above (black) the VO_2 switching threshold voltage.

3.4 Optical Monitoring of Electrical Switching

3.4.1 Measurement Setup

In order to optically measure the phase transition, laser light is coupled into the waveguide via a tapered fiber. TO outline coupler was used at the input and output sides of the waveguide. The RF sample holder is connected to a function generator (Stanford Instruments 535G) and current limiting resistor and then mounted on the fiber coupling setup, as schematically shown in Fig. 3.12. The light source, a TE-polarized tunable laser (Santec TSL-510), is fixed at a set frequency and intensity, and therefore the changes in the output are only due to the changes in VO_2 absorption. At the output end of the waveguide, the light is collected by another tapered fiber and then detected by a Newport 2936-C photodetector. Changes in the signal as small as 0.1 dB can be distinguished from noise.

3.4.2 Steady-State Electro-Optic Response

In order to determine the dimensions and the phase of the VO_2 in the patch that participates in switching, optical transmission measurements through the underlying waveguide are conducted. The first method involved applying square voltage pulses of varying duration and magnitude to the electrical contacts while measuring the optical output of the waveguide. A typical result is presented in Fig. 3.13, where the value of the current limiting resistance is 5.1 kΩ and the applied voltage is 5 V for three one seconds pulses and one five second pulse at the end. The modulation depth is defined as $10log(\frac{P_{ON}}{P_{OFF}})$, where P_{ON} is the optical power in the ”ON” state (0 V) and P_{OFF} is optical power in the ”OFF” state (5 V). The second method consisted of ramping up the voltage from 0 V to 7 V in

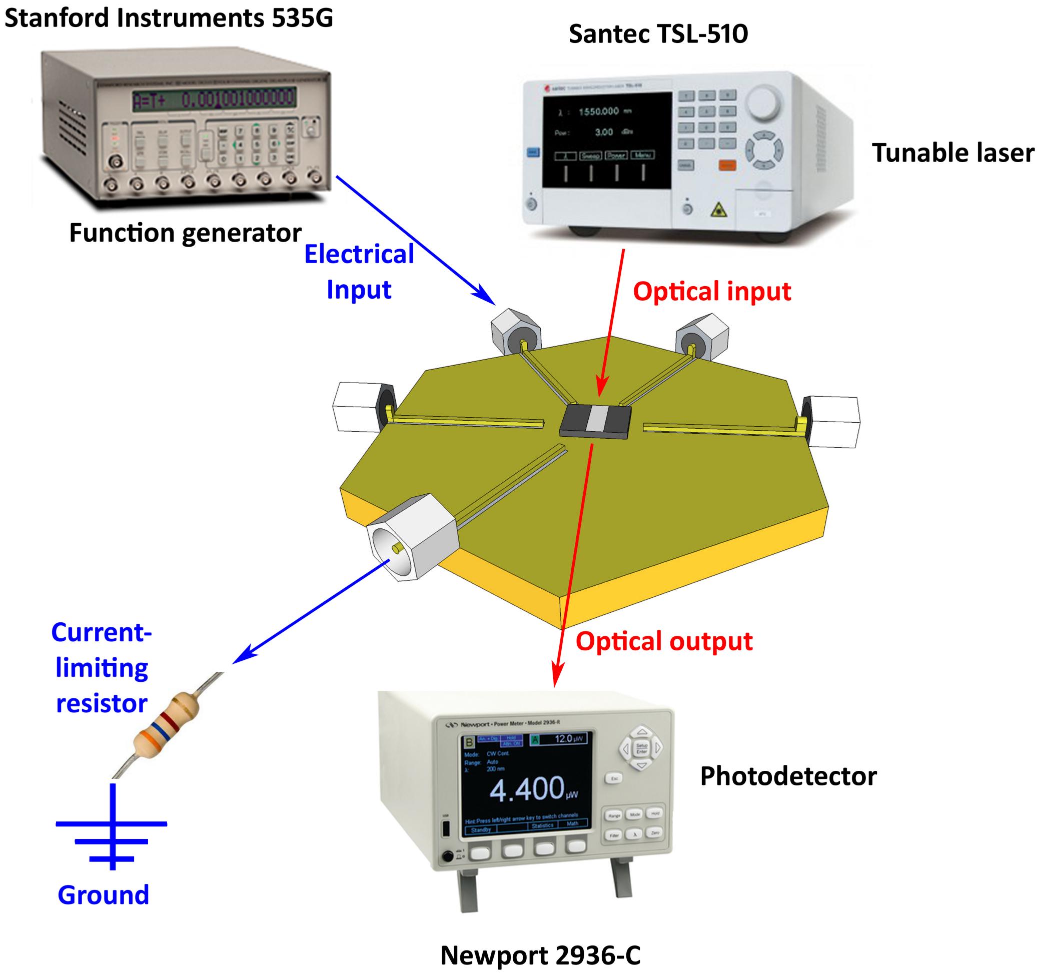

Figure 3.12: Schematic of the electro-optic test bed.

increments of 1 V and ramping it back down. The modulation depth obtained by the second method is plotted as a function of applied voltage in Fig. 3.14(a). First method yielded similar results.

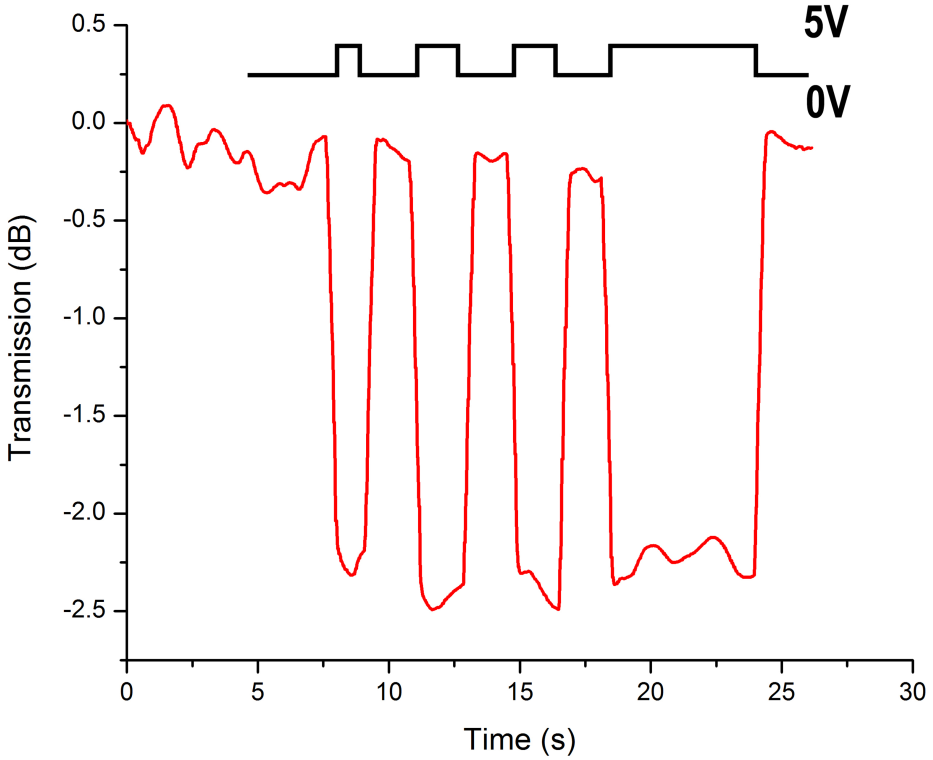

Figure 3.13: Optical transmission as a function of time when an electrical signal (shown in black) is applied to the contacts of the hybrid Si-VO_2 modulator.

Another method for changing modulation depth is varying the current limiting in-series resistor (Fig. 3.14(b)). At higher values of resistance, the modulation depth is very low, indicating that a very small portion of the VO_2 patch is switched to the metallic state and the remainder stays in the semiconducting state. Modulation depth in this optical system is directly dependent on the portion of the VO_2 patch that is switched to the metallic state and can support current flow, which is apparent in Fig. 3.14(c) where the modulation depth is directly proportional to the current resulting from the applied voltage. The relationship between current flowing between the contacts (obtained directly from Keithley 2400 sourcemeter) and modulation depth was found to be the same whether the series resistor was varied or the applied voltage was varied. FDTD simulations were then performed to estimate the volume of metallic VO_2 necessary to achieve different modulation depth of the hybrid Si-VO_2 electro-optic modulator. The FDTD results, along with suggested metallic VO_2 dimensions corresponding to each modulation depth value, are shown in Fig. 3.14(d).

3.4.3 Transient Electro-Optic Response

In order to capture the time varying behavior of the VO_2 phase transition, a faster photodetector needs to be utilized. The New Focus FPD510 used in this work has a bandwidth from DC to 200MHz and optical gain of 50,000 V/W. This optical detector is connected to a 2.5 GHz Agilent oscilloscope, which is synchronized with the function generator trigger signal. With this setup it is possible to measure transmission changes as small as 0.5 dB with a temporal resolution of 2-3 ns.

First, the pulse duration was varied from 100 ns to 900 ns with a constant pulse voltage of 4 V, and the time dependent optical transmission was measured, as shown in Fig. 3.15(a). A modulation depth of $\approx$5 dB is achieved within less than 100 ns and the recovery time is on order of 600 ns for all pulse durations. By comparing the experimentally measured modulation depth with the FDTD simulations shown in Fig. 3.14(a), the results suggest that nearly the entire 2.5 μm patch of VO_2 is switched to the metallic state. Dynamic, finite-

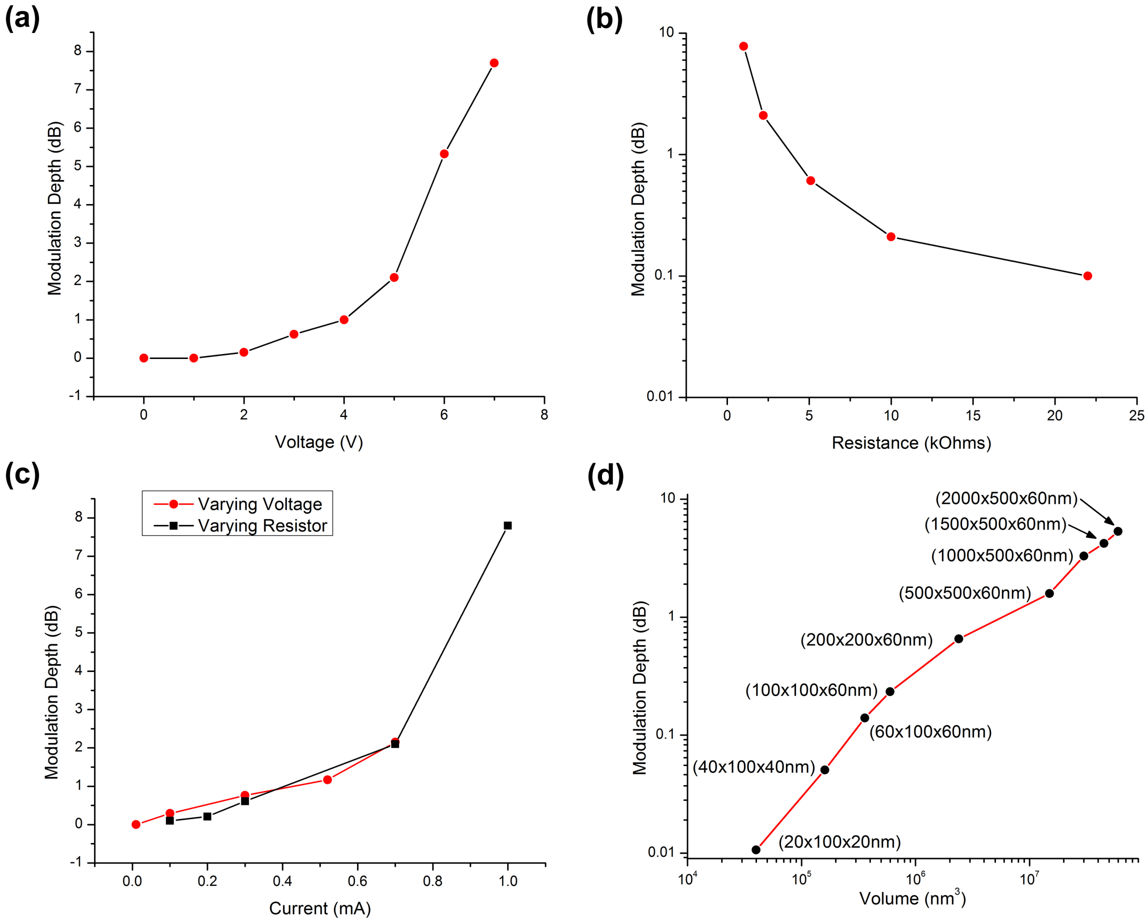

Figure 3.14: Optically measured change in modulation depth of Si-VO_2 electro-optic modulator of a second generation with a 100 nm gap between contacts as a function of (a) voltage applied to the contacts of the hybrid Si-VO_2 electro-optic modulator in the second generation design with contact spacing of 100 nm, (b) in-series resistance of the current limiting resistor (voltage = 4 V), and (c) current through the device. (d) FDTD simulation results providing the relationship between modulation depth and the volume of VO_2 needed to be switched to the metallic state to achieve that modulation depth.

element heating simulations (COMSOL) were then performed to study the global temperature change of the Si-VO_2 device as a function of time, assuming the entire VO_2 patch was switched to the metallic state when the voltage was applied. The simulated recovery time for the device to return to room temperature after the voltage was turned off matched well with the experimental value of 600 ns (Fig. 3.16(d)). The fact that the transmission started to decrease as soon as the voltage was turned on further suggests that the high-conductivity current path formed between the electrodes is indeed metallic VO_2. When a smaller voltage is applied, the modulation depth decreases, as shown in Fig. 3.15(b), which is consistent with the slower time response studies shown in Fig. 3.14(a). The slight difference in modulation depth between dynamic and steady-state measurements is due to normalization and different voltage sources. Applying shorter input voltage pulses also leads to reduced modulation depths as there is not enough time for the entire VO_2 patch to fully heat up and transition to the metallic state (Fig. 3.15(c)). In this case, the slow thermal recovery time can be eliminated (20 ns curve in Fig. 3.15(c)), as the heat is localized to a smaller volume and can be more readily dissipated. In all experiments, the initial transmission change is nearly instantaneous with the applied voltage, regardless of the magnitude and duration of the input voltage pulse. The fastest modulation speed measurable in our setup is shown in Fig. 3.15(d). A 3 V, 10 ns applied voltage pulse leads to a $\approx$0.7 dB change in transmission intensity, suggesting that a 200 x200 x 60 nm portion of the VO_2 patch between the contacts is switched to the metallic state (i.e., through comparison to the FDTD simulations shown in Fig. 3.15(d)). If we assume only a single grain of VO_2 is switched between the electrodes ($\approx$60 nm x 100 x 60 nm), then only a $\approx$0.1 dB modulation depth would result, which is the measured modulation depth of Si-VO_2 modulator with a large in-series resistance (Fig. 3.14(b)). Thus, it is likely that some heating of the VO_2 patch still occurs on the 10 ns timescale, which increases the volume of metallic VO_2 beyond the region of a single grain between the electrical contacts. The in-series resistance can be carefully selected to prevent this additional heating, while still allowing for the phase transition to be completed within the single grain of the VO_2 film. In this case, the cooling dynamics can be assumed to be similar to the heating dynamics, and the recovery time will be faster than 2 ns, which was the electrical response time measured in Fig. 3.11.

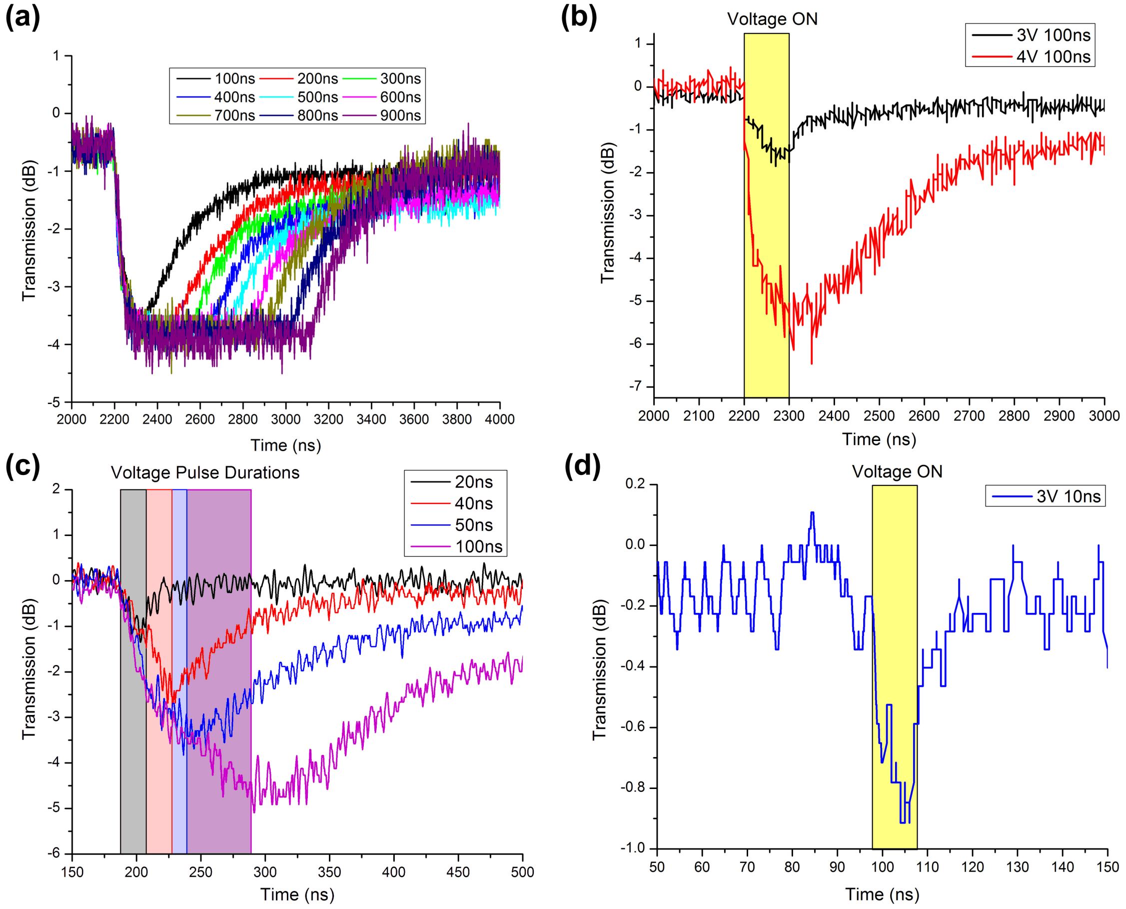

Figure 3.15: Optical transmission measurements of $Si\text{-}VO_2$ electro-optic modulator as (a) 4 V voltage pulses of varying duration (100-900 ns) are applied to the contacts, (b) 100 ns voltage pulses of varying voltage (3 or 4 V) are applied to the contacts, (c) 4 V voltage pulses of shorter durations (20-100 ns) are applied to the contacts, and (d) a 3 V, 10 ns voltage pulse is applied to the contacts.

When triggered by an electrical signal, the VO_2 phase transition has two distinct time scales: (1) ultra-fast Poole-Frenkel assisted localized heating that occurs on picosecond time scales on the portion of the VO_2 patch between contacts and (2) slower, purely thermal heating of the rest of the film. The faster thermal process is much more challenging to model because the carrier concentration dynamics, which are not straightforward to ascertain, play a central role. The thermal process is more predictable and therefore easier to model. Through dynamic electro-optic switching experiments in conjunction with electrical and thermal modeling, we can track the metalization of VO_2 across the full patch. For example Fig. 3.16(a) shows the optical transmission of the Si-VO_2 electro-optic modulator for two input voltage: 3 V and 4 V. It is apparent from COMSOL heat transfer simulations that in the case of the higher applied voltage, the VO_2 patch heats up more than in the case of the lower voltage because VO_2 remains in the metallic state longer as evidenced by the time delay between when the voltage is turned off and when the transmitted power begins to increase (i.e., as shown by the circled area in Fig. 3.16(a)). The simulations were performed using a standard heat transfer Joule heating package with applied voltage being the main input and initial temperature of 293 K. Fig. 3.16(b) shows the heat distribution for the 3 V case indicating that the whole patch is heated beyond the transition temperature (≈ 340 K). When the voltage is turned off the temperature immediately drops below critical (Fig. 3.16(c,d)), and then lingers around 320 K. This is why the optical transmission starts to increase as the degree of metalization of VO_2 decreases immediately. In case of 4 V input the peak temperature is much higher than 380 K and therefore the metalization of VO_2 does not decrease immediately, but only after the whole devices cools down below 340 K. Even though there is a general direct relationship between device temperature and

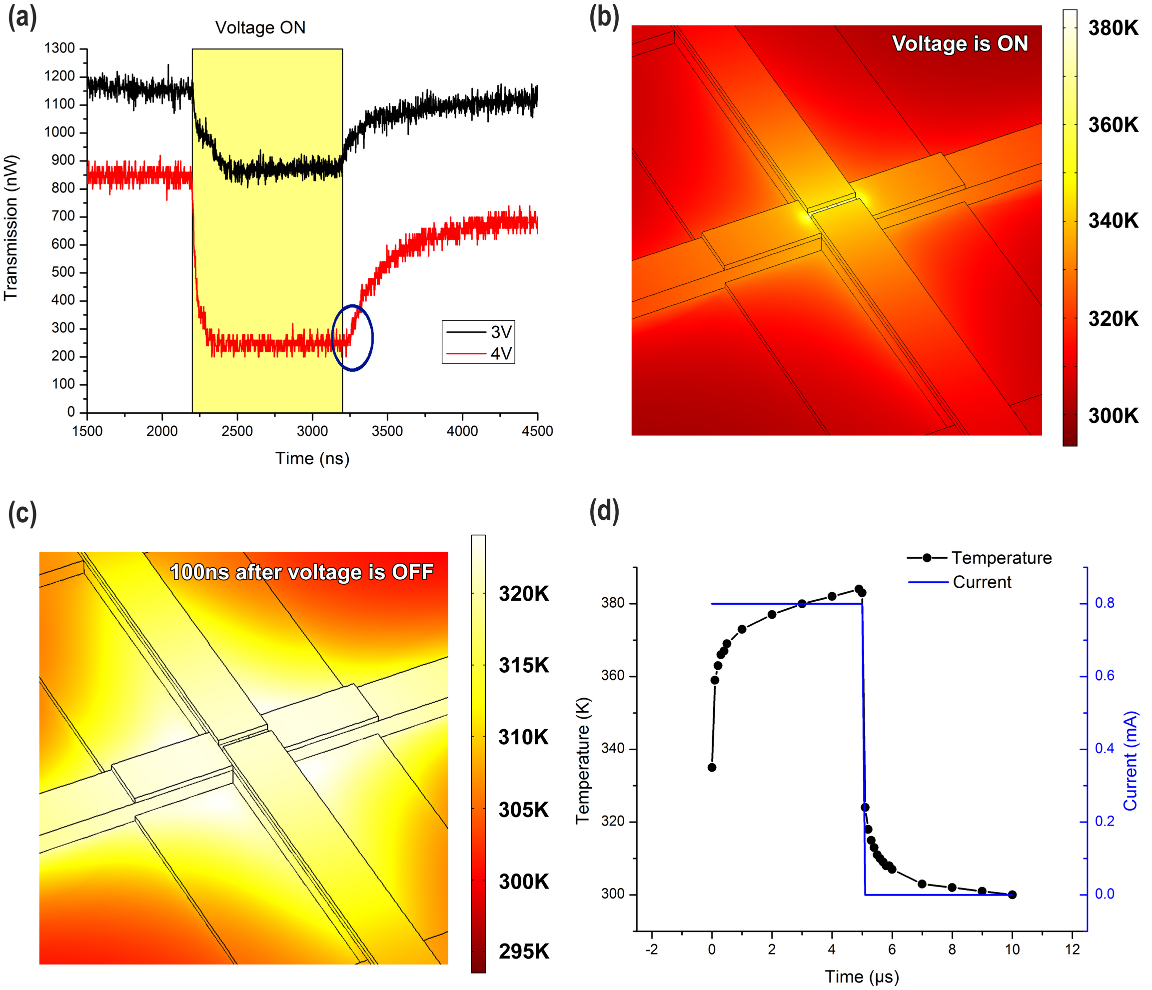

Figure 3.16: (a) Optical transmission measurement of Si-VO_2 electro-optic modulator in second generation geometry with 100 nm contact spacing as a 1 μs voltage pulse of either 3 or 4 V is applied to the contacts. (b) COMSOL heat transfer simulation showing global temperature of Si-VO_2 electro-optic modulator 5 μs after the 3 V input voltage is turned on (steady-state). (c) COMSOL heat transfer simulation 100 ns after the 3 V input voltage is turned off. (d) Maximum device temperature obtained from the time dependent COMSOL heat transfer simulation and device current input to the simulation as a function of time.

VO_2 degree of metalization, there are certain complexities due to VO_2 hysteresis behavior. When the temperature stays around 320-340 K the probability of VO_2 switching to the metallic state is much lower than for lower temperatures and therefore the long tail can be seen in most electro-optic switching measurements even thought the temperature has long dropped below critical.

3.5 Summary and Outlook

In this work we simulate and experimentally confirm the thermal processes taking place during electrically induced SMT in VO_2 by tracking the phase transition in space and time. Neither the electrical nor optical data have suggested that VO_2 phase transition can be initiated by an electric field alone; completion of the phase transition is always preceded by an increase in temperature mediated by an electric-field driven Poole-Frenkel emission. In this work we experimentally demonstrated transition times of $<$2 ns for semiconductor-metal transition. One question that remains is whether VO_2 transition back to semiconducting state as soon as it cools down, or the metallic phase persists at room temperatures. We conclude based on experiments that the reverse metal-to-semiconductor transition time cannot exceed 3 ns, and the temperature can return back to room in $<$1 ns based on simulation. Further investigation with a faster measurement setup will be required to determine the intrinsic VO_2 metal-to-semiconductor transition times. This transition time has been notoriously uncertain in previous work ranging anywhere from picoseconds to hundreds of nanoseconds depending on the switching method [51, 54, 56, 57, 63, 91, 107, 109, 110], but here we demonstrate that it cannot exceed 3 ns.

Investigating the phase transition dynamics is extremely important for the expanding field of VO_2 modulators. In this work some significant discoveries were made that can lead to better modulators. For one, the electric field plays an important part in triggering the phase transition in VO_2, but the main driving force is Joule heating. That however does not mean that GHz modulation is not possible, as the thermal processes are very fast (<10ps). The thermal component of the phase transition brings the need for better thermal design. The way I imagine future electro-optic modulators implemented is with driver electrical circuits that control the current dynamically and do not allow for significant heat spread.

Another consideration for future modulators is extinction ratio. Despite a very large change in refractive index across the phase transition of VO_2, the switching dynamics of VO_2 depend directly on the volume of the material that is switched. In order to achieve faster switching dynamics, the volume of VO_2 needs to be as small as possible. Therefore, in the linear absorption modulator geometry presented in this work, the desired extinction ratio (>3 dB) is challenging to achieve. More complex photonic structures can to be introduced to overcome this challenge. For instance, ring resonators can convert small changes in effective index resulting from a phase change in a small volume of VO_2 on the ring to large modulations of the optical signal, as shown in ref. [51]. In the next section, a different approach to address this issue is presented which takes advantage of sub-wavelength light confinement by plasmonics.

CHAPTER 4

DESIGN OF HYBRID AU-VO$_2$-SI ELECTRO-PLASMONIC MODULATORS BASED ON NEAR-FIELD COUPLING

4.1 Plasmonics for Modulators

In order to address the extinction ratio issue introduced in the previous chapter, we propose a hybrid plasmonic modulator design. Plasmonics offers a path to compact, low power modulators through subwavelength light confinement and a larger group index of plasmon modes compared to optical modes in silicon waveguides [53, 71]. However, as stand-alone elements, plasmonic modulators suffer from unfavorable trade-offs between footprint, losses, and extinction ratios. In order to accumulate necessary phase change for a high extinction ratio, a plasmonic modulator needs to have sufficient length, but the longer the modulator is, the higher insertion loss is. Insertion loss is defined as optical power lost in the ON state. Because of this trade-off between extinction ratio and insertion loss, there is significant interest in hybrid plasmonic-photonic structures [111, 112]. Hybrid plasmonic waveguides comprising a higher refractive-index dielectric, lower refractive-index dielectric, and a metal support much longer propagation lengths and lower losses than conventional plasmonic waveguides consisting of one dielectric and one metal component [72, 113].

In this case it is important to differentiate between hybrid plasmonic mode and hybrid Si-VO$_2$ structure. Hybrid plasmonic mode is defined above and does not necessary have to use VO_2 as a part of its structure. Hybrid material Si-VO_2 structure does not have to use plasmonics and was studied in detail in Chapter 3. Combining the two approaches makes a hybrid plasmonic mode hybrid Si-VO_2-Au electro-optic modulator in this case referred to by ”hybrid Au-VO_2-Si electro-plasmonic modulator” [114]. Purely plasmonic hybrid Si-VO_2 planar optical switches utilizing surface plasmons propagating between silver and VO_2 have been demonstrated, but the switching was slow ($\sim 25\,\mu$s) because the phase transition was initiated by heating [15, 52] and insertion loss high. In order to make improvements on this design, we utilize a hybrid plasmonic mode and electrical switching instead.

In order to realize an ultra-compact hybrid plasmonic modulator capable of operating at ultrafast speeds, we propose and computationally model a device geometry that incorporates electrical switching of VO_2 beneath a gold plasmonic nanodisk chain. Higher modulation speeds can be realized in this configuration because the slow thermal component of the VO_2 phase transition is minimized by switching the VO_2 electrically and integrating the plasmonic modulators into a photonic waveguiding system that couples efficiently into other silicon photonic components. There is a precedent for integrating hybrid plasmonic components with photonic waveguides: an efficient photonic-hybrid plasmonic mode coupler has been proposed and demonstrated for converting a standard silicon waveguide (quasi-TM mode) into a hybrid Au-Al_2O_3-Si plasmonic mode with 75 % power conversion [73]. Our design, which utilizes a photonic-hybrid plasmonic mode coupler, focuses on the active hybrid plasmonic modulator component and capitalizes on the enormous change in the VO_2 refractive index across the semiconductor-to-metal transition to achieve record values of extinction ratio per unit length.

4.2 Design of a Hybrid Au-VO_2-Si Plasmonic Modulator

Fig. 4.1(a) shows the design of the hybrid Si-VO_2-Au plasmonic modulator with silicon as a bottom layer, VO_2 as the active middle layer, and gold nanodisks on top. The gold nanodisk chain is chosen because of its compact footprint and regions of very high electric field confinement where the active material, VO_2, can be switched by an applied field. Fig. 4.1(b) shows the electric field distribution of the fundamental quasi-TM plasmonic mode for this structure, confirming that the mode is largely confined within the VO_2 layer, thus maximizing the extinction ratio of the modulator and allowing lower-loss propagation of the hybrid plasmonic mode in the semiconducting VO_2 film. When VO_2 is switched into a metallic state [Fig. 4.1(c)], the hybrid mode no longer propagates because the loss increases significantly, resulting in signal modulation. The proposed operation of the hybrid Si-VO_2-Au plasmonic modulator is as follows: (1) light is coupled from a standard silicon optical waveguide to the hybrid plasmonic modulator shown in Fig. 4.1(a) using the design strategy reported in Song et al. [73]; (2) a voltage is applied to the outmost gold nanodisks which switches the VO_2 from the semiconducting to the metallic state in the gaps between the coupled nanodisks; (3) when VO_2 is in the metallic state, the hybrid mode no longer propagates along the nanodisks and therefore does not couple back to a photonic mode. Consequently, modulating the electric field applied to the nanodisks effectively modulates the intensity of the output optical mode.

In designing an active plasmonic modulator with VO_2, three design goals are considered: (1) minimizing insertion loss, (2) maximizing modulation depth, and (3) minimizing active VO_2 volume in order to reduce the operating power. Since the modulator is intended

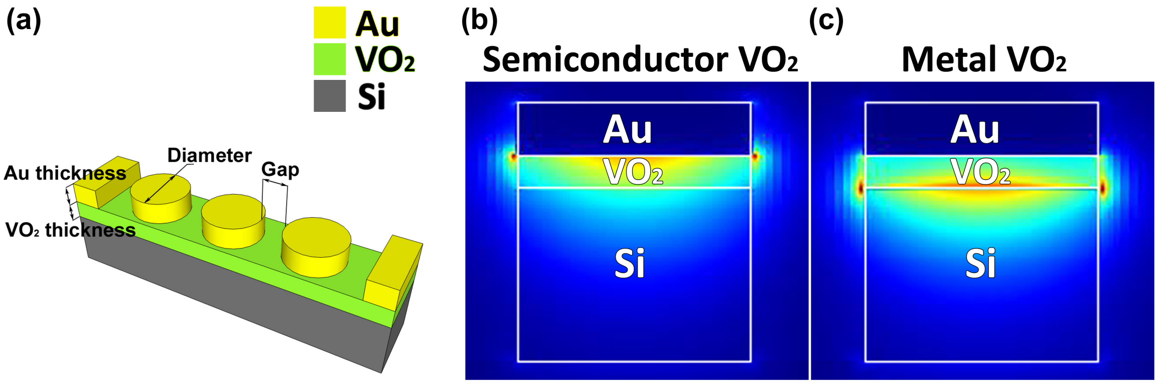

Figure 4.1: (a) Schematic representation of the proposed hybrid plasmonic modulator design based on Au, VO_2, and Si. Light is coupled into the modulator from a standard silicon waveguide using a photonic-hybrid plasmonic mode coupler (not shown). Electric field intensity of the hybrid mode for VO_2 in the (b) semiconducting state and (c) metallic state.

for use in the telecommunication band, we seek designs that maximize transmission near 1550 nm.

A hybrid Si-VO_2-Au waveguide without the Au nanodisks can be used as a modulator with a good extinction ratio ($\sim 15\,\mathrm{dB}/\mu\mathrm{m}$) and low insertion loss; modes of this structure are shown in Fig. 4.1(b,c). However, it is difficult to switch the VO_2 layer in this configuration using an electrical signal unless the gold layer is also used as an integrated heater [15], which would lead to the slow operational speed attendant to heating a large volume of VO_2. Hence we replace the continuous metal film by a chain of plasmonic nanodisks [Fig. 4.1(a)] in which the outmost nanodisks serve as electrical contacts for inducing the electrical semiconductor-metal transition (E-SMT) in VO_2 located in the gaps between nanodisks [52, 55–57, 115]. The E-SMT in VO_2 has recently been shown to occur at least as fast as 2 ns and potentially much faster [56, 107]. The size and spacing of the gold nanodisks not only controls the field strength in the VO_2 regions between nanodisks, but also allows control over the optical resonance wavelength.

4.2.1 Single Nanodisk Analysis

In order to minimize the insertion loss and gain insight into the behavior of the transmission spectrum of the gold nanodisks, the disk size and VO_2 film thickness were optimized in simulations using three-dimensional (3D) full field finite-difference time-domain (FDTD) simulations for a broad frequency range (1300-1700 nm), fixing both the silicon thickness and width at 200 nm, dimensions for which the photonic-plasmonic coupler was optimized in [73]. VO_2 was modeled using the measured real and imaginary parts of the refractive index as a function of wavelength [7]; silicon and gold were modeled using experimental data from [29].

In the optimization process, the transmission spectrum of a single nanodisk was first simulated by launching a hybrid plasmonic mode [Fig. 4.1(b)] into a continuous film Au-VO_2-Si waveguide, letting it propagate through the nanodisk and couple back to the continuous film Au-VO_2-Si waveguide [inset in Fig. 2(a)], and collecting it with a frequency-domain power monitor [114]. As shown in Fig. 4.2(a), the spectrum has a single broad resonance near 1600 nm; the lower wavelength side-lobe near 1400 nm is a simulation artifact due to degenerate modes reaching the power monitor through the silicon, and could be eliminated by increasing the source-to-monitor separation. Next, the VO_2 and gold thicknesses were varied within experimentally achievable limits, assuming that a lift-off fabrication method is used and that VO_2 is deposited as a continuous film (thickness 30-80 nm) [116]. The resulting transmission amplitude and peak resonance wavelength for the hybrid Si-VO_2-Au plasmonic modulator design with a single nanodisk were then analyzed. The continuous gold film thickness was always set to the same value as the nanodisk thickness in order to maximize mode match.

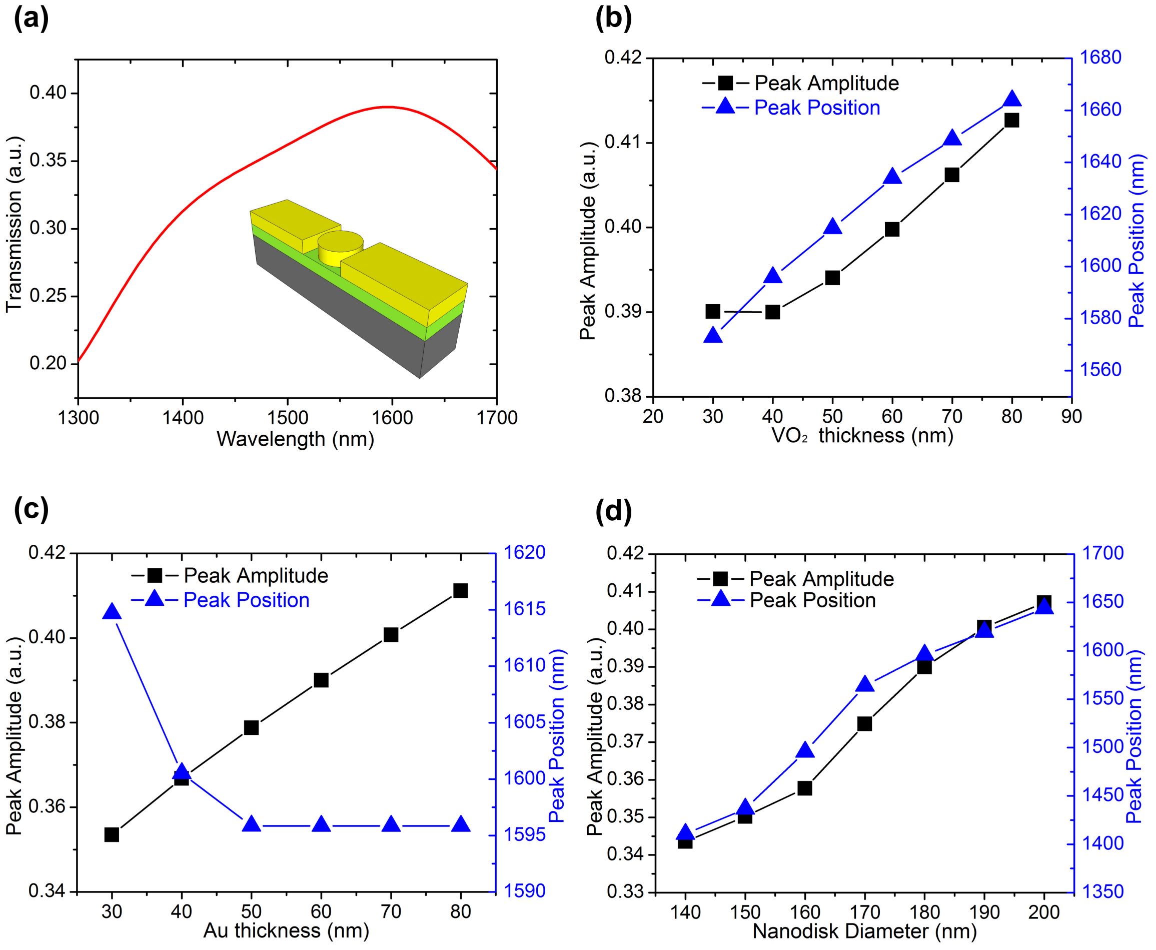

Figure 4.2: (a) Single gold nanodisk transmission spectrum (Nanodisk diameter fixed at 180 nm, Au thickness fixed at 60 nm, and VO_2 thickness fixed at 40 nm) . Inset shows the schematic: yellow is gold, green is semiconducting VO_2, and gray is silicon. The peak position and amplitude of the resonance for varying (b) VO_2 thickness (Au thickness fixed at 60 nm), (c) Au thickness (VO_2 thickness fixed at 40 nm), and (d) nanodisk diameter (Au thickness fixed at 60 nm and VO_2 thickness fixed at 40 nm) are shown.

Increasing the thickness of either VO_2 (for gold thickness fixed at 60 nm) or gold (for VO_2 thickness fixed at 40 nm) increases the resonance amplitude, as shown in Fig. 4.2(b) and 4.2(c), respectively. Increasing VO_2 film thickness improves coupling to the hybrid mode, leading to increased transmission amplitude. The increased transmission amplitude with increased gold thickness is associated with improved coupling between the gold film that forms part of the hybrid plasmonic-photonic coupler, and the gold nanodisk.

Two distinct mechanisms for increasing peak transmission amplitude are apparent in the behavior of the resonant peak wavelength as a function of VO_2 and gold nanodisk thickness. Increasing the VO_2 thickness linearly red-shifts the peak transmission wavelength as a larger portion of the mode becomes concentrated within the semiconducting VO_2 layer with its higher refractive index. Increasing the gold thickness initially blue-shifts the peak transmission wavelength as more of the mode extends into the low refractive-index gold nanodisk; however, beyond a critical thickness near 50 nm, further increases do not affect the peak wavelength because the field decays before reaching the added gold. Next, the effect of the gold nanodisk diameter was examined with the VO_2 and gold thicknesses fixed at 40 nm and 60 nm, respectively. When the diameter of the nanodisk is increased, the transmission resonance is red-shifted, as the resonance energy is reduced consistent with larger cavity size, analogous to quantum-confinement rules in quantum dots [Fig. 4.2(d)] [117]. The change in resonant wavelength is accompanied by an increase in transmission that is most likely caused by a smaller lateral mode mismatch between the 200 nm-wide continuous gold film and the gold nanodisk.

4.2.2 Nanodisk Chain Analysis

With the single nanodisk trends understood, we move on to investigate the effects of incorporating multiple nanodisks into the chain and varying the spacing between nanodisks. For this investigation, we select the nanodisk diameter of 160 nm, VO_2 film thickness of 40 nm, and gold film thickness of 60 nm to maximize the transmission amplitude while maintaining a transmission bandwidth encompassing standard communication wavelength bands. While these parameters for a single nanodisk design produced a resonance peak near 1450 nm, when multiple nanodisks are present, the peak wavelength red-shifts [Fig. 4.3(a)], which is typical for a coupled resonator system. As expected due to VO_2 absorption, the maximum transmission decreases for longer nanodisk chains. Also with additional nanodisks, the resonance peak becomes sharper due to the absence of degenerate modes discussed earlier. In order to choose the most desirable number of nanodisks, one needs to consider the benefits of longer nanodisk chains in comparison to the drawbacks. The main advantage of longer chains is an enhanced extinction ratio resulting from a longer interaction length, and therefore stronger spatial light-matter interaction of the mode with the active modulator material, VO_2. The primary disadvantage of longer gold nanodisk chains is increased insertion loss due to absorption in VO_2 and gold. As shown in detail in the next section, the three-nanodisk chain provides the large extinction ratio that is most suitable for modulator applications and is therefore the design selected for performance benchmarking [114].

The spacing between nanodisks plays an important role in both the efficiency of light propagation through the hybrid modulator and the strength of light-matter interaction between the hybrid mode and VO_2. As predicted by a simple plasmonic model of two circular particles, the coupling strength between two nanodisks increases when they are brought closer together. Fig. 4.3(b) illustrates the relationship between coupling strength (determined by the maximum transmission amplitude) and inter-nanodisk spacing for the hybrid modulator design, and exemplifies this trend. Although better near-field coupling is achieved for a gap of 10 nm, a 20 nm gap relaxes the fabrication tolerance and would be achievable with standard electron-beam lithography [118]. The electric field of the propagating mode is shown in Fig. 4.3(c,d) for a three-nanodisk chain on resonance. The intensity of the field is highest in the space between the nanodisks, but a fraction of the field does extend into the underlying VO_2 layer. The bending tails of the mode between nanodisks arise from longitudinal propagation of the resonating mode. Ideally, VO_2 would be deposited in the gaps between nanodisks to achieve best device performance; the fabrication would be realizable but challenging.

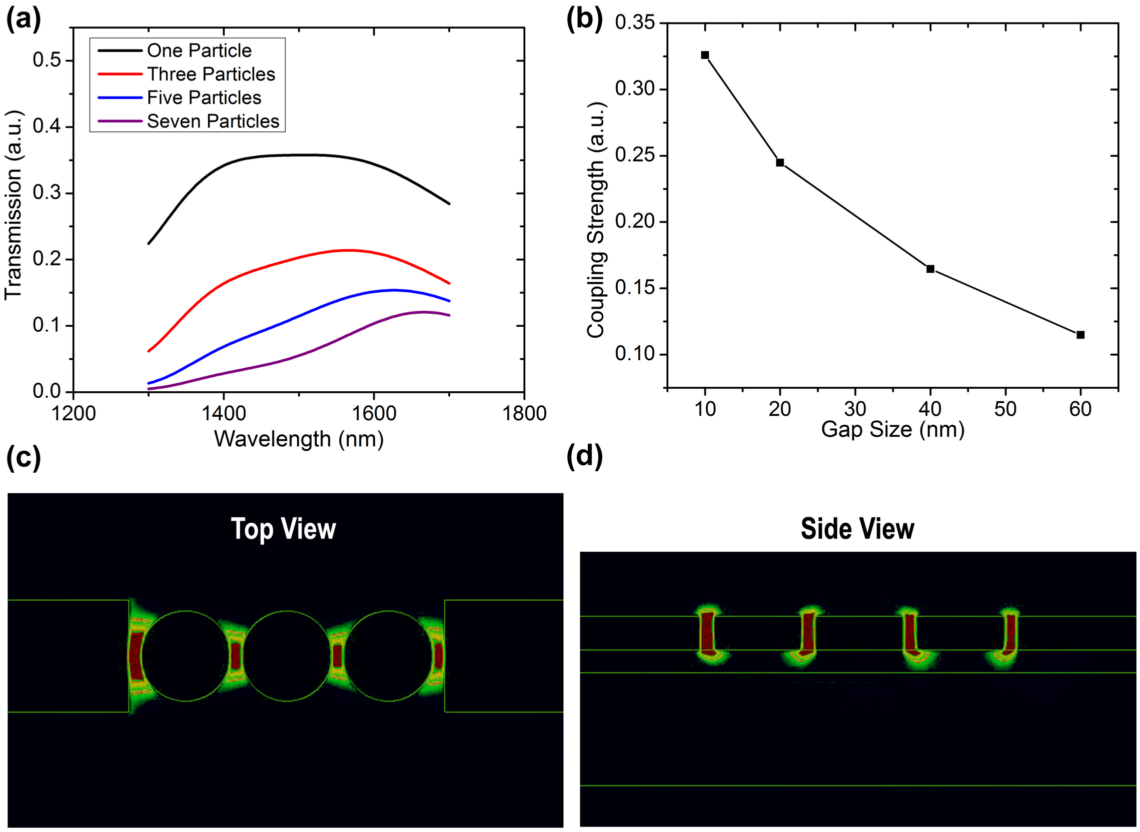

Figure 4.3: (a) Transmission spectra of the devices with varying number of nanodisks (16 nm nanodisk size, 40 nm VO_2, 60 nm gold). (b) Coupling strength dependence on the gap size between nanodisks (160 nm nanodisk size, 40 nm VO_2, 60 nm gold). Electric field distribution at resonant wavelength for three nanodisk chain shown in the (c) top view and (d) side view (160 nm nanodisk size, 40 nm VO_2, 60 nm gold, 20 nm gap). The field is strongest in the gaps between nanodisks and extends into the VO_2 region below the nanodisks.

Following the design studies, a three-nanodisk chain having a gold nanodisk diameter of 160 nm, a gold film and nanodisk thickness of 60 nm, and a VO_2 film thickness of 40 nm was selected to benchmark the modulator performance. This design minimizes overall footprint, minimizes active VO_2 volume, which in turn will minimize operating power, and minimizes insertion losses while providing a relatively large operating bandwidth. The extinction ratio of this modulator design is examined in the next section.

4.3 Performance of the Hybrid Au-VO_2-Si Plasmonic Modulator

With the hybrid Si-VO_2-Au modulator geometry selected, the performance metrics can be assessed. A major advantage of this modulator configuration is that the applied DC electric-field maxima coincide perfectly with the maxima of the propagating plasmon mode, indicating that the optical properties of VO_2 as it undergoes the phase transition will have maximal impact on the propagating mode. The hybrid plasmonic mode for the configuration shown in Fig. 4.3(c,d) is concentrated in an 80 nm x 80 nm area between three nanodisks, making the active VO_2 volume extremely small. Thus, linearly extrapolating from experimental data measured for larger patches of VO_2, the switching voltage in this configuration would be only 400 mV [119]. The data for larger patches is presented in Fig. 3.7(b). For electric field of 5×10^6 and 80 nm contact spacing, the switching voltage equals to 400 mV [114].

4.3.1 Thermal and Electrical Simulation

In order to confirm the required switching voltage, we carried out a finite-element analysis using the COMSOL heat transfer package. The simulation also includes the photonic-plasmonic couplers from [73] that serve as electrical contacts to the nanodisk chain. A voltage of 1 V was applied to the contacts, resulting in fields on the order of 10^7 V/m, above the measured threshold switching value for VO_2 ($\sim 5 \text{ x } 10^6$ V/m) [55–57, 119, 120]. The switching power in this configuration is calculated to be 4.8 mW (400 mV), almost an order of magnitude lower than the power consumed by a hybrid plasmonic-VO_2 device utilizing Joule heating (32.8 mW) [15]. In order to calculate the switching power, the switching voltage (400 mV) was multiplied by the current (12 mA) calculated by the COMSOL simulation if VO_2 is assumed to be semiconducting. The global temperature increase was calculated to be only 3°C above room temperature, suggesting that the electric field possibly augmented by local nanoscale heating are the primary switching mechanisms [Fig. 4.4(a)]. It is known that the electrical metal-insulator transition in VO_2 is triggered by two primary mechanisms, namely electrical tunneling and Joule heating. If Joule heating is minimized by limiting the current through the device, the primary mechanism will be electron tunneling. The size of the tunneling current path is largely unknown. Therefore, in order to estimate the extinction ratio, different sizes of metallic VO_2 filaments within a semiconducting matrix were simulated using 3D FDTD calculations.

4.3.2 Modulation Performance

A schematic of the simulation geometry is shown in Fig. 4.4(b) and results are shown in Fig. 4.4(c). The greatest improvement in extinction ratio is observed for the smallest width of metallic VO_2, while saturation in the extinction approaching 8 dB is observed for widths greater than approximately 100 nm. Gains in extinction ratio diminish when the metallic region of VO_2 extends beyond the width of the plasmonic field ($\sim$ 80 nm) between nan-

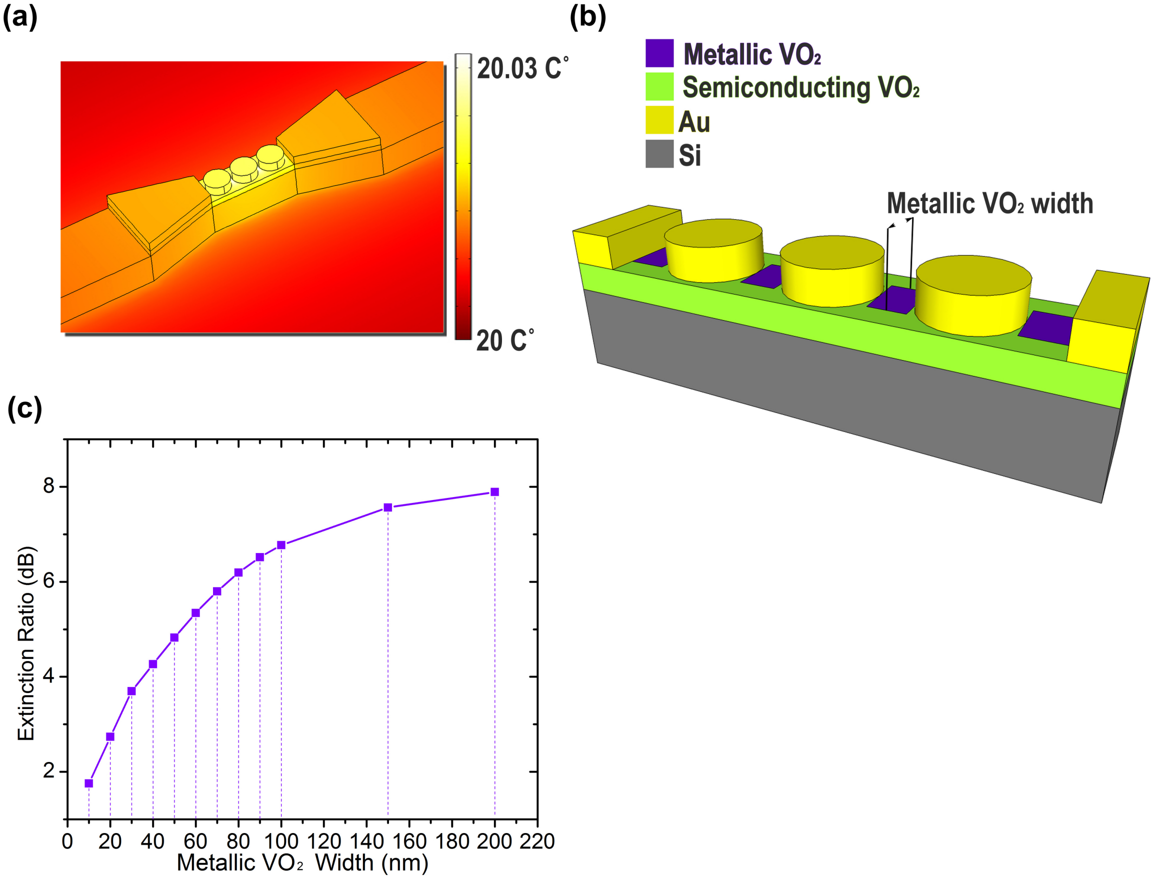

Figure 4.4: (a) Joule heating simulation of the hybrid modulator. (b) Schematic illustrating regions of VO_2 metallization when a voltage is applied across the gold nanodisk chain. (c) Extinction ratio of the hybrid Si-VO_2-Au optical modulator as a function of the metallic VO_2 region width.

odisks. If the tunneling path width is assumed to be 40-60 nm, the typical size of a single grain of multi-crystalline VO_2, the extinction ratio is of order 4-6 dB. This is an astonishingly large value considering that the hybrid modulator is only 560 nm long. Since this extinction ratio is sufficient for most modulator applications, there is no need to add additional nanodisks to the chain, which would further increase extinction ratio at the cost of increased insertion loss.

Our device is compared with other proposed and demonstrated silicon and silicon hybrid modulators in Table 4.1. The performance metrics highlighted in the table exhibit the advantages of the proposed design; the most significant improvements to the state-of-the-art are made in device footprint (560 nm x 200 nm), extinction ratio per unit length (~ 9 dB/μm) and switching power (4.8 mW).

A critical performance-limiting factor is the anticipated VO_2 switching time for the electrically actuated phase transition, which currently appears to limit the modulation speed to approximately 1 GHz according to published work related to electrical switching of VO_2 [56]. The phase transition into the rutile metallic state occurs in less than 100 fs using ultrafast optical excitation, with the reversion to the semiconducting state on the order of a few picoseconds for optical fluences below a critical fluence near 5 mJ/cm^2 [62, 63]. Whether terahertz electrical modulation of an optical signal is achievable in the hybrid Si-VO_2-Au geometry depends on the ultimate achievable speed of the VO_2 transition from the metallic to the semiconducting state. In this work we estimate the modulation speed of our device based on the current state-of-the-art electrical switching times for VO_2 (1 GHz) [56]. There are grounds for optimism with regard to the electrical switching speed of VO_2. The electronic transition of VO_2 has been found to occur prior to completion of the monoclinic-

Device Name	Modulation Mechanism	Length (μm)	Extinction Ratio (dB/μm)	Modulation Speed (GHz)	Voltage (V)	Power (mW)	Band-width (nm)
Plasmonic nanodisk chain Si-VO_2-Au (this work)	VO_2 phase transition	0.56	8.9	>1	0.4	4.8	~ 100
Hybrid SPP-VO_2 waveguide [15]	VO_2 phase transition	7	2.3	0.0004	0.4	32.8	>100
Si-VO_2 ring resonator [51]	VO_2 phase transition	3	4	0.04	-	-	1
Si-VO_2 absorption modulator [14]	VO_2 phase transition	2	3.25	$<10^{-10}$	-	-	>100
Field effect MIM SPP waveguide [53]	Si plasma dispersion	7.5	0.43	>1	0.8	-	>100
Silicon organic hybrid modulator [49]	Kerr nonlinearity in EO polymer	1700	-	42.7	4.1	-	>100
Si ring resonator modulator [45]	Si plasma dispersion	15	0.35	50	1	-	<1

Table 4.1: Comparison of plasmonic nanodisk chain hybrid Si-Au-VO_2 modulator with other plasmonic and photonic electro-optic modulators.

to-rutile transition for epitaxial films [109, 121]. Moreover, a metallic monoclinic (M2) state has been found to be accessible by both optical [59, 60] and thermal [61] excitation. It is therefore likely that more careful study will yield similar results for electrical excitation. In particular, evidence for possible increased speed of transition for smaller VO_2 patch size [58] is consistent with a conjectured two-stage quasi-electric-field excitation [99]. If it is possible to metallize the VO_2 without transforming the crystal structure, then electrical switching speeds substantially faster than 1 ns should be possible. Moreover, even without substantial discoveries in physics of VO_2 SMT, the switching speeds for small volumes mediated through field-enhanced Joule heating is predicted to occur on picosecond scales, which equates to hundreds of GHz modulation speeds.

4.4 Summary

We have developed a design methodology and simulated the performance of a hybrid Si-VO_2-Au modulator based on near-field plasmonic coupling between gold nanodisks. The hybrid modulator exhibited excellent performance in several important categories, including ultra-small footprint (560 nm x 200 nm), large extinction ratio per unit length ($\sim$ 9 dB/μm), and low operating power (4.8 mW). With the potential for direct integration into silicon waveguides, this new design is expected to dramatically improve the performance of silicon optical modulators without requiring a disruptive fabrication process. The fabrication of this design is discussed in Chapter 5 in the future work section (Sec. 5.2.1).

CHAPTER 5

CONCLUSION

5.1 Summary

In this work, two important components of future on-chip optical interconnects were investigated and improved. First, the challenge of bringing light from an off-chip laser on-chip was addressed by designing a passive coupler- component needed for efficiently coupling light from an off-chip fiber-coupled laser to an on-chip waveguide. Second, a hybrid material system (Si-VO_2) was investigated for its potential integration into on-chip optical interconnects. Finally, a hybrid active electro-optical modulator was designed and simulated using this novel material system. The results and improvements to state-of-art resulting from this research are outlined below.

In order to improve fiber-to-chip coupling for on-chip optical interconnects, mode and impedance matching issues were addressed by using transformation optics theory. Quasi-conformal mapping was selected for the transformation optics design approach to produce a fiber-to-chip coupler with an ultra-compact footprint, excellent efficiency and straightforward fabrication. In order to transform the coordinate system using quasi-conformal mapping, a numerical method from ref. [83] was solved in COMSOL Muptiphysics™. After producing a mapping that minimized permittivity anisotropy, the permittivity profile was impedance matched to the input fiber and output waveguide, and then simulated by the COMSOL electro-magnetic solver with a plane wave input source. The COM-

SOL solver produced a possible electro-magnetic field distribution through the coupler and showed no significant portion of the field escaping the coupler. Then, in order to realize the permittivity profile defined by transformation optics and quasi-conformal mapping, the Maxwell-Garnett effective medium approximation was employed with fixed diameter air cylinders embedded in the silicon matrix. These air holes were positioned in a hexagonal lattice and stretched out according to the permittivity profile. Hexagonal packing produces the largest range of permittivities and is superior to square or random packing. In order to correctly stretch the hexagonal lattice, a custom algorithm was developed and implemented in MATLAB. The algorithm uses Delaunay triangulation to determine the area around each air cylinder and then adjusts the lattice. The obtained air cylinder profile was similarly simulated in COMSOL for qualitative verification and then simulated using FDTD in Meep to quantitatively determine the coupling losses. The transformation optics (TO) coupler was then fabricated in SOI using standard electron-beam lithography at the Center for Nanophase Materials Sciences at Oak Ridge National Laboratory. Then the TO coupler was tested using a fiber-coupled test bed in conjunction with tunable lasers and the results were compared to simulation. Simulation and experiment matched reasonably well with some slight differences likely caused by fabrication errors, namely non-uniformity in the hole size and distortion in the hole shape. The fabricated TO coupler showed a peak 5-fold improvement over butt coupling in experiment and maximum transmission of 17 % in simulation. In comparison, the TO coupler outline without holes showed an average simulated transmission of 10 % and a 3-fold improvement over butt-coupling in measurement. We took measures to improve the bandwidth of the proposed coupler by implementing a ”restricted” transform coupler where the space was not fully transformed and that helped avoid having air holes too close together in the narrowest region of the coupler and prevented resonant oscillation. In conclusion, our TO design requires only a single layer of standard lithography and can be fabricated simultaneously with other on-chip components, such as modulators and waveguides, and shows a significant improvement in coupling efficiency compared to competing designs. Another approach was proposed and used for academic research applications that did not require the same high coupling efficiencies. The TO outline fabrication was significantly more straightforward and simpler than the TO coupler as it did not require fabrication of holes of accurate diameter and placement, yet it still improved efficiency compared to butt coupling. The TO outline coupler was used for all testing of our hybrid electro-optic modulators.

Next, a hybrid Si-VO_2 material system was investigated for its potential as an active medium for electro-optic modulators. Electro-optic modulators require an active media, which either changes its refractive index or absorption coefficient under electrical stimulus. Previously, VO_2 has been integrated in optical structures and its phase transition was triggered by optical signal or thermal heating. When the phase transition occurs, both refractive index and absorption coefficient are modulated significantly. The magnitude of this change is large enough to potentially shrink the electro-optic modulators by three orders of magnitude. The electrical switching of VO_2 has been previously investigated, but never using optical integrated devices. In this research, we combined electrical switching with optical monitoring of the phase transition with nanosecond temporal resolution. Through simulation and experiment, the phase transition was traced in space and time. In order to facilitate this experiment, a two terminal VO_2 electrical switching device was placed on top of a silicon waveguide. The waveguides were fabricated using standard electron beam lithography in SOI, and then patches of VO_2 were defined by aligned electron beam lithography and deposited by sputtering. A third layer of lithography was used to define the gold electrical contacts. Fabricated devices were tested electrically first under steady-state and then under transient conditions. The IV curves show a current jump at a critical voltage which is typical for VO_2 films. Then a current limiting resistor was connected in series with our device to minimize Joule heating resulting from current passing through the devices. A specialized radio-frequency stage was used for the measurements to minimize losses. Square voltage pulses of varying amplitude and duration were applied across the device and resistor using a function generator and the voltage across the current limiting resistor was measured. The signal rise time was around 2 ns and VO_2 switching was indistinguishable from the rising signal indicating that the phase transition occurs faster than 2ns. Then steady-state optical transmission measurements were conducted as an electrical signal was applied to contacts. The maximum modulation depth was found to be around 7 dB when the entire 2.5 μm patch of VO_2 is switched. The smallest modulation depth was found to be 0.1 dB when the current is limited by a large resistor (22 kΩ), which corresponded roughly to a single grain of VO_2 switched (60 x 100 x 60 nm). FDTD simulations were used to estimate the size of the VO_2 metallic inclusion based on the experimental modulation depth. Transient electro-optical modulation measurements were then conducted for various voltage pulse durations (10ns-1000ns). The optical signal starts to decrease as soon as the electrical signal rises and saturates after about 50 ns. The propagation of the metallic VO_2 inclusion is about 30 nm/ns based on FDTD simulations and heat transfer FEM simulations. The shortest optical signals we were able to detect were 10 ns long, with rise and fall times of 2-3 ns. These measurements were limited by our measurement setup, which had a rise time of 2 ns and bandwidth of about 200 MHz. The bottleneck in the setup was the optical detector (New Focus FPD510), as high speed, high gain, and high sensitivity are not easily achieved together in detectors. A major contribution to the field of study of electrical switching of VO_2 was made as the dynamics of phase transition were explained entirely in terms of thermal heating. One key factor missing from most other studies was found to be free carrier generation via Poole-Frenkel emission. When taken into account, it drops the resistance of the VO_2 film and increases localized heating. The key to fast switching is keeping the active portion of VO_2 very small (tens of nanometers), which allows for the phase transition to occur on picosecond time scales. This discovery should drive VO_2 electro-optic modulator research towards careful thermal design with an emphasis on controlling the current through the VO_2 structure. This can be done by designing control circuitry to drive the modulator. Another consideration is designing a modulator that can take full advantage of a small portion of VO_2 switching and convert it to a large signal modulation.

This issue was addressed with the design of a hybrid plasmonic Si-VO_2-Au modulator. With realizable fabrication in mind, we designed a modulator based on near-field coupling of plasmonic nanodisks deposited on top of a VO_2 film. Always thinking about practical implementation, we decided to couple the plasmonic modulator to a photonic waveguide, because photonics is more efficient at transmitting optical signals while plasmonics is more efficient at modulating them in a compact footprint. There were existing solutions for converting a TM-polarized photonic waveguide mode to a hybrid plasmonic mode with 75 % efficiency, so we chose to use a hybrid mode for our plasmonic modulator. The hybrid mode was confined within the VO_2 layer between silicon and gold and therefore also had maximum overlap with the active material (VO_2). The hybrid mode was simulated using the beam propagation method by Lumerical Mode Solver and then FDTD was used to simulate propagation loss. Even though a continuous film configuration could achieve 15 dB/μm modulation if entire VO_2 layer is switched to the metallic state, this method would be slow due to heating across the VO_2 film. In order to facilitate faster switching speeds, a smaller portion of VO_2 active material needs to be used. When the plasmonic film is broken up into particles, the mode tends to concentrate between those particles. If the particles are very close together, the active portion of VO_2 between the particles is therefore very small. FDTD simulations were used to design a modulator consisting of gold nanodisks on top of a VO_2 film. The thickness of the films in the stack was first optimized to provide a transmission peak at 1550 nm wavelength; optical transmission was initially optimized by simulating just a single nanodisk particle. The optimum film thicknesses for VO_2 and gold were found to be 40 nm and 60 nm, respectively, and the optimum nanodisk diameter was found to be 160 nm. Then the same method was used to find an optimum nanodisk chain length and spacing, which turned out to be 3 and 20 nm, respectively. After the geometry was set, the performance was evaluated using FDTD simulations with varying portions of the VO_2 switched to a metallic state. The modulator was very sensitive to small changes in VO_2 state in the gaps between particles and for a rather small volume of VO_2 switched (60 x 20 x 40 nm) the modulation depth was more than 5 dB. Taking into consideration a very short length of the modulator (560 nm), the extinction ratio per unit length is record high among plasmonic modulators (9 dB/μm). Using experimental data from Chapter 3, the switching voltage was extrapolated to be 0.4 V and the switching power was estimate to be 4.8 mW, which are also respectably low values.

5.2 Future Directions

5.2.1 Realizing the Plasmonic Modulator

The design of the hybrid plasmonic Si-VO_2-Au modulator was geared towards achievable fabrication. The fabrication is not trivial for several reasons including: (1) deposition of VO_2 on top of a pre-defined structure, and (2) critical dimensions of plasmonic nanodisks. The opening for VO_2 needs to be aligned with the silicon support structure underneath, and the critical dimension of the VO_2 patch needs to be on the order of 200 nm. The investigation of VO_2 switching behavior for different size patches has shown that patches smaller than 500 x 500 nm tend to crystallize in a different manner than larger ones and thus the process needs additional optimization. The crystallization is dependent on the surface to volume ratio of the patch which grows when the patch is made smaller. The annealing conditions will need to be optimized in order to obtain crystalline VO_2 in small patches.

The other consideration is producing sufficiently small gaps to allow coupling between the gold nanodisks. The nanodisk mask openings have to be defined on top of the VO_2 and silicon structures with a low alignment tolerance. The additional challenge to this three-step fabrication is that every layer affects the charge dissipation from the electron beam and effectively changes the dose. That means that dose test done on planar substrates or even on top of a non-complete structure does not accurately predict the dose needed for the full structure fabrication. Producing a fabricated coupler and demonstrating the simulated performance would be a work for the future, but by itself it is not as important until more basic thermal design for VO_2 can be figured out.

5.2.2 Resonant Electro-Optic Hybrid Modulators

Another way mentioned to improve the extinction ratio for small changes in VO_2 composition is to utilize a resonant photonic structure. One of the options is to use the structure used by Ryckman et. al. in ref. [51] and add electrical contacts to it. Adding contacts to the structure is not trivial however, because whatever metal the contacts are made off will induce additional loss in the ring resonator. This loss reduces the Q-factor and makes the resonance shallower, reducing the modulation depth. The current approach introduced in Chapter 3 includes leaving a strip of silicon under the contact, called the contact support. This support will also affect the resonant mode of the ring and introduce additional loss. This contact support issue can be overcome by making the contact support made of silicon dioxide. In order to realize that the whole sample can be covered in 220 nm of SiO_2, which is the height of silicon waveguides. Then openings for VO_2 deposition are etched out in SiO_2 using focused-ion beam. This approach was tested using a helium ion microscope at CNMS/ORNL and proved to be realizable, but ultimately too demanding for absorption modulators in Chapter 3. For ring resonators this approach might be justifiable. Another alternative is using a very thin ($<$100nm) contact support to minimize the mode disturbance. Another possible approach to minimizing the loss due to contacts is creating a standing wave resonator such as a 1D photonic crystal, where the contacts can be places in the regions of minimum mode concentration.

Contact supports do not resolve the metallic contact loss issue however. In order to reduce loss, a different conductive material such as indium tin oxide (ITO) which is transparent for infrared light can be used, or contacts can be placed further apart and off the waveguide, which will reduce the loss but increase switching voltage and power, which is not ideal.

5.2.3 Fundamental VO_2 Switching Times Investigation

In order to confirm our modeling of the time scales of VO_2 SMT, a faster measurement setup is needed. The predicted fastest switching time is on the order of tens of picoseconds, therefore the measurement setup should have a bandwidth of at least 100 GHz. The equipment with this kind of resolution is rare and expensive (>$100k). Function generators with rise times on the order of 10 ps and 100 GHz oscilloscopes are available on the market. The critical element in this setup would be a 100 GHz photodetector with sufficient gain. There are 100 GHz detectors available, but the optical signal needs to be very strong to be detected. Therefore the signal needs to be amplified before it can be detected. At these time scales the packaging and wiring is also critical and expensive. Generally speaking the experiment measuring intrinsic VO_2 switching time is possible, but extremely expensive and can be done in collaboration with a group that owns the equipment needed.

APPENDIX A

SIMULATION CODE

A.1 HoleTranformation.m

`HoleTranformation.m` is a MATLAB script that deforms the hexagonal lattice of holes according to permittivity profile defined in 'materialPermittivity.mat'.

```
%% Petr Markov
% This program will generate hole pattern for a given normalized area (
    Or
% Dielectric function)

clc; clear all;

%% This part exports the material epsilon profile
load 'materialPermittivity.mat'

%% Global Variables of the transform
deformedWindow = [0 10000 0 3000]; % Defines the area of cloaked region
    in nm
Es = 11.86;
Ea = 1;
d = 100; %hole diameter in nm

figure(1); imagesc(eps); colorbar;

%% This piece of code generates area profile
A = 2*Es/(Es+Ea); % field ratio factor between inclusion and substrate
Ah = d^2*pi()/4; %hole area everything is in nanometers
area = Ah*(eps*A-eps-A+Es)./(Es-eps);

tmin = 0.578*d; % minimum side of the hexagon cell
Amin = 3*sqrt(3)/2*tmin^2; %min area of the hexagon cell


%% Use external function to generate the hexagonal lattice
load 'coupler_hex_lattice.mat'
[dummy, basis1, basis2] = hex_lattice_generate([0 1 0 1]);

%% Define transformation needed to stretch the lattice to corespond to
    nm
%% coordinate system. Stretch it to where it corresponds to average area
     to
```

```
%% start with
area(find(area<7000))=0;
figure(1); imagesc(area); colorbar;
T = d*eye(4);
M = T*M;
figure(2); scatter(M(1,:),M(2,:),'r');


stretch = 0;
counter = 0;
%% Loop here through every point to deform the lattice
for n=1:2
for c = 1:length(M(1,:)-1)

    %af
    %% This part finds what the area of current hexagon needs to be
    % First of all we need to make sure it is inside the deformed window
    if M(1,c)>deformedWindow(1) && M(1,c)<deformedWindow(2) && M(2,c)>
       deformedWindow(3) && M(2,c)<deformedWindow(4)

        if counter > 10
          counter = 0;
          figure(3); scatter(M(1,:),M(2,:)); hold on; scatter(M(1,c),M
              (2,c),'r');
          hold off;axis([0 10000 0 10000]);

        end
        counter = counter + 1;
        % Conversion from coordinates of the hex lattice to the
        % coordinates of the stretch matrix
        % (x-x0)/(xend-x0)*cloakDimensions*cloakResolution
        ax = fix((M(1,c)-deformedWindow(1))*length(area(:,1))/(
            deformedWindow(2)-deformedWindow(1)))+1;
        ay = fix((M(2,c)-deformedWindow(3))*length(area(1,:))/(
            deformedWindow(4)-deformedWindow(3)))+1;

        targetArea = area(ax,ay);
        if targetArea < 2000
            targetArea = 0;
        end
        %% This part finds the areas of all the hexagons
        [vv , cc] = voronoin(M(1:2,:)');
        af = zeros (size(cc));
        for i = 1 : length (cc)
            af(i) = polyarea (vv(cc{i, :}, 1), vv (cc{i, :}, 2));

        end
        %af=af/min(af);
        for i = 1 : length (cc)
            if af(i)>800000 || isnan(af(i))
                af(i) = 0;
            end
        end
        %af;
```

```
    %% This part decides what the stretch should be
    if(targetArea==0) || (targetArea <Amin)
        stretch = 0;
    else
        if((length(cc{c})==6)&&(af(c)~=0))
            areaStretch = targetArea-af(c);

            if areaStretch<0
                areaStretch = -areaStretch;
                stretch = -0.5*(areaStretch^(0.5));
            else
                stretch = 0.5*areaStretch^(0.5);
            end
        else
            stretch=0;
        end
        if(abs(stretch)> targetArea)
            if(stretch<0)
                stretch = -50;
            else
                stretch=50;
            end
        end
    end
else
    stretch = 0;
end



%% Main loop that goes thru all the rest of the points and modifies
%% their coordinates
if  (stretch <= 0)% If stretch is zero, there is no need to go thru
   the loop
else

    for n = c+1:length(M(1,:))
        direction = (M(3,n)-M(3,c))*basis1 + (M(4,n)-M(4,c))*basis2;
        %get the general direction
        direction = direction/sqrt(direction(1)^2+direction(2)^2);
        % get direction unit vector
        distance = sqrt(direction(1)^2+direction(2)^2);

        directionBasis = (M(3,n)-M(3,c))*[1;0] + (M(4,n)-M(4,c))
           *[0;1];
        %get the general direction
        directionBasis = direction/sqrt(directionBasis(1)^2+
           directionBasis(2)^2);
        % get direction unit vector

        %% Move each point in the array
        M(1,n) = M(1,n)+direction(1)*stretch/distance^2;
        M(2,n) = M(2,n)+direction(2)*stretch/distance^2;
        M(3,n) = M(3,n)+directionBasis(1)*stretch/distance^2;
```

```
            M(4,n) = M(4,n)+directionBasis(2)*stretch/distance^2;
        end
    end
    %% Move original point
    DM = [0.707; 0.707];
    U = [ 0.5 0.5; 0.866 −0.866];
    V = U^−1*DM;

end
end
scatter(M(1,:),M(2,:),3);
```

A.2 hex_lattice_generate.m

`hex_lattice_generate.m` is a MATLAB function that generates a hexagonal array of points or holes.

```
function [ points, basis1, basis2 ] = hex_lattice_generate( area )
%% Generate Hex Lattice
% Basis length is always one
% This part calculates cartesian coordinates of a hexogonal lattice
% This is for simulation in Meep and MPB
latticeSize = [area(2)−area(1) area(4)−area(3)];
basis1 = [0.5;sqrt(3)/2];
basis2 = [−0.5; sqrt(3)/2];
latticeX = []; % First is the x index of the hole,
latticeY = [];
latticeXB = []; %
latticeYB = [];

index =1;


for(n=−latticeSize(1)/2−10:latticeSize(1)/2+10)
    for(nn=−latticeSize(2)/2−10:latticeSize(2)/2+10)

        X = n*basis1(1) + nn* basis2(1);
        Y = n*basis1(2)+nn*basis2(2);
        if((abs(X)<=latticeSize(1)/2)&&(abs(Y)<=latticeSize(2)/2))

                latticeX(index) = X;
                latticeY(index) = Y;
                 latticeXB(index) = n;
                latticeYB(index) = nn;



               %latticeZ(index) = area(fix(X)+1,fix(Y)+1);
                %latticeZ(index) = 0;
               index = index +1;
        end
   end
```

```
end
latticeX = latticeX + area(1)+latticeSize(1)/2;
latticeY = latticeY + area(3)+latticeSize(2)/2;
points = [latticeX; latticeY; latticeXB;latticeYB];
end
```

BIBLIOGRAPHY

[1] J. B. Pendry, D. Schurig, and D. R. Smith. Controlling electromagnetic fields. *Science*, 312 (5781):1780–1782, 2006.

[2] T. Zentgraf, J. Valentine, N. Tapia, J. Li, and X. Zhang. An optical "Janus" device for integrated photonics. *Adv. Mater.*, 22(23):2561–2564, 2010.

[3] J. Valentine, J. Li, T. Zentgraf, G. Bartal, and X. Zhang. An optical cloak made of dielectrics. *Nat. Mater.*, 8(7):568–571, 2009. 10.1038/nmat2461.

[4] H. Xu, Z. Li, Y. Zhu, Y. Li, Y. Yu, and J. Yu. Silicon optical modulator with integrated grating couplers based on 0.18-μm complementary metal oxide semiconductor technology. *Optical Engineering*, 50(4):044001–044001–5, 2011.

[5] Q. Xu, B. Schmidt, S. Pradhan, and M. Lipson. Micrometre-scale silicon electro-optic modulator. *Nature*, 435(7040):325–327, 2005. 10.1038/nature03569.

[6] V. Eyert. The metal-insulator transitions of VO_2: A band theoretical approach. *Annalen der Physik*, 11(9):650–704, 2002.

[7] J. B. Kana Kana, J. M. Ndjaka, G. Vignaud, A. Gibaud, and M. Maaza. Thermally tunable optical constants of vanadium dioxide thin films measured by spectroscopic ellipsometry. *Opt. Comm.*, 284(3):807–812, 2011.

[8] J. M. Atkin, S.l Berweger, E. K. Chavez, M. B. Raschke, J. Cao, W. Fan, and J. Wu. Strain and temperature dependence of the insulating phases of VO_2 near the metal-insulator transition. *Phys. Rev. B*, 85(2):020101, 2012.

[9] J. D. Ryckman, V. Diez-Blanco, J. Nag, R. E. Marvel, B. K. Choi, R. F. Haglund, and S. M. Weiss. Photothermal optical modulation of ultra-compact hybrid Si-VO_2 ring resonators. *Opt. Express*, 20(12):13215–13225, 2012.

[10] X. Wen, Q. Zhang, J. Chai, L. M. Wong, S. Wang, and Q. Xiong. Near-infrared active metamaterials and their applications in tunable surface-enhanced raman scattering. *Opt. Express*, 22(3):2989–2995, Feb 2014.

[11] T. Chung, S.-Y. Lee, E. Y. Song, H. Chun, and B. Lee. Plasmonic nanostructures for nanoscale bio-sensing. *Sensors*, 11(11):10907–10929, 2011.

[12] V. R. Almeida, R. R. Panepucci, and M. Lipson. Nanotaper for compact mode conversion. *Opt. Lett.*, 28(15):1302–1304, 2003.

[13] A. Khilo, M. A. Popovi, M. Araghchini, and F. X. Krtner. Efficient planar fiber-to-chip coupler based on two-stage adiabatic evolution. *Opt. Express*, 18(15):15790–15806, 2010.

[14] R. M. Briggs, I. M. Pryce, and H. A. Atwater. Compact silicon photonic waveguide modulator based on the vanadium dioxide metal-insulator phase transition. *Opt. Express*, 18(11): 11192–11201, 2010.

[15] A. Joushaghani, B. A. Kruger, S. Paradis, D. Alain, J. S. Aitchison, and J. K. S. Poon. Sub-volt broadband hybrid plasmonic-vanadium dioxide switches. *Appl. Phys. Lett.*, 102 (6):061101–4, 2013.

[16] D. B. Keck, R. D. Maurer, and P. C. Schultz. On the ultimate lower limit of attenuation in glass optical waveguides. *Applied Physics Letters*, 22(7):307–309, 1973.

[17] R. N. Hall. Semiconductor junction laser device, December 19 1967. URL `http://www.google.com/patents/US3359507`. US Patent 3,359,507.

[18] R. Pries, M. Jarschel, D. Schlosser, M. Klopf, and P. Tran-Gia. Power consumption analysis of data center architectures. In *Green Communications and Networking*, pages 114–124. Springer, 2012.

[19] M. Haurylau, G. Chen, H. Chen, J. Zhang, N. A. Nelson, D. H. Albonesi, E. G. Friedman, and P. M. Fauchet. On-chip optical interconnect roadmap: Challenges and critical directions. *Selected Topics in Quantum Electronics, IEEE Journal of*, 12(6):1699–1705, 2006.

[20] D. A. B. Miller. Device requirements for optical interconnects to silicon chips. *Proceedings of the IEEE*, 97(7):1166–1185, 2009.

[21] G. E. Moore. Cramming more components onto integrated circuits, Reprinted from Electronics, volume 38, number 8, April 19, 1965, pp.114 ff. *Solid-State Circuits Society Newsletter, IEEE*, 11(5):33–35, 2006.

[22] T. E. Northup and R. Blatt. Quantum information transfer using photons. *Nat. Photon.*, 8(5): 356–363, 2014.

[23] X.-L. Qi and S.-C. Zhang. Topological insulators and superconductors. *Rev. Mod. Phys.*, 83: 1057–1110, Oct 2011.

[24] K. Sotthewes, V. Geskin, R. Heimbuch, A. Kumar, and H. J. W. Zandvliet. Research update: Molecular electronics: The single-molecule switch and transistor. *APL Materials*, 2(1): 010701, 2014.

[25] G. Chen, H. Chen, M. Haurylau, N. A. Nelson, D. H. Albonesi, P. M. Fauchet, and E. G. Friedman. On-chip copper-based vs. optical interconnects: Delay uncertainty, latency, power, and bandwidth density comparative predictions. In *Interconnect Technology Conference, 2006 International*, pages 39–41, June 2006.

[26] Y. Ho, D. Lee, M. O. Thompson, and M. Lipson. Deposited low temperature silicon GHz modulator. *Opt. Express*, 21(22):26688–26692, Nov 2013.

[27] L. A. Coldren, S. W. Corzine, and M. L. Mashanovitch. *Diode lasers and photonic integrated circuits*, volume 218. John Wiley & Sons, 2012.

[28] H. Rong, R. Jones, A. Liu, O. Cohen, D. Hak, A. Fang, and M. Paniccia. A continuous-wave Raman silicon laser. *Nature*, 433(7027):725–728, 2005. 10.1038/nature03346.

[29] E. D. Palik. *Handbook of Optical Constants of Solids*, volume 5. Academic Press, 1997.

[30] M. Lipson. Compact electro-optic modulators on a silicon chip. *Selected Topics in Quantum Electronics, IEEE Journal of*, 12(6):1520–1526, Nov 2006.

[31] J. Komma, C. Schwarz, G. Hofmann, D. Heinert, and R. Nawrodt. Thermo-optic coefficient of silicon at 1550nm and cryogenic temperatures. *Appl. Phys. Lett.*, 101(4):041905, 2012.

[32] A. W. Fang, H. Park, O. Cohen, R. Jones, M. J. Paniccia, and J. E. Bowers. Electrically pumped hybrid AlGaInAs-silicon evanescent laser. *Opt. Express*, 14(20):9203–9210, 2006.

[33] D. Schurig, J. J. Mock, B. J. Justice, S. A. Cummer, J. B. Pendry, A. F. Starr, and D. R. Smith. Metamaterial electromagnetic cloak at microwave frequencies. *Science*, 314(5801): 977–980, 2006.

[34] J. Li and J. B. Pendry. Hiding under the carpet: A new strategy for cloaking. *Phys. Rev. Lett.*, 101(20):203901, 2008. PRL.

[35] L. H. Gabrielli, J. Cardenas, C. B. Poitras, and M. Lipson. Silicon nanostructure cloak operating at optical frequencies. *Nat. Photon.*, 3(8):461–463, 2009. 10.1038/nphoton.2009.117.

[36] J. H. Lee, J. Blair, V. A. Tamma, Q. Wu, S. J. Rhee, C. J. Summers, and W. Park. Direct visualization of optical frequency invisibility cloak based on silicon nanorod array. *Opt. Express*, 17(15):12922–12928, 2009.

[37] D. A. Genov, S. Zhang, and X. Zhang. Mimicking celestial mechanics in metamaterials. *Nat. Phys.*, 5(9):687–692, 2009. 10.1038/nphys1338.

[38] C. Qiang, C. Tie Jun, J. Wei Xiang, and C. Ben Geng. An omnidirectional electromagnetic absorber made of metamaterials. *New Journal of Physics*, 12(6):063006, 2010.

[39] V. M. Shalaev. Optical negative-index metamaterials. *Nat. Photon.*, 1(1):41–48, 2007. 10.1038/nphoton.2006.49.

[40] D. J. Thomson, F. Y. Gardes, Y. Hu, G. Mashanovich, M. Fournier, P. Grosse, J. M. Fedeli, and G. T. Reed. High contrast 40Gbit/s optical modulation in silicon. *Opt. Express*, 19(12): 11507–11516, 2011.

[41] G. T. Reed, G. Mashanovich, F. Y. Gardes, and D. J. Thomson. Silicon optical modulators. *Nat. Photon.*, 4(8):518–526, 2010. 10.1038/nphoton.2010.179.

[42] P. Dong, S.g Liao, D. Feng, H. Liang, D. Zheng, R. Shafiiha, C.-C. Kung, W. Qian, G. Li, X. Zheng, A. V. Krishnamoorthy, and M. Asghari. Low Vpp, ultralow-energy, compact, high-speed silicon electro-optic modulator. *Opt. Express*, 17(25):22484–22490, 2009.

[43] F. Y. Gardes, A. Brimont, P. Sanchis, G. Rasigade, D. Marris-Morini, L. O'Faolain, F. Dong, J. M. Fedeli, P. Dumon, L. Vivien, T. F. Krauss, G. T. Reed, and J. Mart. High-speed modulation of a compact silicon ring resonator based on a reverse-biased pn diode. *Opt. Express*, 17(24):21986–21991, 2009.

[44] A. Liu, R. Jones, L. Liao, D. Samara-Rubio, D. Rubin, O. Cohen, R. Nicolaescu, and M. Paniccia. A high-speed silicon optical modulator based on a metal-oxide-semiconductor capacitor. *Nature*, 427(6975):615–618, 2004. 10.1038/nature02310.

[45] T. Baba, S. Akiyama, M. Imai, N. Hirayama, H. Takahashi, Y. Noguchi, T. Horikawa, and T. Usuki. 50-Gb/s ring-resonator-based silicon modulator. *Opt. Express*, 21(10):11869–11876, 2013.

[46] J. E. Zucker, K. L. Jones, B. I. Miller, and U. Koren. Miniature Mach-Zehnder InGaAsP quantum well waveguide interferometers for 1.3 μm. *IEEE Photon. Technol. Lett.*, 2:32–34, 1990. 10.1109/68.47033.

[47] E. L. Wooten. A review of lithium niobate modulators for fiber-optic communications systems. *IEEE J. Select. Topics Quant. Electron.*, 6:69–82, 2000. 10.1109/2944.826874.

[48] M. Hochberg, T. Baehr-Jones, G. Wang, M. Shearn, K. Harvard, J. Luo, B. Chen, Z. Shi, R. Lawson, P. Sullivan, A. K. Y. Jen, L. Dalton, and A. Scherer. Terahertz all-optical modulation in a silicon-polymer hybrid system. *Nat. Mater.*, 5(9):703–709, 2006. 10.1038/nmat1719.

[49] L. Alloatti, D. Korn, R. Palmer, D. Hillerkuss, J. Li, A. Barklund, R. Dinu, J. Wieland, M. Fournier, J. Fedeli, H. Yu, W. Bogaerts, P. Dumon, R. Baets, C. Koos, W. Freude, and J. Leuthold. 42.7 Gbit/s electro-optic modulator in silicon technology. *Opt. Express*, 19(12): 11841–11851, 2011.

[50] M. Liu, X. Yin, E. Ulin-Avila, B. Geng, T. Zentgraf, L. Ju, F. Wang, and X. Zhang. A graphene-based broadband optical modulator. *Nature*, 474(7349):64–67, 2011. 10.1038/nature10067.

[51] J. D. Ryckman, K. A. Hallman, R. E. Marvel, R. F. Haglund, and S. M. Weiss. Ultra-compact silicon photonic devices reconfigured by an optically induced semiconductor-to-metal transition. *Opt. Express*, 21(9):10753–10763, 2013.

[52] B. A. Kruger, A. Joushaghani, and J. K. S. Poon. Design of electrically driven hybrid vanadium dioxide (VO_2) plasmonic switches. *Opt. Express*, 20(21):23598–23609, 2012.

[53] J. A. Dionne, K. Diest, L. A. Sweatlock, and H. A. Atwater. PlasMOStor: A metaloxidesi field effect plasmonic modulator. *Nano Letters*, 9(2):897–902, 2009.

[54] M. Rini, A. Cavalleri, R. W. Schoenlein, R. Lopez, L. C. Feldman, R. F. Haglund, L. A. Boatner, and T. E. Haynes. Photoinduced phase transition in VO_2 nanocrystals: ultrafast control of surface-plasmon resonance. *Opt. Lett.*, 30(5):558–560, 2005.

[55] B. Wu, A. Zimmers, H. Aubin, R. Ghosh, Y. Liu, and R. Lopez. Electric-field-driven phase transition in vanadium dioxide. *Phys. Rev. B*, 84(24):241410, 2011. PRB.

[56] Z. You, C. Xiaonan, K. Changhyun, Y. Zheng, C. Mouli, and S. Ramanathan. Voltage-triggered ultrafast phase transition in vanadium dioxide switches. *Electron Device Letters, IEEE*, 34(2):220–222, 2013.

[57] G. Stefanovich, A. Pergament, and D. Stefanovich. Electrical switching and mott transition in VO_2. *Journal of Physics: Condensed Matter*, 12(41):8837, 2000.

[58] K. Appavoo, D. Y. Lei, Y. Sonnefraud, B. Wang, S. T. Pantelides, S. A. Maier, and R. F. Haglund. Role of defects in the phase transition of VO_2 nanoparticles probed by plasmon resonance spectroscopy. *Nano Letters*, 12(2):780–786, 2012. doi: 10.1021/nl203782y.

[59] D. Wegkamp, M. Herzog, L. Xian, M. Gatti, P. Cudazzo, C. L. McGahan, R. E. Marvel, R. F. Haglund, A. Rubio, M. Wolf, and J. Stähler. Instantaneous band gap collapse in photoexcited monoclinic VO_2 due to photocarrier doping. *Phys. Rev. Lett.*, 113:216401, Nov 2014.

[60] V. R. Morrison, R. P. Chatelain, K. L. Tiwari, A. Hendaoui, A. Bruhacs, M. Chaker, and B. J. Siwick. A photoinduced metal-like phase of monoclinic VO_2 revealed by ultrafast electron diffraction. *Science*, 346(6208):445–448, 2014. 10.1126/science.1253779.

[61] J. Laverock, L. F. J. Piper, A. R. H. Preston, B. Chen, J. McNulty, K. E. Smith, S. Kittiwatanakul, J. W. Lu, S. A. Wolf, P.-A. Glans, and J.-H. Guo. Strain dependence of bonding and hybridization across the metal-insulator transition of VO_2. *Phys. Rev. B*, 85:081104, Feb 2012.

[62] M. Liu, H. Y. Hwang, H. Tao, A. C. Strikwerda, K. Fan, G. R. Keiser, A. J. Sternbach, K. G. West, S. Kittiwatanakul, J. Lu, S. A. Wolf, F. G. Omenetto, X. Zhang, K. A. Nelson, and R. D. Averitt. Terahertz-field-induced insulator-to-metal transition in vanadium dioxide metamaterial. *Nature*, 487(7407):345–348, 2012. 10.1038/nature11231.

[63] A. Pashkin, C. Kbler, H. Ehrke, R. Lopez, A. Halabica, R. F. Haglund, R. Huber, and A. Leitenstorfer. Ultrafast insulator-metal phase transition in VO_2 studied by multiterahertz spectroscopy. *Phys. Rev. B*, 83(19):195120, 2011. PRB.

[64] R. Thomas, Z. Ikonic, and R. W. Kelsall. Electro-optic metalinsulatorsemiconductorinsulatormetal mach-zehnder plasmonic modulator. *Photonics and Nanostructures - Fundamentals and Applications*, 10(1):183 – 189, 2012. ISSN 1569-4410.

[65] A. Melikyan, N. Lindenmann, S. Walheim, P. M. Leufke, S. Ulrich, J. Ye, P. Vincze, H. Hahn, Th. Schimmel, C. Koos, W. Freude, and J. Leuthold. Surface plasmon polariton absorption modulator. *Opt. Express*, 19(9):8855–8869, Apr 2011.

[66] A. Melikyan, L. Alloatti, A. Muslija, D. Hillerkuss, P. C. Schindler, J. Li, R. Palmer, D. Korn, S. Muehlbrandt, D. Van Thourhout, B. Chen, R. Dinu, M. Sommer, C. Koos, M. Kohl, W. Freude, and Leuthold. J. High-speed plasmonic phase modulators. *Nat. Photon.*, 8(3): 229–233, 2014.

[67] E. Hutter and J.H. Fendler. Exploitation of localized surface plasmon resonance. *Advanced Materials*, 16(19):1685–1706, 2004. ISSN 1521-4095.

[68] K. R. Catchpole and A. Polman. Design principles for particle plasmon enhanced solar cells. *Appl. Phys. Lett.*, 93(19):191113, 2008.

[69] X. Cui and D. Erni. Enhanced propagation in a plasmonic chain waveguide with nanoshell structures based on low-and high-order mode coupling. *JOSA A*, 25(7):1783–1789, 2008.

[70] J. C. Ndukaife, A. Mishra, U. Guler, A. G. A. Nnanna, S. T. Wereley, and A. Boltasseva. Photothermal heating enabled by plasmonic nanostructures for electrokinetic manipulation and sorting of particles. *ACS Nano*, 8(9):9035–9043, 2014.

[71] M. I. Stockman. Nanoplasmonics: past, present, and glimpse into future. *Opt. Express*, 19 (22):22029–22106, 2011.

[72] L. Chen, X. Li, and G. Wang. A hybrid long-range plasmonic waveguide with subwavelength confinement. *Opt. Comm.*, 291(0):400 – 404, 2013.

[73] Y. Song, J. Wang, Q. Li, M. Yan, and M. Qiu. Broadband coupler between silicon waveguide and hybrid plasmonic waveguide. *Opt. Express*, 18(12):13173–13179, 2010.

[74] OZ Optics Limited. Tapered and lensed fibers, 2011.

[75] D. Taillaert, W. Bogaerts, P. Bienstman, T. F. Krauss, P. van Daele, I. Moerman, S. Verstuyft, K. De Mesel, and R. Baets. An out-of-plane grating coupler for efficient butt-coupling between compact planar waveguides and single-mode fibers. *Quantum Electronics, IEEE Journal of*, 38(7):949–955, 2002.

[76] D. Taillaert, P. Bienstman, and R. Baets. Compact efficient broadband grating coupler for silicon-on-insulator waveguides. *Opt. Lett.*, 29(23):2749–2751, 2004.

[77] F. Van Laere, G. Roelkens, M. Ayre, Jonathan Schrauwen, D. Taillaert, D. Van Thourhout, T. F. Krauss, and R. Baets. Compact and highly efficient grating couplers between optical fiber and nanophotonic waveguides. *Lightwave Technology, Journal of*, 25(1):151–156, 2007.

[78] M. Fan, M. Popovic, and F. X. Kaertner. High directivity, vertical fiber-to-chip coupler with anisotropically radiating grating teeth. OSA Technical Digest Series (CD), page CTuDD3. Optical Society of America, 2007.

[79] T. Shoji, T. Tsuchizawa, T. Watanabe, K. Yamada, and H. Morita. Low loss mode size converter from 0.3 μm square si wire waveguides to singlemode fibres. *Electronics Letters*, 38(25):1669–1670, 2002.

[80] G. Roelkens, P. Dumon, W. Bogaerts, D. Van Thourhout, and R. Baets. Efficient silicon-on-insulator fiber coupler fabricated using 248-nm-deep UV lithography. *Photonics Technology Letters, IEEE*, 17(12):2613–2615, 2005.

[81] K. K. Lee, D. R. Lim, D. Pan, C. Hoepfner, W.-Y. Oh, K. Wada, L. C. Kimerling, K. P. Yap, and M. T. Doan. Mode transformer for miniaturized optical circuits. *Opt. Lett.*, 30(5): 498–500, 2005.

[82] L. H. Gabrielli and M. Lipson. Integrated Luneburg lens via ultra-strong index gradient on silicon. *Opt. Express*, 19(21):20122–20127, 2011.

[83] Z. Chang, X. Zhou, J. Hu, and G. Hu. Design method for quasi-isotropic transformation materials based on inverse laplace's equation with sliding boundaries. *Opt. Express*, 18(6): 6089–6096, 2010.

[84] C. Garcia-Meca, M. M. Tung, J. V. Galan, R. Ortuno, F. J. Rodriguez-Fortuno, J. Marti, and A. Martinez. Squeezing and expanding light without reflections via transformation optics. *Opt. Express*, 19(4):3562–3575, 2011.

[85] P.-H. Tichit, S. N. Burokur, and A. de Lustrac. Waveguide taper engineering using coordinate transformation technology. *Opt. Express*, 18(2):767–772, 2010.

[86] C. Zang, X.and Jiang. Manipulating the field distribution via optical transformation. *Opt. Express*, 18(10):10168–10176, 2010.

[87] D. H. Spadoti, L. H. Gabrielli, C. B. Poitras, and M. Lipson. Focusing light in a curved-space. *Opt. Express*, 18(3):3181–3186, 2010.

[88] A. F Oskooi, D. Roundy, M. Ibanescu, P. Bermel, J. D Joannopoulos, and S. G Johnson. MEEP: a flexible free-software package for electromagnetic simulations by the FDTD method. *Computer Physics Communications*, 181(3):687–702, 2010.

[89] P. Markov, J. G. Valentine, and S. M. Weiss. Fiber-to-chip coupler designed using an optical transformation. *Opt. Express*, 20(13):14705–14713, 2012.

[90] P. P. Boriskov, A. A. Velichko, A. L. Pergament, G. B. Stefanovich, and D. G. Stefanovich. The effect of electric field on metal-insulator phase transition in vanadium dioxide. *Technical Physics Letters*, 28(5):406–408, 2002.

[91] B.-G. Chae, H.-T. Kim, D.-H. Youn, and K.-Y. Kang. Abrupt metalinsulator transition observed in VO_2 thin films induced by a switching voltage pulse. *Physica B: Condensed Matter*, 369(14):76–80, 2005.

[92] G. Gopalakrishnan, D. Ruzmetov, and S. Ramanathan. On the triggering mechanism for the metalinsulator transition in thin film VO_2 devices: electric field versus thermal effects. *Journal of Materials Science*, 44(19):5345–5353, 2009.

[93] S. Hormoz and S. Ramanathan. Limits on vanadium oxide mott metalinsulator transition field-effect transistors. *Solid-State Electronics*, 54(6):654–659, 2010.

[94] K. Hyun-Tak, C. Byung-Gyu, Y. Doo-Hyeb, M. Sung-Lyul, K. Gyungock, K. Kwang-Yong, and L. Yong-Sik. Mechanism and observation of mott transition in VO_2 -based two- and three-terminal devices. *New Journal of Physics*, 6(1):52, 2004.

[95] H. Ji, J. Wei, and D. Natelson. Modulation of the electrical properties of VO_2 nanobeams using an ionic liquid as a gating medium. *Nano Letters*, 12(6):2988–2992, 2012.

[96] J. Jeong, N. Aetukuri, T. Graf, T. D. Schladt, M. G. Samant, and S. P. Stuart-Parkin. Suppression of metal-insulator transition in VO_2 by electric fieldinduced oxygen vacancy formation. *Science*, 339(6126):1402–1405, 2013.

[97] A. Joushaghani, J. Jeong, S. Paradis, D. Alain, S. J. Aitchison, and J. K. S. Poon. Voltage-controlled switching and thermal effects in VO_2 nano-gap junctions. *Appl. Phys. Lett.*, 104 (22):–, 2014.

[98] C. Ko and S. Ramanathan. Observation of electric field-assisted phase transition in thin film vanadium oxide in a metal-oxide-semiconductor device geometry. *Appl. Phys. Lett.*, 93(25): –, 2008.

[99] J. Kim, C.n Ko, A. Frenzel, S. Ramanathan, and J. E. Hoffman. Nanoscale imaging and control of resistance switching in VO_2 at room temperature. *Appl. Phys. Lett.*, 96(21):–, 2010.

[100] K. Seal, A. Sharoni, J. M. Messman, B. S. Lokitz, R. W. Shaw, I. K. Schuller, P. C. Snijders, and T. Z. Ward. Resolving transitions in the mesoscale domain configuration in VO_2 using laser speckle pattern analysis. *Sci. Rep.*, 4, 2014.

[101] J. Sakai, M. Zaghrioui, M. Matsushima, H. Funakubo, and K. Okimura. Impact of thermal expansion of substrates on phase transition temperature of VO_2 films. *Journal of Applied Physics*, 116(12):–, 2014.

[102] S. Zhang, M. A. Kats, Y. Cui, Y. Zhou, Y. Yao, S. Ramanathan, and F. Capasso. Current-modulated optical properties of vanadium dioxide thin films in the phase transition region. *Appl. Phys. Lett.*, 105(21):–, 2014.

[103] J. Rozen, R. Lopez, R. F. Haglund, and L. C. Feldman. Two-dimensional current percolation in nanocrystalline vanadium dioxide films. *Appl. Phys. Lett.*, 88(8):–, 2006.

[104] A. Zimmers, L. Aigouy, M. Mortier, A. Sharoni, Siming Wang, K. West, J. Ramirez, and Ivan Schuller. Role of thermal heating on the voltage induced insulator-metal transition in VO_2. *Phys. Rev. Lett.*, 110(5):056601, 2013. PRL.

[105] C. Zener. A theory of the electrical breakdown of solid dielectrics. *Proceedings of the Royal Society of London A: Mathematical, Physical and Engineering Sciences*, 145(855):523–529, 1934. ISSN 0950-1207. doi: 10.1098/rspa.1934.0116.

[106] S. D. Ganichev, E. Ziemann, W. Prettl, I. N. Yassievich, A. A. Istratov, and E. R. Weber. Distinction between the Poole-Frenkel and tunneling models of electric-field-stimulated carrier emission from deep levels in semiconductors. *Phys. Rev. B*, 61:10361–10365, Apr 2000.

[107] J. S. Brockman, L. Gao, B. Hughes, C. T. Rettner, M. G. Samant, K. P. Roche, and S. P. Parkin-Stuart. Subnanosecond incubation times for electric-field-induced metallization of a correlated electron oxide. *Nat. Nano.*, 9(6):453–458, 2014.

[108] A. A. Stabile, S. K. Singh, T.-L. Wu, L. Whittaker, S. Banderjee, and G. Sambandamurthy. Separating electric field and thermal effects across the metal-insulator transition in vanadium oxide nanobeams, 2014.

[109] Z. Tao, T.-R. T. Han, S. D. Mahanti, P. M. Duxbury, F. Yuan, C.-Y. Ruan, K. Wang, and J. Wu. Decoupling of structural and electronic phase transitions in VO_2. *Phys. Rev. Lett.*, 109 (16):166406, 2012. PRL.

[110] M. Rini, Z. Hao, R. W. Schoenlein, C. Giannetti, F. Parmigiani, S. Fourmaux, J. C. Kieffer, A. Fujimori, M. Onoda, S. Wall, and A. Cavalleri. Optical switching in VO_2 films by below-gap excitation. *Appl. Phys. Lett.*, 92(18):–, 2008.

[111] T.-L. Liu, K. J. Russell, S. Cui, and E. L. Hu. Two-dimensional hybrid photonic/plasmonic crystal cavities. *Opt. Express*, 22(7):8219–8225, 2014.

[112] X. Yang, A.i Ishikawa, X. Yin, and X. Zhang. Hybrid photonic-plasmonic crystal nanocavities. *ACS Nano*, 5(4):2831–2838, 2011.

[113] R. F. Oulton, V. J. Sorger, D. A. Genov, D. F. P. Pile, and X. Zhang. A hybrid plasmonic waveguide for subwavelength confinement and long-range propagation. *Nat. Photon.*, 2(8): 496–500, 2008. 10.1038/nphoton.2008.131.

[114] P. Markov, K. Appavoo, R. F. Haglund, and S. M. Weiss. Hybrid Si-VO_2-Au optical modulator based on near-field plasmonic coupling. *Opt. Express*, 23(5):6878–6887, Mar 2015.

[115] M. Nakano, K. Shibuya, D. Okuyama, T. Hatano, S. Ono, M. Kawasaki, Y. Iwasa, and Y. Tokura. Collective bulk carrier delocalization driven by electrostatic surface charge accumulation. *Nature*, 487(7408):459–462, 2012. 10.1038/nature11296.

[116] K. Appavoo and R. F. Haglund. Detecting nanoscale size dependence in VO_2 phase transition using a split-ring resonator metamaterial. *Nano Letters*, 11(3):1025–1031, 2011.

[117] K. Appavoo and R. F. Haglund Jr. Polarization selective phase-change nanomodulator. *Sci. Rep.*, 4, 2014.

[118] F. Yaghmaie, J. Fleck, A. Gusman, and R. Prohaska. Improvement of PMMA electron-beam lithography performance in metal liftoff through a poly-imide bi-layer system. *Microelectronic Engineering*, 87(12):2629–2632, 2010.

[119] P. Markov, J. D. Ryckman, R. E. Marvel, K. A. Hallman, R. F. Haglund, and S. M. Weiss. Silicon-VO_2 hybrid electro-optic modulator. In *CLEO: 2013*, OSA Technical Digest (online), page CTu2F.7. Optical Society of America, 2013.

[120] A. Crunteanu, J. Givernaud, J. Leroy, D. Mardivirin, C. Champeaux, J.-C. Orlianges, A. Catherinot, and P. Blondy. Voltage- and current-activated metalcinsulator transition in VO_2-based electrical switches: a lifetime operation analysis. *Science and Technology of Advanced Materials*, 2010.

[121] J. Nag, R. F. Haglund, A. E. Payzant, and K. L. More. Non-congruence of thermally driven structural and electronic transitions in VO_2. *J. of Appl. Phys.*, 112(10):103532, 2012.